Engineering Functional Materials from Cellulose Nanocrystals by Exploring Their Structure and Property Relationships

by

Ananya Ghosh

A dissertation submitted to the Graduate Faculty of
Auburn University
in partial fulfillment of the
requirements for the Degree of
Doctor of Philosophy

Auburn, Alabama
August 3, 2024

Keywords: Cellulose Nanocrystal, Order parameter, Nematic structure, Optical property, Mechanical shear, and Freeze-Thaw

Approved by

Zhihua Jiang, Chair, Auburn Pulp and Paper Foundation Associate Professor, Chemical Engineering, Auburn University
Virginia A. Davis, Dr. Daniel F. and Josephine Breeden Professor, Chemical Engineering, Auburn University
Xinyu Zhang, Professor, Graduate Program Chair, Chemical Engineering, Auburn University
Zhongyang Cheng, McWane Professor, Mechanical Engineering, Auburn University
Thomas Elder, Research Scientist, USDA-Forest Service, and Professor Emeritus, College of Forestry, Wildlife and Environment, Auburn University

Abstract

The objective of this research was to utilize cellulose nanocrystals (CNC), a biobased nanomaterial, to understand their fundamental dispersion behavior and to develop CNC based films with high transparency, flexibility, and good optical qualities, which can be used in film packaging, coatings in the electronics industry, or as piezoelectric and optical sensors.

First, the research aimed at exploring the impact of electrolytes on the orientation of cellulose nanocrystals (CNC) in a mechanically shear-cast thin solid films prepared from CNC aqueous gels. Alignment in CNC films are the result of both the ease of achieving shear-induced alignment in the dispersion and the ability to retain that alignment during drying. Changes in the aqueous CNC gels' rheological properties with electrolyte addition were correlated to the orientation and optical properties of dried CNC films. Film alignment was qualitatively assessed using cross-polarized optical microscopy and quantified by order parameters computed by UV-Vis transmission spectroscopy. Electrolyte addition resulted in an increased alignment in dried CNC films. For pure CNC, the film order parameters remained constant at approximately 0.3 for shear rates from 20 s^{-1} to 100 s^{-1}. However, higher order parameters were achieved in the presence of electrolytes. Notably, an order parameter of 0.88 was achieved at a shear rate of only 20 s^{-1}. In addition, films produced from dispersions containing electrolytes exhibited improved clarity and haze as well. The results of this work highlight that electrolyte addition can enable higher order parameters at lower shear rates and facilitate the development of aligned CNC films for applications such as polarizers, clear coatings, and piezoelectric materials.

CNCs produced from sulfuric acid hydrolysis contain an anionic sulfate ester group, which play a crucial role in the structural orientation. Thus, its effect on self-assembly was investigated in the CNC self-assembled solid film. NaOH treatment was performed on commercially purchased sulfated CNC to partially desulfate the CNC, and the self-assembled film was produced by pouring it into a Petri dish and allowing to evaporate in ambient conditions. Comparison between pure CNC and NaOH-treated CNC revealed differences in structural orientation of self-assembled solid films. Complete absence of chiral nematic organization was observed after reaction and the formation of the nematic structure was identified through SEM, cross-polarized microscopy, and UV-Vis spectroscopy. The optical properties of the films were thoroughly investigated and exhibited lowered haze and high clarity and sharpness. Lastly, polyvinyl alcohol (PVA) was added to the CNC to observe the effect of PVA on the optical quality of the film. Overall, a transparent and flexible composite film was developed, which could be utilized as a promising candidate in the film packaging application, especially in the electronic industry.

Moreover, a facile method, the freeze-thaw technique, was introduced where, without any external force or chemical reaction, a completely transparent CNC film can be produced by locking the CNC in an oriented manner. To date, self-assembled transparent CNC solid film can be obtained through chemical doping. It was found that the freeze-thaw method completely eliminated the chiral nematic structure, resulting in transparent films without structural color. Detailed internal structure characterization using SEM, XRD, and UV-Vis spectroscopy coupled with optical property analysis revealed a remarkable improvement in the clarity and sharpness of freeze-thaw based CNC films without compromising transmittance and haze, showing the promise of freeze-thaw based CNC films in packaging and coating applications.

Lastly, the study focused on utilizing cellulose nanocrystal (CNC) – polyvinyl alcohol (PVA) composites as optical sensors to detect high humidity conditions and determine water concentration in ethanol. The chiral nematic structure of CNC was used to prepare a colorimetric sensor. Upon the moisture absorption, the composites demonstrate a visual color change. A CNC-PVA sensor was developed, which can detect high humidity with 2 hours of exposure time. 2,2,6,6-tetramethylpiperidin-1-piperidinyloxy oxidized CNC (TEMPO-CNC) having carboxylic functionality was also used to prepare CNC-PVA composite films in order to compare the effect of functional groups on moisture sensitivity. Finally, we demonstrated a facile method for the utilization of the composite as an optical sensor to detect water concentration in ethanol efficiently, which can have applications in polar organic solvent dehydration.

Acknowledgment

Firstly, I would like to convey my sincere gratitude to my advisor, Dr. Zhihua Jiang, for his continuous support and guidance. His immense knowledge, patience, and encouragement helped me to come this far with my Ph.D. study and research. I would like to express my gratitude to my committee members, Dr. Virginia A. Davis, Dr. Zhongyang Cheng and Dr. Xinyu Zhang, for their feedback, insight, and support towards the completion of my research and dissertation. I would also like to acknowledge Dr. Davis for providing me with her guidance, critical input, and time in one of my research projects. I would like to extend my sincere gratitude to Dr. Thomas Elder, my university reader, for his thoughtful editing and valuable input during the preparation of my dissertation. I would like to express my acknowledgment to Dr. Ramsis Farag for helping me out with the equipment setup and troubleshooting. Further, many thanks to Dr. Davis's, Dr. Cheng's, and Dr. Oh's research group for their help. I would also like to express my gratitude to the members of the Alabama Centre for Paper and Bioresource Engineering (AC-PABE) for their support.

Lastly, I am thankful to my family and friends for providing me with moral support whenever needed. This journey would not be possible without the continuous support of my father, Tapas Kumar Ghosh, and my mother, Debjani Ghosh. Their encouragement throughout my life served as motivation and propelled me to fulfill my dreams. Thanks to my brother, Anirban Ghosh, for the long conversations whenever needed and for guiding me in every stage of my life. I am also grateful to my close friends, Dr. Amod Parkhi and Akhil Teja Kambhampati for their time and support during my stay in Auburn.

Table of Contents

List of Tables

List of Figures

List of Equations

List of Abbreviations

CNC	Cellulose Nanocrystal
PVA	Polyvinyl Alcohol
TEMPO	2,2,6,6-Tetramethylpiperidin-1-piperidinyloxy Oxidized
FT	Freeze-Thaw
PCNC	Pure Cellulose Nanocrystal
PDCNC	Partially Desulfated Cellulose Nanocrystal
TCNC	TEMPO Cellulose Nanocrystal
DCNC	Dialyzed Cellulose Nanocrystal
RPM	Revolution Per Minute
LCP	Left-handed Circular Polarization
RCP	Right-handed Circular Polarization
DI	Deionized
HMW	High Molecular Weight
LMW	Low Molecular Weight

Introduction

The modern world is dependent on novel electronic devices and appliances, materials, automobiles, and synthetic high-performance polymers. Most of these products utilize fossil resources for synthesis. The depletion of fossil fuel sources has been of concern for many years. In addition, petroleum usage increases carbon dioxide emissions, which is a prime reason for global warming [1]. The energy demand to produce petroleum-based products is quite high when compared to bio-based materials. For example, 20% to 50% less energy is required to produce polylactic acid than synthetic polymers [2]. Additionally, biodegradability is an important criterion for resolving the issue regarding landfills and aquatic life conditions [1]. These propel today's research more towards utilizing natural resources and developing novel bio-based materials.

Cellulose is a natural polymer abundantly available on earth and produced at a rate of 1.5×10^{12} tons per year. Cellulose nanocrystals (CNC) are a biomaterial produced from cellulose, which is abundantly present in wood, plants, cotton, agricultural waste, and algae. [3,4]. The rod-like CNC is produced by sulfuric acid hydrolysis, which degrades the amorphous region of the cellulose by disrupting the hydrogen bonds and only retaining the crystalline part [3]. The dimension of CNC is greatly dependent on the source of the cellulose. For example, CNC from hardwood has a diameter of 3 – 5 nm with a length of around 100 – 300 nm, whereas tunicate cellulose CNC is 15 – 30 nm in diameter and 1000 – 1500 nm in length [3]. CNC produced from sulfuric acid hydrolysis incorporates anionic sulfate ester groups on its surface, which facilitates the formation of anisotropic or cholesteric phase in aqueous dispersion. CNC phase transition from isotropic to anisotropic is mostly governed by the aspect ratio and surface charge. Additionally, counterion, the type of counterion solvents, plays a role in the phase behavior. CNC has various valuable

properties, which can be used in various applications such as in developing optical and piezoelectric sensors, additives to prepare nanocomposite to improvise mechanical and thermal properties, and hydrogel as a rheology modifier [3].

This research work mainly focuses on the structure-property relationship of CNC dispersions to develop a functional material suitable for applications in coating, packaging, or piezoelectric sensors. In these application areas, CNC orientation in a thin film, its transparency, and optical properties are important factors. CNC with higher orientation exhibits enhanced gas barrier properties and piezoelectric properties. Additionally, in the packaging and coating domain, transparency is an important factor as it impacts the perceived quality of the material and impacts the sales and marketing of a product through visual stimulation [5]. Therefore, the research first focuses on obtaining a higher orientation of the CNC in a thin solid film from CNC aqueous gel, which is mainly suitable in the coating industry to enhance gas barrier properties or in the piezoelectric application, where higher alignment is important. This work is focused on the CNC gel phase as this offers the lowest structural relaxation; thus, retaining the orientation during drying is more probable. Further, higher orientation also assists in achieving higher transparency in terms of haze and clarity. The colloidal suspension of CNC exhibits a chiral nematic structure with a helical pitch. Through external forces such as mechanical shear, electrical and magnetic fields, CNC can be aligned. Chowdhury et al. [6] showed that highly aligned CNC film can significantly improve gas barrier properties. However, a higher degree of orientation requires higher shear rates, which also increases the chances of coating defects. Chowdhury et al. [7] reported that to obtain around a parameter of 0.93 order from CNC aqueous gels, a shear rate of 550 – 600 s^{-1} is required. Moreover, the brittleness of these CNC-based films is still a major concern. The effect of different electrolytes on self-assembled CNC film has been thoroughly studied by Parit et al. [8] where the

author reported structural rearrangements to produce a transparent film for a certain electrolyte concentration range. However, the combined effect of ionic strength and the mechanical shearing operation has not been studied yet. In this research, a simple approach is utilized where the addition of electrolytes to CNC aqueous gel prior to mechanical shearing has been explored to develop a highly oriented thin solid CNC film at a low shear rate from CNC aqueous gel.

In the next phase, the research focused on developing self-assembled transparent CNC-based green composite films that are suitable for packaging applications. The self-assembled CNC films exhibit structural color and iridescence, which decreases the transparency in the film. The chiral nematic structure is restored in the self-assembled CNC film during drying, which gives rise to iridescence. Therefore, restricting the formation of the cholesteric phase during self-assembled film formation could be a possible route to developing transparent CNC films. Since the surface charge of CNC plays a crucial role in the formation of chiral nematic structures, tuning the CNC anionic surface charge could affect the internal structural organization in a self-assembled solid film. Parit et al. [8] demonstrated the preparation of transparent CNC film through screening of the CNC's anionic surface charges by the addition of electrolytes by. Also, Abitbol et al. [9] reported significant effects on the phase boundaries and viscosities of CNC dispersion with different surface charge. The dispersion viscosity was found to be higher for lower surface charge. The effective diameter of CNC was also found to be higher for lower surface charge. According to the Stroobants-Lekkerkerker-Odjik (SLO) modified Onsager theory, the electrostatic interaction plays a crucial role in predicting the isotropic to anisotropic phase transition of CNC dispersion [10]. Therefore, modulating sulfate ester moieties can affect the self-assembly in solid films and their properties. Treatment with sodium hydroxide (NaOH) was found to be a suitable approach to partially desulfate CNC as reported by Jordan et al. [11]. Therefore, isotropic CNC dispersions were treated

with NaOH to investigate the effect of partial sulfur removal on the structural properties of self-assembled CNC solid films. Lastly, a CNC and polyvinyl alcohol (PVA) composite was prepared, and a detailed optical property analysis performed to determine the effect of PVA concentration on the NaOH-treated CNC film.

Previously, research has demonstrated the structural tuning of CNC through chemical modification to produce transparent CNC films. However, some practical techniques can also be used to produce CNC based transparent film without chemical doping, such as freeze-thaw and circular shear. Freezing CNC dispersions promotes ice crystal growth through which CNC alignment was noticed after freeze drying or sublimation [12]. However, this method has not applied to produce CNC solid film where all three phase transitions (solid, liquid and gas/vapor) take place. The chiral nematic structure of CNC causes the color in the film, however, through the freeze-thaw technique, anisotropic structure formation can be restricted due to the lack of system entropy. Therefore, this method was utilized on an isotropic CNC aqueous dispersion to develop a CNC based film the morphology and optical properties of which were investigated.

The second part of the research focused on developing a biodegradable, low cost, low maintenance, and sturdy optical sensor by utilizing the CNC's internal chiral nematic structure to detect water concentration in polar organic solvents that can be used in the alcohol dehydration industry. The solid self-assembled CNC film exhibits structural color or iridescence due to its chiral nematic organization. Therefore, CNC can also be used as optical sensors when exposed to different external stimuli conditions such as humidity, pH, solvent, or acid vapors. Humidity sensors are of great importance in different industries such as semiconductors, food, beverage, and pharmaceuticals. Wireless, easy operation, and low-cost humidity sensors can be advantageous in comparison to the current colorimetric humidity indicator which contains cobalt chloride, which

is toxic to humans [13]. To date, significant color changes for different humidity levels has not been exhibited by the humidity indicators that do not contain cobalt chloride [13]. Therefore, an inexpensive, non-toxic humidity indicator is quite important. Similarly, heavy volatile vapors, like ammonia or hydrochloric acid, pose threats to the environment, health, and safety [14]. Electrochemical gas sensors used to detect these are, however, inconvenient in terms of the application complexity and cost [14]. Therefore, inexpensive, sensitive, stable, recyclable, and biodegradable optical vapor/gas sensors are in demand to overcome such difficulties. As for humidity sensors, CNC and polyethylene glycol composites and CNC and graphene oxide have exhibited good responses [15,16]. Although many more routes are available to create CNC-based optical sensors, the scope for improvement regarding cost, stability, and durability is still under research. Polyvinyl alcohol is a low-cost, hydrophilic polymer that can be used with CNC to create a sensor. The thermal crosslinking capability of polyvinyl alcohol can provide the sensor with more stability and make it reusable during operation, whereas the abundance of hydroxyl groups in the structure can serve as the source to absorb moisture easily. Insolubility in polar organic solvents of polyvinyl alcohol also helps this sensor in use for the detection of the concentration of polar organic solvents. In this research, a simple CNC and polyvinyl alcohol composite sensor are prepared and its effectiveness in determining humidity and water concentration ethanol has been studied.

Chapter 1 Literature Review

This chapter provides the background details that are required for the research work. A theoretical background on cellulose nanocrystals, their preparation methodologies, colloidal dispersion behavior, and their application areas are included. Sections 1.1 – 1.4 are focused on an overview of the preparation, morphology, and applications of cellulose nanocrystals. Section 1.5 discusses types of liquid crystal and its microstructure. Lastly, in Sections 1.6 and 1.7 the phase behavior, rheological properties and optical properties of CNCs are detailed respectively.

1.1 Cellulose Nanocrystal

Cellulose nanocrystals are bio-based nanomaterials of width (3 – 70) nm and length (35-3000) nm, produced from cellulose, a natural linear polymer abundantly present on earth [17,18] . The repeating unit of the cellulosic chain, cellobiose, is composed of two anhydro-D-glucose units, connected by β-1,4-linkages [18–21]. These chains are packed into fibrils, containing both amorphous and crystalline regions [19]. The cellulosic structure bears hydroxyl units which impart chirality, hydrophilicity, and biodegradability and form strong hydrogen bonds which creates the crystalline and amorphous regions, multiscale fibrillated structure and imparts cohesive nature to cellulose [18]. CNC can be produced from cellulose containing natural resources such as plants, cotton, tunicates, agricultural waste, algae, and bacteria. [4,22]. Rod-shaped CNC is produced mainly by sulfuric acid hydrolysis where the amorphous portion of the fibre is degraded retaining only the crystalline part. This improves the mechanical strength and modulus, provides high specific area and liquid crystalline properties at higher concentrations [18,23]. Additionally, CNC can have different shapes and morphologies such as needle, lamellar, and whiskers, depending on the raw material, process condition, and drying mechanism [20,24]. The aqueous colloidal suspension of CNC produced through sulfuric acid hydrolysis is found to be stable due to the

presence of the negative sulfate charge on the surface of the CNC particles, which creates electrostatic repulsion between the particles [25–27]. Concentrated colloidal suspensions of CNC produced from sulfuric acid hydrolysis exhibits a chiral nematic (cholesteric) structure with a left-handed helical organization [28,29]. During the evaporation of a CNC suspension, the chiral nematic structure is restored in the dried solid film [30]. In colloidal suspensions, this chiral nematic structure is observable at higher concentrations (anisotropic phase) as at low concentrations, CNC particles are oriented randomly and thus isotopically [31,32]. The chiral nematic phase is of rod-like particles with a helical organization directed towards the alignment direction [28]. A simplified way to explain chiral nematic structure is the stacking of helical organization into the nematic planes [33] shown in **Figure 1.1**. The pitch of the chiral nematic structure can be defined as the periodicity of the helical organization towards the direction of the CNC particle's local alignment [34]. A complete rotation is referred to as 360° whereas 180° is referred to as half-pitch shown in **Figure 1.1** as P/2 [35]. This structure of CNC is dependent on the particle size, surface charge, polydispersity, and liquid medium properties such as pH, ionic strength, and temperature. [17].

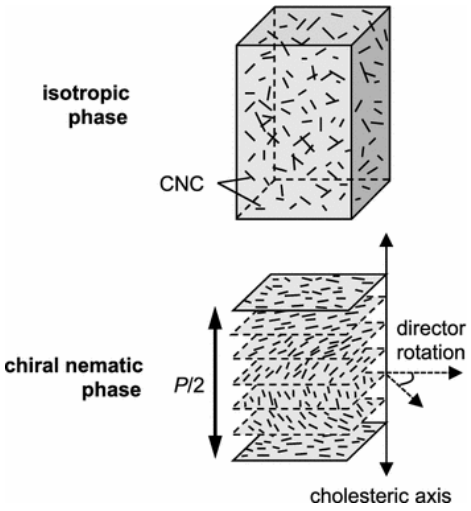

Figure 1.1 Cellulose nanocrystal isotropic and chiral nematic organization [36]

1.1.2 Preparation Methodologies

To prepare CNC from cellulosic fibres, pre-treatment is necessary to remove hemicellulose, and lignin, and separating and purifying the cellulose fibre. The fibres are composed of amorphous and crystalline regions. During acid hydrolysis, the hydrogen ion cleaves the glycosidic bonds of the amorphous part while acid cannot easily penetrate the crystalline region [37]. Ranby et al. [38] first prepared CNC by boiling cotton or wood cellulose fibres with 2.5 N sulfuric acid for 1 – 8 hours followed by washing and centrifugation. Upon washing with water, the pH rose from acidic to neutral, and around pH ~ 4 a colloidal suspension of CNC is formed without changing the crystalline structure [38]. Mukherjee et al. [39] further investigated increasing the concentration of sulfuric acid on cotton and ramie fibre at room temperature in which the author reported that at up to a concentration of 900 g/L acid the crystalline structure was not changed, however a small amount of hydrolysis of the crystals were observed [40]. Further investigations have been done with elevated temperature where 955 g/L sulfuric acid is used on textile fibre at 40 ºC for 24 hours [40]. A yield of 63.8 % was found for cotton pulp, although other sources of pulp generally resulted in low yield [37,41]. Although high dispersibility is the prime advantage of the sulfuric acid hydrolysis process, thermal instability due to the sulfate group is the major shortcoming of these CNC [22,41,42]. Apart from sulfuric acid, CNC can be produced via hydrolysis by hydrochloric acid, a mixture of sulfuric and hydrochloric acid, maleic acid, and phosphoric acid [20,41–43]. Wang et al. [43] reported spherical shaped CNC from microcrystalline cellulose can be formed via hydrolyzing with a mixture of sulfuric and hydrochloric acid under ultrasonic treatment. The ratio of sulfuric, hydrochloric, and distilled water used was 3:1:6. In comparison to the 64 wt% sulfuric acid hydrolysis, spherical CNC formation took place under mild acidic conditions for a longer time [43]. Although the CNC produced is thermally stable, low dispersibility is the disadvantage [42]. While CNC produced from hydrochloric acid is thermally stable, it lacks particle stability due to

low surface charge [22,41]. Hydrolysis with phosphoric acid produced CNC with higher thermal stability and better dispersibility in polar solvents but with lower surface charge [42]. Apart from chemical treatment, CNC can be produced via mechanical treatment as well. Li et al. [44] reported the production of CNC from microcrystalline cellulose by using an ultrasonicator of 1500 W output power. The ultrasonication fractured and fragmented the microcrystalline cellulose after 1 minute and after 10 minutes, the formation of CNC was observed with web-like network formation. The size reduction is achieved by the emission of heat which is caused by cavitation [44]. The loss of crystallinity has been found with longer treatment time [44]. Various experiments showed that the production of CNC is dependent on the concentration of the acid, acid to cellulose ratio, temperature, reaction time, and source of the cellulose [1,41].

1.1.3 Dimension, Morphology, and Sources of CNC

The dimensions and morphology of CNC are dependent on the raw material, along with preparation condition and drying technology. The aspect ratio of CNC mostly depends on the cellulose source as shown in **Table 1.1** [18]**.**

Table 1.1 CNC from various sources and dimensions (modified and adapted from literature) [18]

CNC source	Length nm	Aspect ratio L/D	Note
Wood	100-300	20 to 100	*Produced by H_2SO_4 hydrolysis*
Cotton	10-150	10 to 30	*Produced by HCl hydrolysis*
Ramie	70-200	around 12	*Produced by H_2SO_4 hydrolysis*
Tunicates	>1000	around 100	*Produced by H_2SO_4 hydrolysis*
Bacteria	100-1000	2-100	*Produced by H_2SO_4 hydrolysis*
Bacteria	160-420	7 to 23	*Produced by HCl hydrolysis*

The morphology of CNC depends on the source as well [45,46]. The crystallinity of CNC is also dependent on sources. Korolovych et al. [47] studied CNC morphology from microcrystalline

cellulose (MC), softwood, and hardwood fibres. The crystallinity from MC is the highest among the three. Between softwood and hardwood fibre, hardwood showed a higher crystallinity value than softwood because of its denser structure with the lower amount of lignin and hemicellulose. The morphology of the different cellulose sources is shown in **Figure 1.2**.

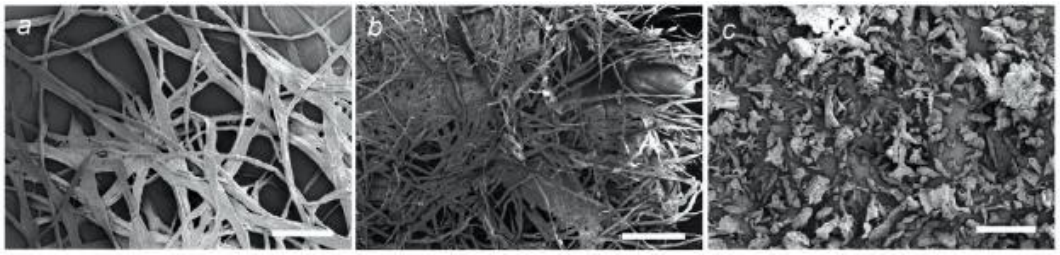

Figure 1.2 Morphology of cellulose from different sources: (a) softwood (b) hardwood and (c) microcrystalline cellulose [47]

1.1.4 Application

The unique structure and properties of CNC make them suitable for many applications such as optical and biosensors, stabilizers, fillers, and biodegradable packaging material [15,48,49]. Industrial applications of CNC are mainly to food, pharmaceuticals, polymers, and energy[3,49]. CNC exhibits mechanical properties such as axial stiffness of 150 GPa, tensile strength of 7.5 GPa, and a high aspect ratio ranging between 10 - 100, which can improve the properties of biopolymers (Polylactic acid, Polyhydroxyalkanoates) into which they are incorporated [4]. Functionalization of CNC is carried out to make it compatible with a hydrophobic polymer matrix. Different pathways, such as polymer grafting [50,51], acetylation, alkylation [52,53], and cationic surfactants [54], have been used to modify CNC as a filler in a PLA matrix to improve PLA's crystallinity and mechanical properties such as tensile strength, and thermal stability. CNC is also found to be useful as a rheology modifier [50]. The anisotropic structure of CNC can be used for coating materials that can improve gas barrier properties [6]. Chowdhury et al. [6] showed that with the increased alignment of CNC crystals, the oxygen and carbon dioxide barrier properties of

polylactic acid film improved. Mechanical shearing of CNC creates a film with close packing of the oriented particles which reduces the permeability of gases. Similarly, shearing of a CNC and polyvinyl alcohol mixture on a polypropylene substrate showed improvement in barrier property up to 30 wt% of polyvinyl alcohol [51]. Goswami et al. [52] used CNC coating to improve the interfacial shear strength in GF–epoxy composite by creating bonding between fibre and matrix through CNC coating. The chiral nematic structure of CNC also results in iridescence which can be used to detect external stimuli such as moisture. Research has been done to make a CNC and polyethylene glycol-based optical sensor for humidity detection [13,15], a spin-coated multi-layered CNC sensor for sensing acid vapor [14], or used as a fluorescence material with CNC [53]. Kelly et al. [54] prepared a CNC and polyacrylamide-based hydrogel for organic solvent detection and CNC and acrylic acid-based pH sensor. Gao et al. [55] studied to the detection of similar types of organic solvents such as ethanol/methanol and 1-propenol/2-propanol with polyvinylpyrrolidone. CNC can also be used as a nanostructure to host other nanoparticles such as silver nanoparticles to detect hydrogen peroxide in wastewater [56]. Amination has been done to CNC based film to detect aldehyde gas through a color change [57]. Though several routes are proposed, industrialization of such sensors is still in process. In addition to this, CNC can be used for piezoelectric sensors [58,59], and super capacitors [60]. The alignment of the crystals gives a piezoelectric property. Although not much research has been carried out on the piezoelectricity of CNC films, several studies have been conducted in establishing the existence of piezoelectric properties in wood fibres. Fukada et al. [61] showed the existence of the piezoelectric effect in wood fibres in 1955. According to the literature, the piezoelectric property in the wood is generated from the crystalline region, therefore the degree of crystallinity and crystal orientations in cell wall are the prime criteria to be considered [62]. The experimental findings related the link between the

degree of crystallinity and orientation of the crystallites with the piezoelectric property. This led to the finding that the alignment of CNC can also exhibit piezoelectric properties. Csoka et al. [63] developed ultrathin film of CNC with electric field shear for sensing piezoelectricity. In addition to this, there are several other domains where CNC is being researched, like, tissue engineering, biomedical engineering, drug delivery system, and biocatalysis [3].

1.2 Liquid Crystal

The discovery of liquid crystals occurred in the year 1888 by the Prague scientist Friedrich Reinitzer with the observation of the double melting point of cholesterol benzoate [64]. Further, German physicist, Otto Lehmann studied this matter with Friedrich Reinitzer and termed it as a liquid crystal that belongs to neither the solid, liquid, or gaseous state. For 75 years it remained of purely academic interest, but the application of liquid crystal began with electronic displays. Even though liquid crystals were present in the 4^{th} century, however, their popularity in the research began from the past 125 years. The liquid crystals are also called mesophases and the mesogen or the anisotropic particles are the building blocks of these mesophases [65].

Liquid crystals are fluidic materials that exhibit long-range order like solids. The order can be either positional or orientational. Liquid crystals can mainly be classified into two categories: thermotropic and lyotropic. Thermotropic liquid crystals are formed by a change in temperature whereas lyotropic liquid crystals are governed by changes in concentration. In this section, only the lyotropic liquid crystal is discussed. The formation of lyotropic liquid crystals occurs when a solvent is added to it. The formation of a liquid crystal takes place either by penetration of liquid into the crystal lattice without breaking the crystals or by addition of a suitable solute in an isotropic solvent which can form oriented aggregates upon increasing solute concentration [66]. In lyotropic liquid crystals, the building blocks could be amphiphilic which form micelle by

aggregation. Examples of such constituents are surfactants and amphiphilic lipids [64]. Non-amphiphilic anisometric macromolecules such as viruses, inorganic rods or discs in colloidal suspension can also form the liquid crystal phase [64].

1.2.1 Microstructure

Three different microstructures of LC phases (mesophases) were reported by Friedel in 1922 i.e., smectic, nematic and cholesteric [67]. The nematic phase exhibits long-range orientational order, however, it does not show any long-range positional order. Here, the local orientation of the macromolecule has been observed along the director n shown in **Figure 1.3**. For the smectic microstructure, the nematic orientational order is maintained, but the macromolecules also align themselves into layers or planes, therefore the smectic phase also exhibits long-range positional order. In the smectic phase, molecules can move from one layer to other. For the cholesteric phase, a slight twist in nematic structure along the axis perpendicular to director n is observed. CNC exhibit a cholesteric (chiral nematic) structure, where a left-handed helical structure with pitch length P is observed.

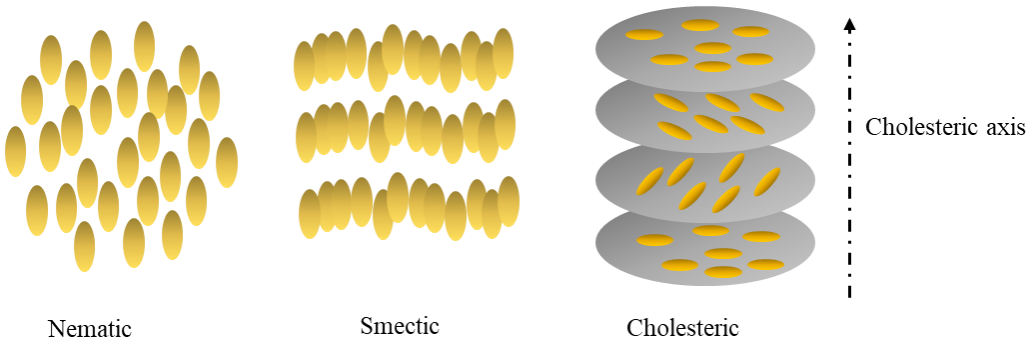

Figure 1.3 Microstructure of liquid crystal

1.2.2 Onsager and Stroobants, Lekkerkerker, and Odijk (SLO) Theory

The first theoretical model developed by Onsager in the year 1949, based on hard repulsion of Tobacco Mosaic Virus (TMV), was significant in explaining the phase behavior of liquid crystals. The theory was developed considering the excluded volume interaction of monodisperse spherocylinders with only hard rod interactions [68,69]. As hard rods cannot interpenetrate, adjustment to the excluded volume governed by the rods orientation which can be ascribed to the loss and gain in orientational and translational entropy in the system. Based on the theoretical model, formation of liquid crystalline phase occurs when excluded volume between rods are minimized through transformation of their orientation from perpendicular to parallel by gaining translational entropy. Onsager predicted that for perfect neutral rigid rods, the critical concentration is dependent on the aspect ratio (L (length) /D (diameter)). The equation from Onsager theory to predict Φ_I (first critical concentration for isotropic to biphasic domain) and Φ_N (second critical concentration for biphasic to liquid crystalline domain) are indicated below.

$$\Phi_I = 3.34\frac{L}{D}$$

Equation 1.1 Onsager's theory (isotropic to biphasic)

$$\Phi_N = 4.49\frac{L}{D}$$

Equation 1.2 Onsager's theory (biphasic to liquid crystalline)

Since Onsager's theory is based on an ideal case, it is not possible to predict the phase behavior of CNC suspension. However, the CNCs are charged particles with polydispersity. Therefore, the effect of electrostatic repulsive force and polydispersity needs to be considered along with the aspect ratio to predict phase behavior accurately [32]. A more accurate prediction of phase separation of rodlike polyelectrolyte particles was developed by Stroobants, Lekkerkerker, and

Odijk (SLO) and Onsager's theory combined with SLO theory introduces the effective diameter (D_{eff}) and twisting factor/parameter (h) because of electrostatic repulsion as two more factors to predict phase behavior [32]. With increasing ionic strength, the effective diameter decreases due to the screening of the double layer. Also, this repulsive force favors a perpendicular orientation which could be seen as a twisting action between rods. By considering SLO theory, the critical concentration of isotropic (C_i) and anisotropic (C_a) phases can be written as

$$C_i = 3.290[(1 - 0.675h)b]^{-1}$$

Equation 1.3 Stroobants, Lekkerkerker, and Odijk (SLO) modified Onsager's theory (isotropic to biphasic)

$$C_a = 4.191[(1 - 0.730h)b]^{-1}$$

Equation 1.4 Stroobants, Lekkerkerker, and Odijk (SLO) modified Onsager's theory (biphasic to liquid crystalline)

Here, b is the second virial coefficient of the system and concentrations are expressed as the number density of rods, and b and h can be calculated from the following equations:

$$b = \frac{\pi}{4} L^2 D_{eff}; h = \frac{\lambda_D}{D_{eff}}; \; D_{eff} = D + 5.54\lambda_D$$

Equation 1.5 Stroobants, Lekkerkerker, and Odijk (SLO) modified Onsager's theory, second virial coefficient, twist parameter and effective diameter determination.

where, λ_D= Debye length and D is CNC rod diameter [32,70].

1.3 Phase Behavior and Rheological Characterization of Cellulose Nanocrystal

1.3.1 Phase Behavior

Lyotropic liquid crystals exhibit phase transitions under the influence of varying concentrations of anisotropic mesogen in the solvent [68]. The phase boundary is dependent upon the aspect ratio (L/D) of the rod-shaped particles. For low particle concentration, isotropic phase forms which can

be divided into the following three regimes: dilute, semi-dilute and concentrated isotropic phase. At a very low concentration, the rod particles form a dilute phase where free motion is observable due to Brownian motion [65,68]. With increasing concentration, a semi-dilute phase is formed which restricts the motion of the particles. Further, an increase in concentration forms concentrated isotropic phase where the particle movement is constricted to a small volume. Next, with increasing concentration to Φ_I (critical rod concentration), a biphasic system is observed where some rod particles form an anisotropic phase which stays in equilibrium with the isotropic phase. Further, with higher concentration, the anisotropic region increases and at Φ_N (second critical concentration), the system becomes completely liquid crystalline [65]. The schematic of the phase behavior is shown in **Figure 1.4**. Although research is ongoing to develop a widely accepted theory to explain this phase behavior, this can mainly be explained via Onsager theory.

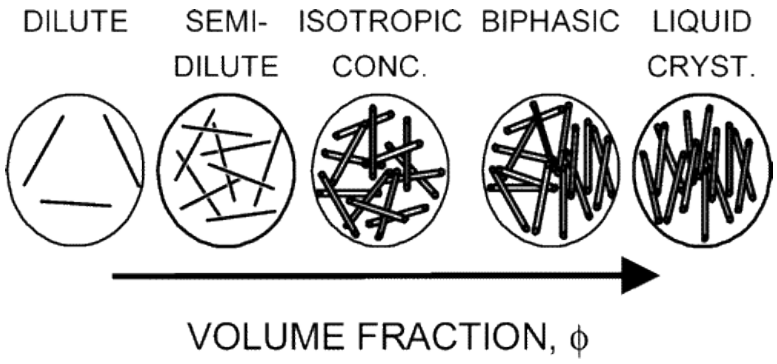

Figure 1.4 Phase behavior of CNC dispersion [71]

This phase behavior of LC with increasing concentration is dependent on a decrease in rotational entropy combined with an increase in translational entropy due to alignment [69]. Further, the concentration of Φ_I and Φ_N is dependent on the aspect ratio and solvent quality.

The CNC suspension forms a cholesteric or chiral nematic structure at the liquid crystalline phase. This chiral nematic structure exhibits fingerprint texture under cross-polarized microscopy. Dong

et al. [32] experimentally showed the dependency of the volume fraction of the anisotropic phase in the biphasic system on the total CNC suspension concentration. The increase in the anisotropic volume fraction is observed with increasing CNC suspension concentration. The author reported that the phase transition occurred at the following critical concentration, Φ_I = 4.55 wt% and Φ_N = 13.13 wt% [32]. Further, Ureña-Benavides et al. [72] reported Φ_I and Φ_N is a function of CNC concentration and found that Φ_I and Φ_N occur around 2.7 vol% and 11.2 vol% respectively for aqueous dispersion of cotton-based CNC. The author also reported to observe the presence of small isotropic domains in between 7.69 vol% to 10.4 vol% which posed challenge in estimating the exact Φ_N. The polarized light microscope image in **Figure 1.5** exhibits the birefringent character for increasing CNC concentration.

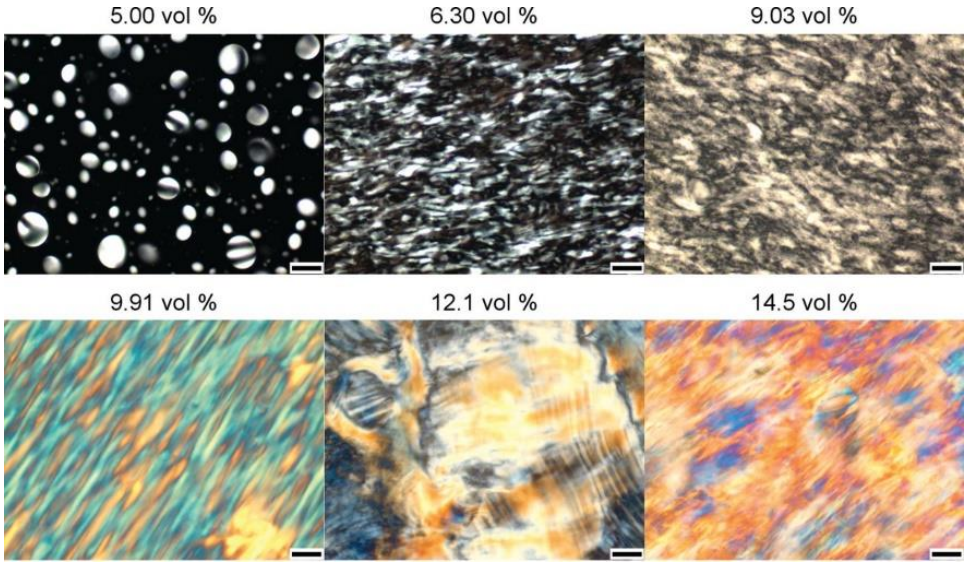

Figure 1.5 Polarized images of CNC dispersion at different concentrations; 50 µm scale bar [72]

At 14.5 vol%, a very bright and random color is obtained which is later understood to be the gel phase by rheological characterization. The changing ionic strength is also an important factor to be considered when determining phase behavior. Dong et al. [32] showed that with constant ionic

strength of the suspension, linearity can be obtained between the volume fraction of anisotropic phase and the total concentration. This further proves that with increasing total CNC suspension, the counterion also increases which increases the ionic strength of the system, thus lowering the effective diameter of the CNC particle. Therefore, for CNC suspensions, if the ionic strength is not kept constant, linearity is not observed between volume fraction and total concentration. The author also reported the significant suppression of the anisotropic fraction in the biphasic region by the addition of electrolytes for fixed total CNC concentration. This effect is similar for acidic, i.e. HCl and neutral electrolytes such as NaCl, KCl [32]. The addition of electrolytes decreases the pitch length and doubles the value of the twist parameter, indicating the presence of higher chiral interaction. The results obtained from the experiments were found to be in accordance with Stroobants, Lekkerkerker, and Odijk (SLO) theory. Dong et al. [73] experimentally demonstrated that the presence of counterions can affect the phase behavior of CNC suspension. In this regard, transition of isotropic to biphasic (Φ_I) domain formation was observed at 4.9 wt% for H^+ whereas in the presence of Na^+ this concentration was found to be 5.3 wt%. Again, when comparing the results between Na^+, K^+ and Cs^+, it was found that Cs^+ exhibited higher Φ_I. The phase behavior based on these counterions is dependent on their hydration number. These hydrated ions bond with the negative surface charge of CNC and create repulsive forces. When the repulsive force is higher, lower Φ_I is expected and the magnitude of the repulsive force is directly proportional to the counterions hydration number which is in the following order i.e., $Na^+ > K^+ > Cs^+$. According to Honorato-Rios et al. [74] addition of electrolyte screens of the electric double layer which in turn reduces effective diameter as well as the effective volume of each rod. Although the effect of different counterion and electrolytes on phase behavior is clearly visible, the explanation of the effect is still under investigation. Further, Haywood et al. [75] reported the effect of the source of

cellulose, counterion and solvent affects the CNC phase behavior as well. The formation of fully liquid crystalline and gel phases occurred at 6.50 vol% and 7.16 vol%, respectively for CNC from woody biomass with Na^+ and dispersed in D_2O (deuterium oxide) whereas for cotton extracted CNC with H^+ counterion dispersed in water, the phase transition concentrations for the liquid crystalline and gel phases were 12.4 vol% and 14.5 vol%, respectively [75]. Onsager theory proposed phase behavior for neutral perfect rigid rods which is dependent on aspect ratio. However, when discussing CNC particles, the presence of surface charge needs to be considered and therefore, the phase behavior cannot be predicted accurately with only Onsager theory. Not only polydispersity but increased ionic strength with increasing CNC concentration reduces the effective diameter of the CNC. In this case, Stroobants, Lekkerkerker, and Odijk (SLO) modified Onsager's theory can be used to predict phase behavior which introduces two factors i.e., effective diameter and twisting factor resulting from electrostatic repulsion [32]. Therefore, to summarize, dependency of CNC suspension phase behavior depends upon the CNC source, aspect ratio, polydispersity, ionic strength/counterions and solvent of the suspension.

1.3.2 Rheological Behavior

Rheological characterization of CNC suspensions has been carried out by several authors who have explained the behavior based on concentration and the effect of counterions. The phase behavior of CNC suspension can be characterized by rheological studies as well. Ureña-Benavides et al. [72] observed Newtonian behavior at very low suspension concentrations. For the biphasic region, three-region behavior is observed and for the liquid crystalline and gel phase complete shear thinning has been observed which follows the power law. This observation is in line with Sabet et al. [76] and Haywood et al. [77] shown in **Figure 1.6**.

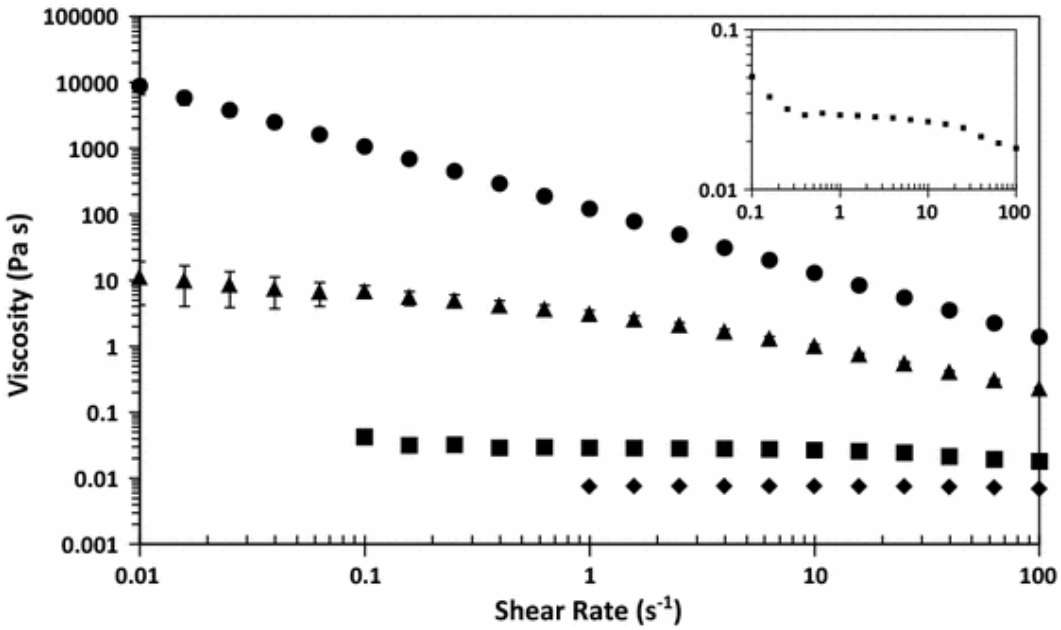

Figure 1.6 Steady shear viscosity of CNC suspension for shear rate range; Diamond - 3.27 vol%, Square - 6.98 vol%, Triangle - 11.6 vol%, Circle - 15.8 vol% [77]

For, 3.27 vol% (isotropic), nearly Newtonian behavior is observed. The three-region behavior associated with biphasic concentration i.e., 6.98 vol% is consistent with lyotropic liquid crystalline behavior described by Onogi et al. [78]. The shear-thinning behavior in Region-I is associated with the variation in poly-domain texture or tumbling under shear. Region-II depicts plateau behavior due to "vorticity alignment" or wagging and Region-III is associated with complete alignment of mesogens in the shear direction which results in shear-thinning [77]. For 11.6 vol% and 15.8 vol%, complete shear thinning is observed for all shear rates. The oscillatory measurement showed that for 15.8 vol%, $G' > G''$ for all frequencies confirming the gel structure at this concentration. As for the 11.6 vol%, predominantly viscous behavior is observed ($G'' > G'$) with the strong dependency of G' on frequency [77]. This observation is in accord with Ureña-Benavides et al. [72] where the author mentioned obtaining dominant elastic behavior i.e., $G' > G''$ for concentrations above 12 vol%. Independent behavior of G' with frequency range indicates the

transition to the gel structure which is observed from 14.5 vol% [72]. One important characteristic to mention is that CNC suspensions do not show any shear viscosity maxima over the concentration range in the biphasic region which is the hallmark for liquid crystalline polymeric behavior [69,72,79]. In this case, a slight decrease in shear viscosity is observed at the liquid crystalline phase with an increase in concentration shown in **Figure 1.7**. Apart from this, a continuous increase in shear viscosity up to the liquid crystalline phase and then plateau formation in the gel phase is observed for sulfonated CNC shown in **Figure 1.7.** Similarly, for other charged rod-like dispersions like halloysite and chitin, the viscosity versus concentration curve failed to exhibit a maximum.

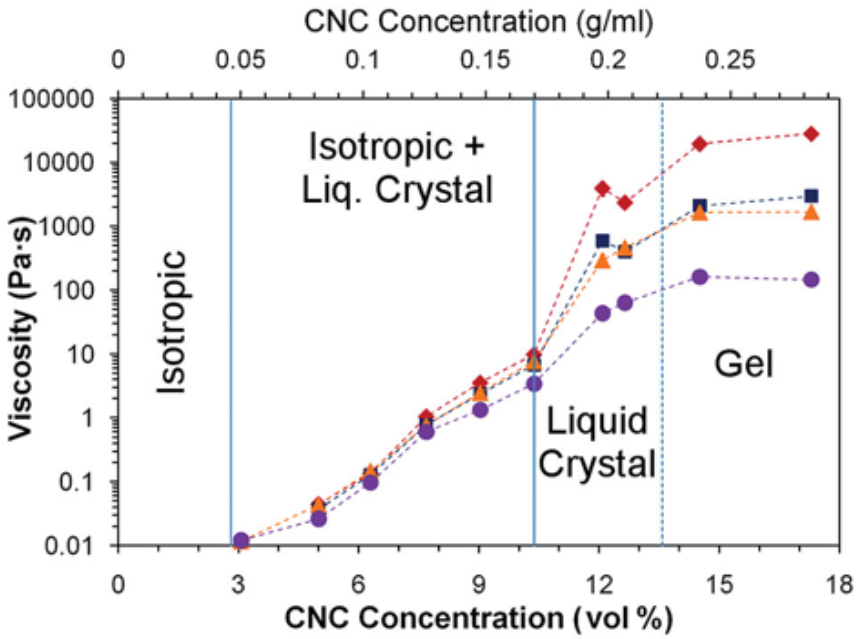

Figure 1.7 Steady shear and complex viscosity over range of CNC concentration; Color code: red - 0.1 rad/s, blue - 1.0 rad/s, orange - 0.1 s^{-1} and purple - 1 s^{-1} [72]

This behavior is not fully understood for charged rod like dispersions, however, Li et al. [80] related it to the electro-viscous effect where distortion of the electric double layer occurred under

shear. Further, the critical concentrations are not independent of the total concentration which could be another reason for this behavior. The effect of ionic strength on the rheological aspect of CNC aqueous suspension is characterized by Sabet et al. [81], who reported that the addition of (0 – 10) mM of NaCl to isotropic CNC suspension of 3 wt% concentration resulted in lowered steady shear viscosity due to lowered electro-viscous effect as NaCl compresses the double layer. The biphasic region i.e., 7 – 10 wt% concentration, showed an increase in viscosity for low shear rate i.e., in the region I and decrease in viscosity for higher shear rate domain for 0 – 5 mM NaCl addition. The increase in the liquid crystalline region contributes to the higher viscosity at a lower shear rate. Again, the interaction of individual CNC particles decreases the viscosity at higher ionic strength for a high shear rate region. For 10 mM and 15 mM of NaCl, higher viscosity with the single shear-thinning region is observed for higher particle aggregation due to the collapse of the double layer. For gel concentrations above 11 wt%, an initial drop in shear viscosity was observed due to the disturbance in the hydrogen bonding which results in a weaker gel structure. Further, an increase in NaCl concentration beyond 5mM resulted in an increase in viscosity due to particle aggregation. The effect of temperature on the rheological behavior of CNC suspension has been observed beyond 40°C for biphasic and liquid crystalline regions where at a low shear rate, an increment in shear viscosity in region I is observed [76]. The cause of this is still not understood, however, Sabet et al. [76] attributed this to the occurrence of a higher packed chiral nematic structure with lower pitch size at higher temperatures [82]. The temperature results from the liquid crystalline region is in accordance with Ureña-Benavides et al. [72]. Ureña-Benavides et al. [72] reported an increase in shear viscosity of the 12.1 vol% CNC suspension at 40°C and observed a significant increase in the isotropic domain through hot stage microscopy between 35°C to 40°C. The change in microstructure confirms that the change in viscosity is not an artifact and occurs

due to change in microstructure. Apart from this, CNC suspensions at higher concentration i.e., biphasic and liquid crystalline phases exhibit failure of the Cox-Merz rule as expected. For the isotropic domain, the deviation between steady shear viscosity and complex viscosity is not much higher, however, the difference becomes prominent at higher concentrations for a range of shear rate/frequency [72,76]. In the case of the biphasic domain, at a low shear rate, the difference between steady shear and complex viscosity is not very high but eventually becomes pronounced at a higher shear rate due to the presence of an isotropic phase in the biphasic phase. However, for the liquid crystalline phase, the difference is observed for the entire shear rate/ frequency range. Throughout the above discussion, many aspects of CNC suspension, primarily in water, are discussed, where the phase behavior of the dispersion is further characterized by rheology. A few special characteristics are observed for liquid crystal or mainly for the liquid crystalline polymer are three region flow behavior, maxima and minima in shear viscosity vs. ranges of concentration plot, not obeying Cox-Merz rule, and the requirement of long oscillatory transient before reaching of steady-state and exhibiting sign change for first normal stress difference for increasing shear rate. Ureña-Benavides et al. [72] observed three regions of flow behavior in the biphasic region. Similarly, for whisker shaped CNC, Bercea et al. [83] observed three region behavior in the biphasic domain as well. Haywood et al. [75] also noticed the same behavior for CNC with Na^+ counterion dispersed in D_2O and attributed this behavior to the differences in shear response between the isotropic and anisotropic domain in the biphasic domain. Further, this could also be attributed to the presence of the electro-viscous effect, which is present for the charged mesogens, however, the effect is not fully understood and is still subject to research. Similarly, the absence of a maximum in shear viscosity over concentration range has also been observed for CNC suspensions which is a hallmark for liquid crystalline polymers. For whisker shaped CNC

dispersions, Bercea et al. [83] showed the short transient time requirement for reaching steady state which contradicts the behavior of classical liquid crystals. In terms of relaxation of microstructure after cessation of shear, Haywood et al. [77] experimentally showed the low retention of shear structure for the biphasic domain whereas for a liquid crystalline state the retention time of the sheared structure is higher than biphasic. However, given enough time ~ 17 min, the sheared liquid crystalline phase also returns to its original state. As of for gel phase, though the optical contrast or order parameter is found to be lower than biphasic and liquid crystalline as the breaking of gel structure needs higher shear force, the retention is much higher as the aligned gel structure is quickly reformed. Finally, for preparations of sheared films, the liquid crystalline phase showed retention of the alignment in the early drying stage, the phase goes to gel state which locks the aligned structure. This informs that for using CNC for processing or application, understanding phase behavior and its flow properties are important. Many parameters that affect the phase behavior are discussed, however, the reasoning of all such behavior cannot fully be explained. Further, associated flow behavior also poses challenges to explain certain characteristics as these are dependent on many other factors, such as microstructure, presence of surface charge, the effect of increasing ionic strength with concentration etc. Additionally, measurement conditions such as evaporation, sample history etc. can also affect the result. Therefore, further investigations are still needed to comprehend these behaviors in more detail.

1.4 CNC Solid Film

Self-assembled CNC films display structural color or iridescence as the chiral nematic structure becomes restored while air drying as observed by Revol et al. [31]. Polarized light microscopy showed random localized multicolored domains in such CNC films as shown in **Figure 1.8.** A typical reflectance or transmittance profile was also identified due to the circular polarization of

the light. The reflectance peak of CNC film can be directly correlated to the cholesteric pitch which showed dependency when plasticizer or polymer was added. Multiple studies have shown a red shift of reflectance spectra through addition of materials such as polyethylene glycol, glycerol, and glucose[15,84]. Pan et al. [85] demonstrated that different factors such as temperature, ionic strength, concentration, and magnetic field impact the chiral nematic pitch. Even though CNC self-assembled films provide valuable optical properties, shrinkage and cracking, non-uniformity, and variability in thickness through capillary action are crucial challenges to overcome. In the case of producing aligned CNC film, the application of external forces such as mechanical, electrical, or magnetic shearing can be used. Further, the addition of electrolytes to the CNC dispersion or modulating dispersion pH can also transform the chiral nematic to nematic structure to produce transparent nematic films.

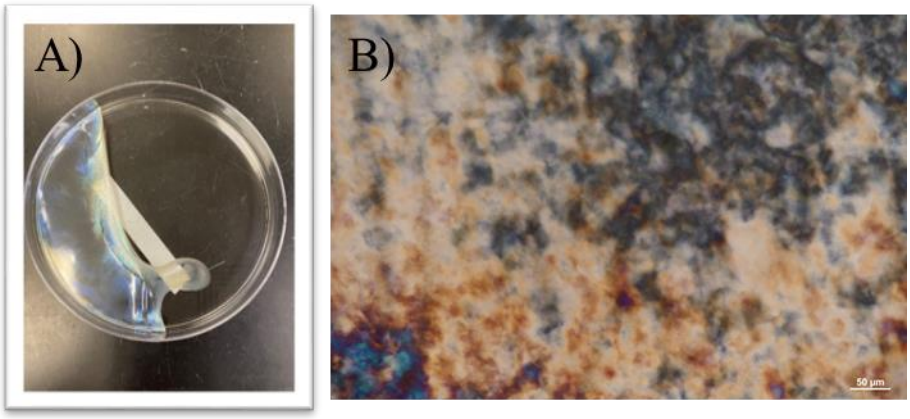

Figure 1.8 A) Self-assembled CNC film B) Cross polarized microscopic image of self-assembled CNC film; scale: 50 µm.

Many applications of CNC require alignment such as coating to provide enhanced gas barrier properties, improved transparency and piezoelectric properties. Previously, reported literature showed the alignment of CNC from different phase behavior and retention of the orientation during drying. In 2012, Reising et al. [86] demonstrated the occurrence of CNC alignment under the

influence of mechanical shear and reported increases in mechanical properties when measured in the shear direction. Later, Chowdhury et al. [7] showed with increasing shear rate, higher CNC alignment can occur in the final film. The concentration of CNC aqueous dispersion at 11.8 wt% was used to minimize the structure relaxation during drying. A detailed investigation was performed by Haywood et al. [77] which showed highest CNC alignment can be obtained from the liquid crystalline phase, shown in **Figure 1.9**. The film image from CNC gel showed multicolored domains suggestive of lower alignment. Further, the dark lines in the images were the cracks propagated in the shear direction posing challenges in the practical application.

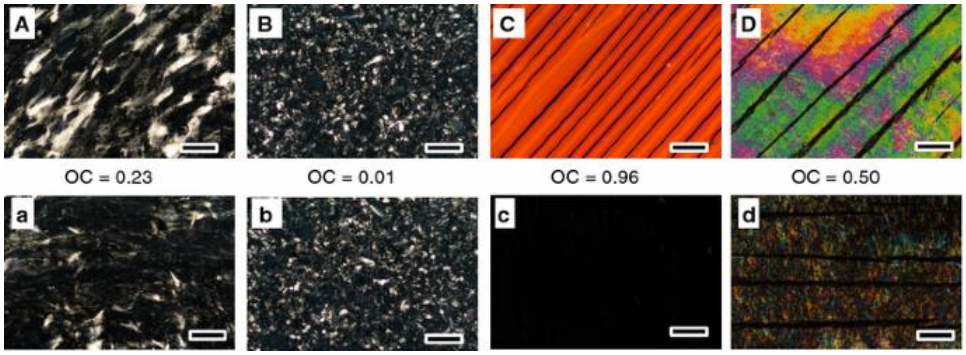

Figure 1.9 Aligned CNC film by doctor blade coating at 100 s^{-1} – a) 3.27 vol%, b) 6.98 vol%, c) 11.6 vol%, d) 15.8 vol%; (A-D) 45º and (a-d) 0º [77]

The structure relaxation plays an important role when preparing aligned CNC films. Post shearing structure relaxation is depicted in **Figure 1.10**, which shows a much faster decrease in alignment for the liquid crystalline phase than the CNC gel phase. Therefore, even though the liquid crystalline phase can provide the highest alignment for low shear, within 20 minutes all the alignment will have dropped to no alignment, thus retaining the alignment in the dried film is challenging. More uniform birefringence as observed through cross polarized microscopy was found with increased orientation, shown in **Figure 1.10.** Further the author reported the formation of poly-domain structure for wet gap thicknesses higher than 250 microns.

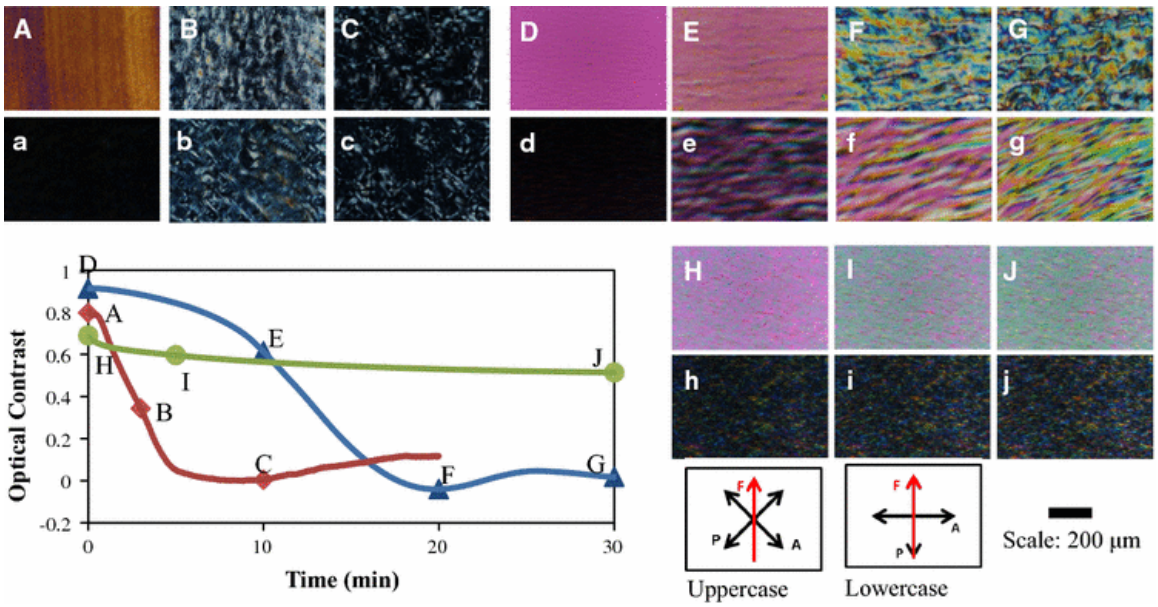

Figure 1.10 Cross-polarized images of CNC dispersion under 100 s^{-1}, Red - 6.98 vol%, Blue - 11.6 vol% and Green - 15.8 vol%; Structure relaxation through optical contrast [77]

Chapter 2 The Combined Effects of Electrolyte Addition and Mechanical Shearing on Cellulose Nanocrystal Alignment

2.1 Background

Cellulose nanocrystals (CNC) are produced from cellulosic feedstocks such as cotton, wood, plants, tunicates, agricultural waste, algae, fungi, and others. [18,87–89]. Natural abundance, biodegradability and renewability, coupled with outstanding mechanical properties, liquid crystalline phase behavior, and other intriguing properties, make CNC a promising candidate for many engineering applications. Promising applications include films, coatings, polymer additives to increase mechanical strength [18,90], optical devices, optical sensors to exhibit a color change under the influence of external stimuli [14,15,91], and rheology modifiers [50].

Typically, sulfuric acid hydrolysis is used to extract CNC from biomass. This process yields rod-like CNC particles with an anionic sulfate ester group [-O-SO3-] on the CNC surface, which stabilizes aqueous CNC dispersions. [18,20,25,26,87]. The counterion is typically H^+ for laboratory made materials and Na^+ for commercially produced CNC [92]. The exact size and surface chemistry of the CNC are dependent on the biomass source and extraction conditions. Aqueous dispersions of sulfated CNCs exhibit lyotropic liquid crystalline phase behavior. With increasing concentration, the dispersions progress from isotropic to biphasic to liquid crystalline and finally a gel phase [93]. CNC's ability to form liquid crystals is of particular interest because they have chiral nematic ordering, which can be exploited to produce iridescence or structural color upon drying [82,94,95]. In addition, it facilitates achieving CNC orientation in the flow direction in shear cast films. In accordance with Onsager's theory, the concentrations at which the dispersions transition from isotropic to biphasic (where an isotropic phase exists in equilibrium with a liquid crystal phase) and from biphasic to liquid crystalline primarily depend on the CNCs'

length-to-diameter ratio (aspect ratio). However, size, polydispersity, the amount and type of counterions, and solvent-rod interactions also affect CNC dispersions' microstructure and phase boundaries [68,72–75,95–97]. For example, when the ionic strength of the medium is increased, the electrostatic double layer is compressed, and the sulfate half-ester groups can be neutralized. This can result in changes in phase boundaries, cholesteric pitch, and dispersion stability [95,98].

Much of the literature has focused on retaining aqueous CNC dispersions' cholesteric microstructure in dried films for sensing, anti-counterfeiting, and selective optical filter applications. However, using shear to unwind the pitch enables alignment of the CNC along the flow direction enabling higher Young's Moduli and enhanced clarity. Both these properties can be relevant for free-standing films and using CNCs as a coating to increase gas barrier in packaging applications. [6,90,93] and in piezoelectric applications [63,99]. Further, transparency is an important factor for visual appeal particularly affecting the sale and marketing of a product [5]. CNC crystal alignment in shear-cast films is primarily dependent on CNC concentration, shear rate, and wet gap thickness. For low to moderate shear rates, the liquid crystalline phase exhibits a higher initial alignment in the shear direction than the isotropic or gel phase. This is due to the liquid crystalline phase exhibiting a higher initial degree of alignment and allowing for more rod mobility than the higher viscosity gel phase [77]. However, the same mobility that facilitates the initial alignment in the shear direction also results in faster microstructural relaxation compared to films prepared from gels. These relaxation effects become more acute for thicker films and longer drying times and can result in films prepared from CNC gels having greater alignment in the flow direction than those prepared from liquid crystalline dispersions. Haywood and Davis 2017 [77] reported an 11.6 vol% liquid crystalline dispersion of cotton CNC had 30% higher alignment than the 15.8 vol% gel immediately after shearing at 100

s^{-1}. However, after a mere 10 min, the degree of orientation of the gel was greater. Relaxation time effects are particularly acute for thicker films that take longer to dry. Chowdhury et al. [7] reported a shear rate of (550 – 600) s^{-1} could be used to achieve a 0.93 film order parameter from a CNC gel. These relatively high shear rates induce localized defects and non-uniformity in the coating [100,101]. These defects, combined with CNC film shrinkage [102,103] and brittleness [104,105], are major obstacles to their practical application.

The effect of the additions of different electrolytes on self-assembled (drop-cast) CNC films have been widely reported [8,106]. CNCs' chiral nematic to nematic transition depends on electrolyte type and interaction, and transparent CNC films can be obtained with optimum electrolyte addition [107]. The effect of electrolytes depends on their cationic bridging strength with the sulfate ester group. Higher interaction has been found for softer cations in monovalent ions, representing the lower critical concentration to exhibit aggregating behavior [108]. $Li^+ > Na^+ > K^+ > Cs^+$ is the monovalent ion order based on their critical aggregation concentration. Additionally, higher valency cations such as Ca^{2+} showed higher efficiency in showing aggregating behavior, indicating higher bridging strength with the anionic sulfate ester group [108,109].

In this work, we investigated the combined effects of electrolyte addition and mechanical shearing on the alignment of CNC in thin shear- cast CNC films prepared from aqueous CNC gels. The gel phase of CNC was chosen due to its slow structural relaxation, which helps retain orientation during drying. We focused on achieving higher CNC alignment at a low shear rate to avoid coating defects reported by others at high shear rates. The addition of electrolytes to CNC gel was studied rheologically and systematically based on size (NaCl, CsCl), valency (NaCl, $CaCl_2$), and pH (NaCl, NaOH) of the electrolytes. We demonstrated that these electrolyte-added CNC gels produce highly oriented thin films when sheared at a very low shear rate. The resulting films also exhibited

transparency and low haze compared to neat CNC films. To the best of our knowledge, this is the first-time mechanical shearing on electrolyte-added CNC gel has been explored to prepare highly aligned CNC film at low shear.

2.2 Materials and Methods

An 11 wt% sulfated cellulose nanocrystal (CNC) aqueous gel with sodium counterion and 1.1 wt% sulfur content was purchased from the University of Maine (Lot number 2021-FPL-CNC-170). The measured length and width of the CNC were 164 ± 37 nm and 5.4 ± 1.7 nm, respectively. Four different high-purity analytical grade anhydrous electrolytes: sodium chloride (NaCl), cesium chloride (CsCl), and sodium hydroxide pellets (NaOH), were purchased from BTC chemicals, and calcium chloride ($CaCl_2$) was purchased from TCI chemicals. These four electrolytes were chosen to demonstrate their effect based on the size (NaCl, CsCl), valency (NaCl, $CaCl_2$) and pH (NaCl, NaOH).

2.2.1 Sample Preparation

The samples were prepared by high-speed magnetic stirring of the as received CNC gel with the electrolytes for 2 hours. Aqueous electrolyte solutions were prepared first and then added to the gel prior to mixing. The final CNC concentration in the sample was maintained at 10.5 wt%. The average transition concentration was used for the electrolyte addition which was determined using the method of Parit (2021) [8] and listed in **Table 2.1**. The transition concentration of the electrolyte is defined as the concentration range where CNC's chiral nematic structure collapses by the double-layer screening without causing particle aggregation. Beyond this range, attractive forces dominate, resulting in dispersion instability and aggregation. The transition concentration ranges vary depending on the electrolyte type and their interaction capability with the anionic sulfate ester group on the CNC surface. The transition concentration of each electrolyte was used

to ensure a common basis for comparing the results as the effect would be different for all the electrolytes at the same concentration (comparison between NaCl and $CaCl_2$ at 0.12mmol/g is shown in **Figure 6.6 (Appendix A)**). The homogenous mixture of CNC and electrolyte was used for film formation and rheological characterization.

Table 2.1 Transition concentration range for the electrolytes

Electrolyte	Range (mmol/g)	Average Concentration used (mmol/g)
NaCl	0.46 – 0.50	0.48
CsCl	0.36 – 0.40	0.38
$CaCl_2$	0.11– 0.13	0.12
NaOH	0.46 - 0.50	0.48

2.2.2 Film Formation

Homogenous mixtures of CNC and electrolytes were cast on polyvinyl butyral (PVB) substrate and sheared using an MSK – AFA – II Automatic, thick film coater (traverse speed range: 0 – 100 mm/sec), and the film applicator maintained a fixed gap of 0.45mm. Three different shear rates were applied to prepare the films, i.e., approximately 20 s^{-1}, 40 s^{-1}, and 100 s^{-1}. Finally, the films were dried in an oven at 40°C. Self-assembled CNC films were prepared by pouring 20 g CNC aqueous dispersion (concentration 2 wt%) in a Petri dish and allowing it to dry for 2-3 days under ambient conditions.

2.2.3 UV-Vis Spectrophotometer

A Thermo Scientific Genesys 10S UV−vis spectrometer with a wavelength range of 200−800 nm was used to collect the transmission spectra of prepared films within 400 – 680 nm range. A birefringence method established by Chowdhury et al.[7] was implemented to calculate the order parameter, which quantifies the present degree of crystal alignment in the film. A sandwich structure of two linear polarized films (American Polarizers, Inc. AP42-007T) perpendicular to

each other was used as cross polarizer setup. The shear cast films were placed between the sandwich structure to measure maximum light transmission intensities for 0° (I_{min}, dark field) and 45° (I_{max}, bright field) configurations. These two intensity values were incorporated into **Equation 2.1** to calculate order parameters (S) [6,7,51].

$$D = \frac{I_{max}}{I_{min}} = \frac{2S + 1}{1 - S}$$

Equation 2.1 Order parameter evaluation

Further, unpolarized light transmittance profile of 100 s^{-1} shear cast films were also performed for the wavelength range 200-800 nm.

2.2.4 Thickness Tester

A thickness tester, Testing Machine Inc. Model 49-71, with a range of 0 – 1.25 mm, was used to obtain the thickness of the films. A minimum of four measurements were taken to calculate the average thickness of the films with the standard deviation listed in **Table 2.2.**

Table 2.2 Average Film Thickness, data given for 100s^{-1} sheared films

Sample	Film Thickness, µm
Pure CNC	35.00 ± 1.41
NaCl	25.25 ± 1.50
CsCl	25.00 ± 2.16
$CaCl_2$	28.00 ± 2.94
NaOH	25.75 ± 0.96

2.2.5 Zeta Potential

A Zeta sizer Nano ZS, Malvern instrument was used to determine the zeta potential of the samples, prepared by mixing 1.66 wt% CNC dispersion with the electrolytes at their average transition concentration for 2 hours. Three measurements were taken to calculate the average and standard deviation.

2.2.6 Rheological Characterization

A rotational rheometer, ARG2 from TA Instruments, was used to characterize the microstructure and flow properties of the dispersions. All tests were performed using a parallel plate fixture (PP40, diameter 40 mm, gap 500 μm) and evaporation blocker at 20°C. Amplitude sweeps starting at 0.001% strain with fixed angular frequency of 6.283 rad/s were used to determine the linear viscoelastic region (LVR) (**Figure 6.1 (Appendix A)**) of each dispersion. The structural stability with time was observed from an oscillatory time sweep measurement conducted within the linear viscoelastic region (LVR) at 1% strain and an angular frequency $\omega = 1$ rad/s. Frequency sweeps were conducted within the LVR with the angular frequency range from 0.1 rad/s to 100 rad/s. The steady state shear viscosity was measured at increasing shear rates from 0.1 s^{-1} to 1000 s^{-1} for each sample. Further, to confirm the absence of any artifacts (fixture and gap), the same experiments were conducted for pure CNC gel and NaCl sample with 800 μm size and 60 mm diameter/ 1° cone and plate geometry (refer to section **Figure 6.2 (Appendix A)**).

2.2.6 Cross-polarized Microscopy

A Nikon (Melville, NY) Eclipse Ni microscope equipped with a Nikon DS-RI2 camera and 20×/0.45 LU Plan Fluor objective were used to image and observe the birefringence of the samples. The shear cast films were imaged at 0°, 45° orientation with respect to the flow direction and the polarizer.

2.2.7 Optical Property

A haze meter, Rhopoint ID-L A3100 – 001 was used to determine the transmittance, haze and clarity of the films. All data were taken with 8 mm spacer at room temperature and 50% relative humidity condition.

2.3 Results and Discussions

2.3.1 Effect of the addition of electrolytes on zeta potential

Aqueous colloidal dispersions of sulfated CNC maintain stability through repulsion arising from the overlapping electric double layers associated with their negative surface charges [18,31]. As for other colloidal entities, these surface charges of the CNC are screened by the addition of electrolytes [110,111]. The zeta potential of CNC aqueous dispersion with the addition of the transition concentration of each of the electrolytes is listed in **Table 2.3**. The zeta potential of electrolyte-added dispersions increased to -33.53, -31.77, and -26.03 with the addition of NaCl, CsCl, and $CaCl_2$, respectively. The addition of electrolyte neutralizes the anionic sulfate ester content, therefore increasing the zeta potential for all the electrolyte additions. The addition of NaOH to CNC dispersion increased the medium pH to ~12 and the zeta potential to -38.90, which is in line with previous literature [107,112]. Li et al. (2019) reported that the counter ionic (Na^+, OH^-) strength in CNC dispersion increases when pH goes above 11. Qi et al. [112] reported an increase in zeta potential when the pH of the dispersion changes, and at a higher pH, Na^+ shields the electrons, which may influence the zeta potential. However, an excess amount of OH^- at higher pH has been reported to result in both decreased crystallinity and a shift from cellulose I to cellulose II structure. [112]. This, in turn, affects the sensitivity towards ions and impacts the magnitude of the zeta potential.

Table 2.3 Average zeta potential for 1.66 wt% CNC aqueous suspension along with different types of electrolytes at average transition concentration

Sample	Avg. zeta potential, mV
Pure CNC	-52.03 ± 2.97
NaCl	-33.53 ± 2.90
CsCl	-31.77 ± 1.19
$CaCl_2$	-26.03 ± 0.23
NaOH	-38.90 ± 2.72

2.3.2 Effect of the addition of electrolytes on rheological characteristics

Cross-polarized optical microscopy images of the dispersions were taken with the slide oriented at 0° and 45° relative to the polarizer. The as received aqueous CNC gels exhibited birefringence and the watercolor like texture of bright colors expected for a liquid crystalline gel [72]. With the addition of electrolytes, the dispersions remained birefringent but had more uniform interference colors, shown in **Figure 2.1**

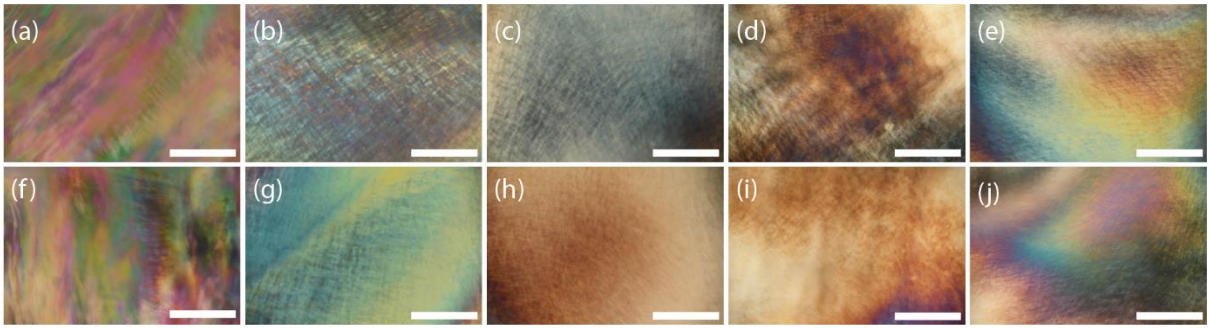

Figure 2.1 Cross polarized images of the dispersions at 0° and 45° with respect to the polarizer; ((a-e) dispersion images at 0°; (f-j) dispersion images at 45°); a and f refer to Pure CNC gel, b and g refer to NaCl added CNC gel, c and h refer to CsCl added CNC gel, d and i refer to $CaCl_2$ added CNC gel, e and j refer to NaOH added CNC gel; scale bar: 200 µm

The structural stability of the samples was measured through an oscillatory time sweep by applying a 1% strain to observe changes in the storage, or elastic, modulus (G′) over time. The storage modulus of the pure CNC gel was G′ = 600 Pa and remained constant throughout the test (**Figure 6.3 (Appendix A)**). The main purpose of conducting a time sweep was to identify the stability of the system. For pure CNC gel, G′ was found to be stable from the beginning; the time sweep was conducted for 20 min to confirm that G′ was stable. However, the addition of electrolytes resulted in G′ becoming dependent on time. For example, the addition of 0.48 mmol/g NaCl increased the initial G′ to ~800 Pa, which increased to ~1100 Pa over 2 hours (**Figure 2.2a**). The higher initial value of G′ resulted from the neutralization of the anionic surface charge of the CNC surface by

the addition of cations, thus compressing the cholesteric pitch due to the weakening of the electric double-layer repulsion. Similar time-dependent behavior was also reported by Lenfant et al. [109] and Danesh et al. [113] for CNC dispersions containing electrolytes. The addition of CsCl and $CaCl_2$ (**Figure 6.3 (Appendix A)**) to the CNC gel showed a similar behavior as NaCl.

Contrastingly, NaOH addition resulted in a significantly different time sweep curve, as depicted in **Fig. 2.2b**. The working mechanism with the addition of the neutral electrolyte was different than for the pH alteration. The initial value of G′ was only ~12 Pa but sharply increased to ~300 Pa during the first 20 minutes and then slowly increased to ~ 600 Pa during the remaining test time. The addition of NaOH to CNC gel also resulted in a more viscous-like system than NaCl, as shown in **Figure 6.4 (Appendix A)**. At increased pH, deprotonation takes place. At higher pH, counter ionic strength (Na^+, OH^-) of the CNC dispersion also increases, as reported by Li et al. [70] and Qi et al. [112]. Here, at pH~12, the amount of counterions in the system increases, which is more likely to cause an ionic envelope around the CNC particles and interrupt hydrogen bonding. This facilitated the formation of weaker gel, exhibiting higher dependency of G′ with shear or strain and atypical time sweep profile. Compared to NaOH, the other electrolyte addition exhibited higher initial G′ and slow structural reform.

The time dependency of G′ necessitates careful choice of rheological test protocols. The change in G′ was measured over time, and the sample was considered to be stabilized when the slope was minimized and G′ exhibited plateau formation. Approximately 2 hrs. were necessary for the stabilization of samples containing the transition concentration of electrolyte. Therefore, it is important to perform time sweeps before conducting frequency sweeps and steady shear flow curve experiments.

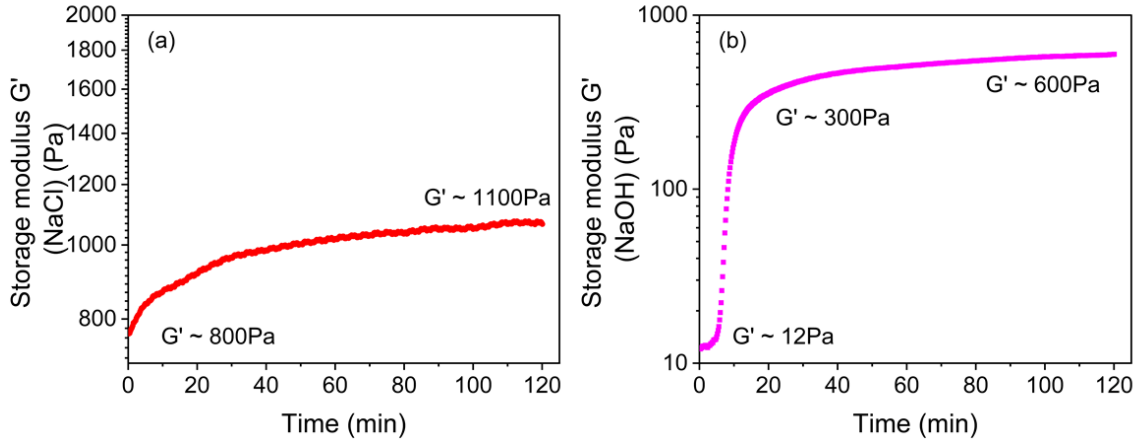

Figure 2.2 Oscillatory time sweep: (a) NaCl and (b) NaOH added CNC gel

As shown in **Figure 2.3**, all electrolytes added to CNC gel resulted in an increase in storage modulus compared to the pure CNC gel. The independence of G′ on frequency as well as the storage modulus being greater than loss modulus (all loss modulus shown in **Figure 6.3e (Appendix A)**) is consistent with a rheological gel. When compared based on the size, CsCl showed higher G′ than NaCl as Cs^+ has a higher affinity towards the anionic sulfate ester group [108]. This was further confirmed by the lower transition concentration range for CsCl than NaCl, noted in **Table 2.1**. The stronger cationic bridging strength of Cs^+ formed a stronger network structure than Na^+. Similarly, higher valency cations also exhibited higher affinity towards the anionic sulfate ester group, which resulted in a much lower transition concentration range for $CaCl_2$. The higher affinity of Ca^{2+} also created a stronger gel structure than Na^+ included in **Figure 2.3a.**

Again, the addition of NaOH exhibited behavioral disparity over the other electrolytes due to the change in pH of the system. Only a slight increase in G′ was observed compared to pure CNC gel, probably due to excess Na^+. As discussed previously, the higher concentration of counterions in

the system may create an ionic envelope around the particles that resist the formation of a strong gel structure even though an increase in zeta potential by NaOH addition was observed.

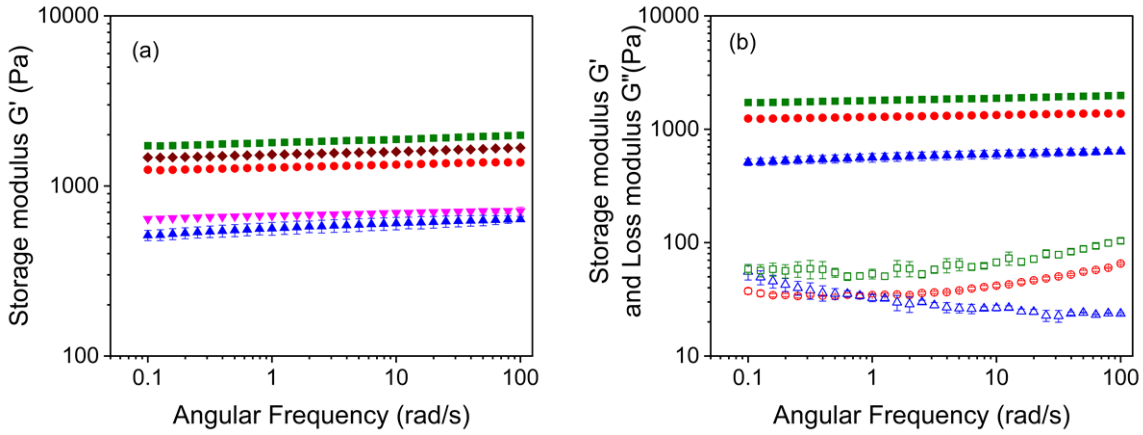

Figure 2.3 Frequency sweep measurements: (a) all G′ and (b) based on size, Color code: NaCl-red, CsCl-green,$CaCl_2$-brown and NaOH-magenta; Symbol code: all solid symbol – G′ and all empty symbol – G′′; (**Figure 6.3 (Appendix A)** for rest of the frequency plots)

The steady state shear viscosity profile, depicted in **Figure 2.4**, showed shear thinning behavior for all the samples. Previously, for pure CNC gel, a similar flow profile was also noticed and reported by other authors [72,77,81] . The shear viscosity data were fitted with a power law model, and the computed parameters are listed in **Table 4**. The addition of electrolytes significantly impacted the K (consistency index) and n (flow behavior index) data in comparison to the pure CNC gel. For the pure CNC gel, the flow index (n) was 0.071. However, when NaCl, CsCl, and $CaCl_2$ were introduced, the n ranged from 0 to 0.005, suggesting yielding behavior across the entire shear rate range. The flatness of the shear stress profile, also observed in **Figure 2.4**, further supported this yielding property for the electrolyte-added samples. Interestingly, the addition of

NaOH resulted in an n value of approximately 0.055, which is close to that of the pure CNC gel.

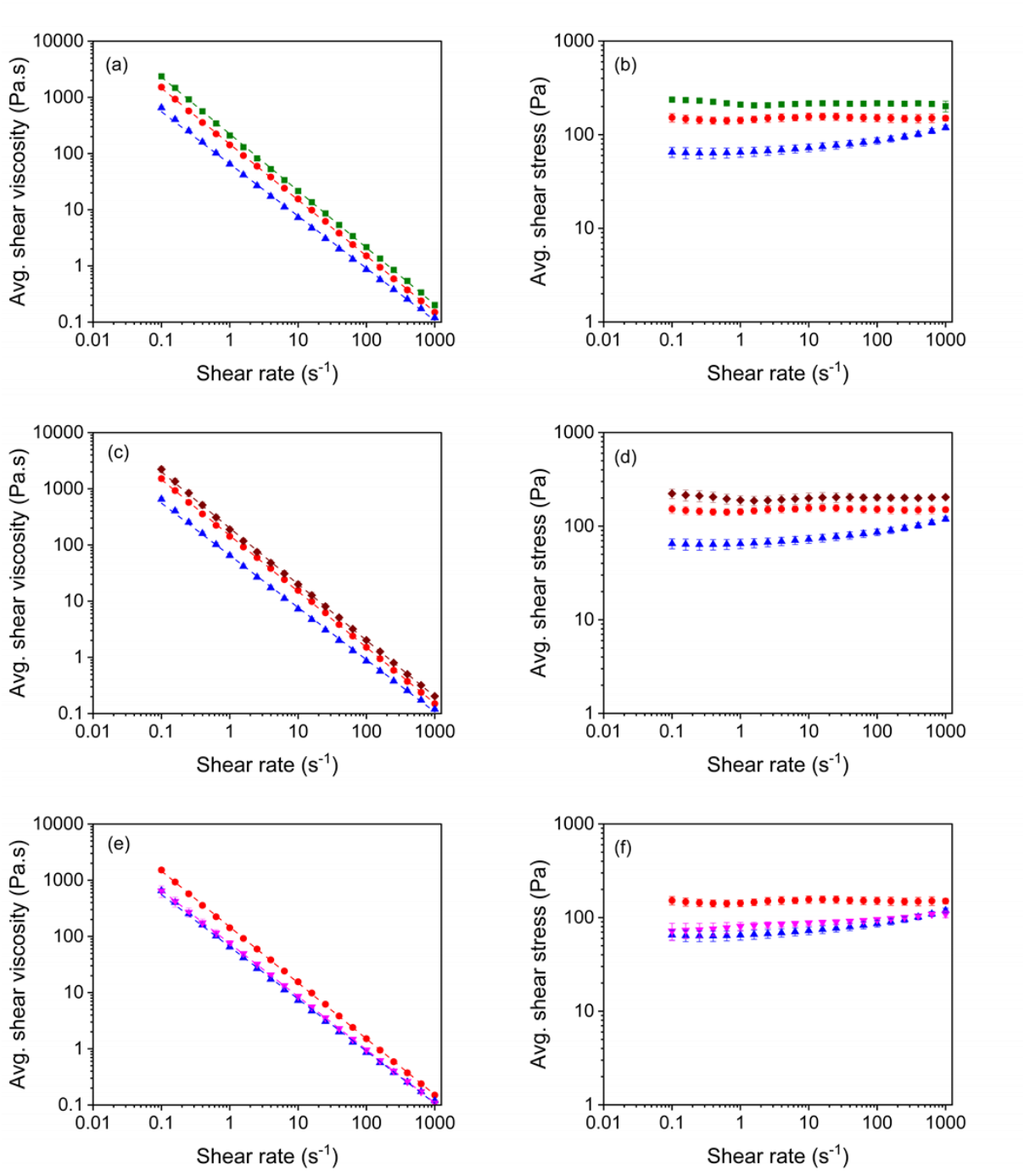

Figure 2.4 Shear viscosity and shear stress profile over (0.1 - 1000) s^{-1}: (a,b) size, (c,d) valency and (e,f) pH; Color code: Pure CNC gel – blue, NaCl-red, CsCl-green,$CaCl_2$-brown and NaOH-magenta; dotted lines are for Power law model fitting

Additionally, the consistency index did not exhibit a similar increase compared to the other electrolytes. This atypical behavior was most likely influenced by deprotonation as explained earlier. Consistent with the SAOS measurements, the addition of CsCl and $CaCl_2$ resulted in higher shear viscosity than NaCl. The alkaline CNC gel with the addition of NaOH exhibited similar properties as pure CNC gel with a slight increase in shear viscosity.

Table 2.4 Power law model; $\eta = K\dot{\gamma}^{n-1}$ fitting data for pure CNC and all electrolyte contained samples; η = shear viscosity, $\dot{\gamma}$ = shear rate

Sample	Power law constant, n	Flow consistency index, K (Pa.s^n)
Pure CNC Gel	0.071	65.51
NaCl	0.005	147.57
CsCl	-0.01 ~ 0	223.46
$CaCl_2$	0.001	200.23
NaOH	0.055	74.96

2.3.3 Combined effects of the addition of different electrolytes and mechanical shearing on the order parameter of CNC films

Comparison between Pure CNC and electrolyte addition

The self-assembled pure CNC film exhibited a very low order parameter, S ~ 0.13 ± 0.10, indicating the lack of global CNC alignment in the film. In comparison, the order parameter for shear-cast pure CNC films were 0.31 ± 0.02, 0.36 ± 0.15, 0.32 ± 0.12 for shear rate 20 s^{-1}, 40 $s^{-1,}$ and 100 $s^{-1,}$ respectively which showed improvement of the alignment by the application of mechanical shear. The found order parameter for pure CNC film can be correlated to the previous literature data. Previously order parameter, S ~ 0.29 and 0.5 for the shear rate 60 s^{-1} and 100 s^{-1}, respectively, for 11.8 wt% aqueous dispersion of CNC was reported by Chowdhury et al.[7]. Additionally, it was reported that to obtain high order parameter in the CNC film from 11.8 wt% aqueous dispersion, S ~ (0.88-0.91) around (400 – 500) s^{-1} of higher shear rate is required [7].

Generally, with a higher shear rate, the standard deviation also increases due to typical coating defects at high shear. Therefore, achieving better alignment at a lower shear rate would be ideal for practical application. In addition to this, pure CNC films also exhibit cracking above a critical cracking thickness [77] which is also another hindrance to practical uses.

The evaluated order parameter (S) for all the shear rates is listed in **Table 2.5.** The overall observation showed that the addition of electrolytes increased the average order parameter from 0.31 to 0.88. At the transition concentration, a higher concentration of cation intercalation between CNCs may take place, which weakens the chiral interaction, and facilitates unwinding the pitch to form a nematic-like structure. Generally, the addition of electrolytes at low concentrations causes shortening of cholesteric pitch due to higher chiral interaction as reported by Dong et al. [32], Hirai et al. [114], Araki et al. [95], and Parit et al. [107]. Additionally, Parit et al. [107] also reported an increased CNC cholesteric pitch at higher electrolyte concentrations. The transmittance profile of the films depicted in **Figure 6.5 (Appendix A)** exhibited the absence of the typical transmittance peak, confirming the formation of a nematic structure.

The gel structure of pure CNC offers a higher storage modulus than other CNC phases. Therefore, a single stroke of shear at a rate 100 s^{-1} is insufficient to completely break the network structure, create a nematic domain, and retain the alignment. The cross-polarized images of pure CNC film depicted in **Figure 2.5** showed a lack of uniform interference color in different areas, which can be correlated to the lack of uniform crystal alignment at 20 s^{-1} shear rate compared to the other film images. Additionally, the color contrast from 0° to 45° is not as significant as for the other films resulting in a lower order parameter. Initially, at lower NaCl concentrations, a weakened gel structure forms and produces a more viscous fluid-like substance (refer to **Figure 6.6 (Appendix A)**), which was also reported by Shafiei-Sabet et al. [81].

Table 2.5 Evaluated order parameter S for all samples

	Evaluated S for the following shear rate		
Sample	20 s^{-1}	40 s^{-1}	100 s^{-1}
Pure CNC	0.31 ± 0.02	0.36 ± 0.15	0.32 ± 0.12
NaCl	0.88 ± 0.01	0.82 ± 0.07	0.71 ± 0.08
CsCl	0.77 ± 0.13	0.86 ± 0.03	0.86 ± 0.02
$CaCl_2$	0.42 ± 0.10	0.79 ± 0.10	0.88 ± 0.02
NaOH	0.66 ± 0.11	0.71 ± 0.06	0.60 ± 0.07

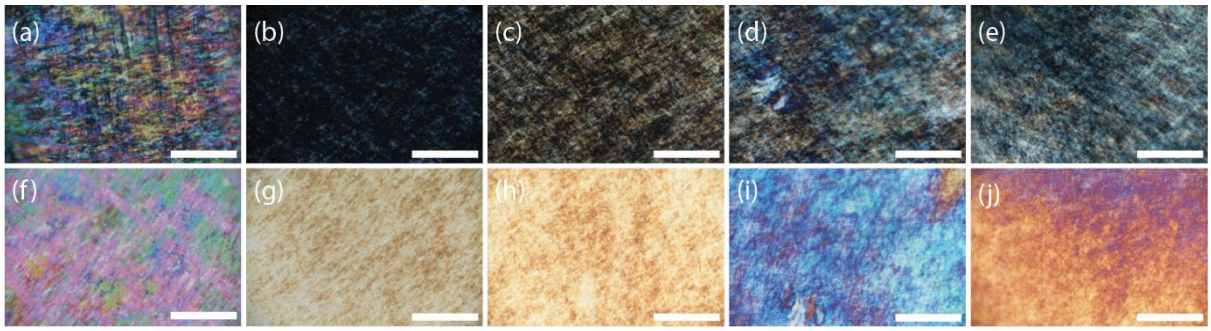

Figure 2.5 Cross-polarized images of pure CNC and electrolyte added films at 20s^{-1}shear rate: (a-e) – 0° and (f-j) – 45° with respect to the polarizer; a,f) - Pure CNC film, b,g) – Pure CNC + NaCl film, c,h) - Pure CNC + CsCl, d,i) – Pure CNC + $CaCl_2$ and e,j) - Pure CNC + NaOH film: scale – 200 µm; the resolution is 20x

At first, the hydrogen bonding in the gel structure is disturbed with a lower concentration of NaCl, inducing a more viscous property. With increasing concentration, structural reformation occurs and produces firmer gel. Since the nematic structure already contributes to the higher alignment, the order parameter for electrolyte addition increased significantly. Although the increment of the average order parameter was noticed for all the electrolytes, the shear requirement to achieve the same degree of alignment was different for every electrolyte.

Comparison based on size (NaCl and CsCl) and valency (NaCl and $CaCl_2$)

NaCl, CsCl, and $CaCl_2$ addition to CNC gel caused a much stronger network structure, which only yielded under high shear. These gel structures needed a specific shear force to stretch and spread

the material to cast the film rather than breaking the gel network structure since the nematic structure is already globally oriented. Depending on their G′ and shear viscosity, the shear rate requirement was fulfilled to obtain a similar S. In **Table 2.5**, the average order parameter was found to be around 0.88 for 20 s^{-1} for NaCl, and to obtain a similar order parameter, 40 s^{-1} of shear rate was needed for CsCl and $CaCl_2$ due to their higher G′ and shear viscosity than NaCl. In **Figure 2.6**, CsCl and $CaCl_2$ film images at 100 s^{-1} shear rates are included where more uniform interference color is observed compared to the 20 s^{-1} films. Having a gel consistency limited the relaxation of the structure and contributed to the higher order parameter. Additionally, the compatibility of the electrolytes to the substrate was also a factor that can contribute to variability in resultant order parameter.

Comparison based on pH (NaCl and NaOH)

NaOH addition to pure CNC gel also improved the overall order parameter; however, compared to NaCl, the improvement was much lower due to the increased pH of the gel. The time sweep results for NaOH exhibited a sharp increase in G′ for a shorter period. More likely, the ionic movement was the reason for this sharp rise, which also influenced the structure's misalignment during drying. CNCs structural relaxation after shearing with time was reported by Haywood et al. [77]. The addition of NaOH formed a weaker gel in comparison to the other electrolytes, thus structure relaxation can be higher than all other electrolytes as well.

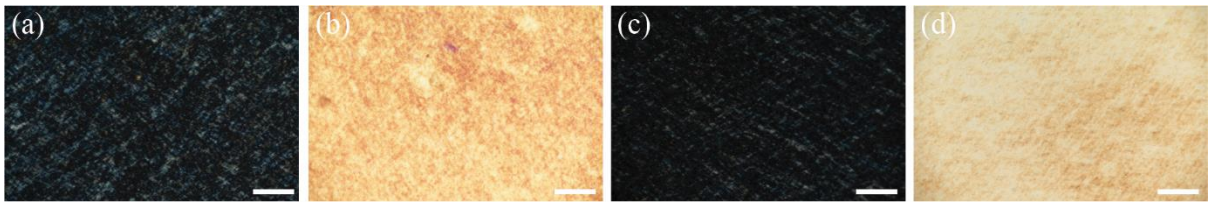

Figure 2.6 Cross polarized images of CsCl and $CaCl_2$ films at 100 s^{-1}shear rate: (a and c) – 0° and (b and d) – 45° with respect to the polarizer; a, b) - Pure CNC + CsCl, c, d) – Pure CNC + $CaCl_2$ film: scale – 100 µm; the resolution is 20x

Noticeably, the flexibility of the film was improved by electrolyte addition, and the shrinkage and brittleness of the pure CNC film were reduced, as shown qualitatively in **Figure 2.7**. This observation was also in line with Parit and Jiang (2023) [107]. The formation of cracks in CNC film was alleviated by adding electrolytes. The haziness of pure CNC film was also reduced with electrolyte addition due to the improved CNC alignment and reduced shrinkage, therefore reducing the light scattering. The haze and clarity of the films are shown in **Figure 2.7** and **Table 2.6,** demonstrating an improvement in both haze and clarity values. The strong hydrogen bond between the hydroxyl groups is a major reason for creating shrinkage in the film [103]. The addition of cations interrupted these hydrogen bonds and imparted flexibility into these films. This is evident from the evaluated thickness of the films shown in **Figure 2.7,** where a higher standard deviation is observed for pure CNC film due to the presence of shrinkage in the film.

Figure 2.7 (a,b) Pure CNC film cast at 20 s^{-1} shear rate (thickness: 35 µm) and (c,d,e) Pure CNC + NaCl films cast at 20 s^{-1} shear rate (thickness: 25 µm)

Table 2.6 Optical properties for pure CNC and Pure CNC + NaCl film at 20 s^{-1} shear rate

Sample	% Transmittance	% Haze	% Clarity
Pure CNC	88.17	17.43	80.48
Pure CNC + NaCl	88.40	7.67	96.02

2.4 Conclusion

This study demonstrated an easy method to obtain highly oriented CNC thin solid films from CNC aqueous gels by mechanical shearing at a low shear rate. By adding electrolytes to the CNC gel, a higher order parameter (0.88) can be obtained even at a low shear rate of 20 s^{-1}. Unwinding aqueous CNC's chiral nematic organization requires a high enough shear rate for the mechanical forces to overcome the chiral forces and unwind the pitch. In contrast, the addition of electrolytes at their transition concentration results in a nematic structure through surface charge neutralization. This global orientation further assists in developing highly oriented CNC films.

Overall, improvement in CNC alignment was observed for different shear rate regimes across all electrolytes, depending on their structural and flow behavior. The structural behavior is influenced by electrolyte valency, size, and pH, which directly correlate with cationic bridging strength and surface charge neutralization. NaCl can be considered the most suited among all the electrolytes used here as it exhibited higher ordering for lower shear and is a common electrolyte used widely. The improved flexibility and optical properties of the films make them suitable for applications such as piezoelectric materials, film packaging, and coatings.

Chapter 3 Impact of Sodium Hydroxide Treatment on Commercial Cellulose Nanocrystal: Investigating the Structure and Optical Property of Self-Assembled Film

3.1 Background

Cellulose nanocrystal (CNC) is a biomaterial produced from cellulose, which is abundantly available on Earth. Some common cellulose sources are plants, wood, cotton, tunicates, algae, and biomass [18,87–89,115]. CNC has gained popularity over the years due to its valuable applications and properties , such as its high Young's modulus ~ 150 GPa, improvement of mechanical and thermal properties in composites [116], unique structural color optical properties through which it can be used as an optical sensor [14,15,55,117], enhanced gas barrier properties [6,118] and piezoelectric properties [63,99]. Though the potential applications of CNC films are huge, the chiral nematic structure of self-assembled solid CNC film lowers the transparency and exhibits shrinkage and brittleness [119,120] which limits its industrial application especially in film packaging.

Commercially, CNC is produced through sulfuric acid hydrolysis which incorporates anionic sulfate ester groups, OSO_3^- which creating electrostatic repulsion between the CNC particles when suspended in water and stability in the suspension [20,25,26]. In the protonated condition, sulfated CNC showed auto catalytic desulfurization even at ambient conditions which promotes destabilization, therefore neutralization with sodium hydroxide (NaOH) is required for commercial production [92,121]. The surface charge of CNC along with its aspect ratio plays a crucial role in chiral nematic organization explained by SLO modified Onsager's theory [32,70]. Abitbol et al. [9] reported the correlation of the surface charge of CNC to its phase behavior and increased effective diameter for low surface charge. Therefore, partially removing these surface charges without significant modification of the aspect ratio could be an interesting pathway to alter

the chiral nematic structure. Many different routes were investigated to partially desulfate CNC such as heating the suspension, acid or alkali de-esterification or a solvolytic method [11,121,122]. So far, partial desulfation of CNC has been utilized to elucidate the effect of sulfate ester content on the suspension stability, rheology, composite properties, and reaction kinetics [9,11,121,123–125].

Sulfated CNC exhibits chiral nematic organization which is restored in the self-assembled film. These chiral nematic structures in CNC films decrease the transparency as they display fingerprint patterns and increase shrinkage and brittleness in the film through H-bond between OH- groups, which limits its application. Further, the addition of other hydrophilic polymers to CNC provides more uniform structural color [15,55]. Studies reported that electrolyte addition [8], increase in the pH of the suspension, and shearing the chiral can disintegrate the nematic structure [70]. Parit et al. [102] reported that transparent CNC self-assembled films can be produced via addition of NaOH and other electrolytes. Chowdhury et al. [7] observed that with mechanical shearing, the chiral nematic structure can be unwound to create nematic domains. In all the above studies, either the electrostatic double layer was neutralized through cation addition or applied higher external forces to stretch the chiral nematic structure. Therefore, it is evident that these sulfate ester groups in pristine CNC are one of the main hindrances to transparency.

In this work, NaOH treatment (as a partial desulfation reaction) was carried out on the commercial CNC to observe its effect on CNCs surface charge and investigate its effect on self-assembly in a solid film. Numerous studies have used the laboratory-prepared CNC which possesses a higher level of purity. Commercial grade CNC contains a certain impurity level, which can affect the post-reaction properties [126]. We obtained a complete transparent nematic film through the partial desulfation reaction and further investigated it systematically to demonstrate its optical properties.

CNC-based films are mostly reported to have high gas barrier properties. However, in the case of film packaging, especially where transparency is crucial, such as in the electronic industry, a detailed study on optical properties has not been previously evaluated. To the author's knowledge, investigating CNC orientation after NaOH treatment in solid self-assembled films and studying the optical properties of its composite was carried out for the first time.

3.2 Experimental Methods

3.2.1 Materials

Aqueous gel cellulose nanocrystal (CNC) with sodium counter ion was purchased from the University of Maine (Lot number 2021-FPL-CNC-170) with 11 wt% concentration. For partial desulfation, sodium hydroxide (NaOH) pellets were purchased from BTC Chemicals. Solid, low molecular weight hydrolyzed polyvinyl alcohol (PVA), n = 1750 ± 50 was purchased from TCI Chemicals. All the chemicals purchased were of high purity and analytical grade. The samples were prepared by partial desulfation and compared with pure/neat CNC film based on their structure and physical and optical properties.

3.2.2 Sample Preparation

An alkaline medium partial desulfation process was chosen to conduct the reaction. The sodium form of CNC is found to be stable against acidic conditions, thus alkaline conditions are the most suitable ones. The experiment is conducted in a water bath at 65 $^{\circ}$C for 1 hr. and 4 hrs. of reaction time. Isotropic CNC suspension with 1.66 wt% is prepared and 1 M NaOH is added. The reaction quenched by addition of cold deionized (DI) water at 4 $^{\circ}$C and 1 ml of 4 M NaCl is added as a coagulation aid which further improves the purification efficiency with a centrifuge.

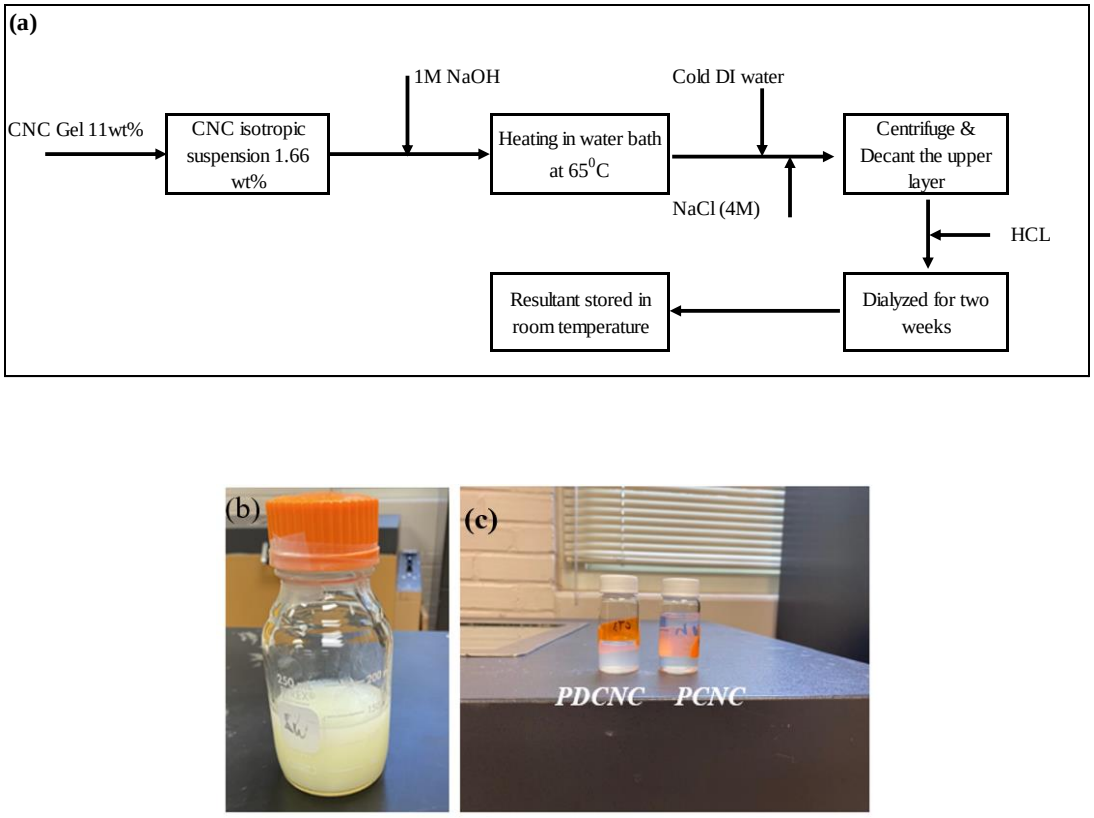

Figure 3.1 (a) Process schematic for partial desulfation; (b) Slight yellow color post reaction; (c) Pure CNC (PCNC) and Partially desulfated CNC (PDCNC 4) at 0.84 wt%

The centrifugation was performed three times with DI water. Next, the pH was adjusted to neutral and dialyzed with a regenerated cellulose membrane of (12-14) kDa MWCO for two weeks until the conductivity of the medium showed no fluctuation. The obtained CNC suspension exhibited a slightly acidic pH of ~ 4.66. The sample was neutralized and stored at room temperature.

3.2.3 Film Formation

The self-assembled films of pure CNC (PCNC), partial desulfated CNC (PDCNC) were prepared from isotropic suspension, ~ 1 wt%. To maintain the CNC content, 0.4 g CNC was cast on polystyrene petri dish and allowed to dry in the ambient temperature for 2-3 days. After this, the films were peeled off from the substrate and stored at 50% RH. Similarly, to prepare CNC and

polyvinyl alcohol composite films, (10-30) wt% PVA was added to the PCNC and PDCNC 4 and the suspension was magnetically stirred for 2 hours. To prepare composite film, 0.4g CNC was used as the basis.

3.2.4 Zeta Potential and Particle Size Analysis

A Zeta sizer Nano ZS, Malvern instrument was used to determine the zeta potential and hydrodynamic particle size of the samples. For all of the samples, 0.84 wt% concentration was maintained, and pH was kept neutral. Three measurements were taken to calculate the average and standard deviation.

3.2.5 Sulfur Content Analysis (CHNS/O)

A Vario MICRO cube, Elementar (New York, NY, USA) was used to determine the sulfur content in all the samples, PCNC, PDCNC 1 (1 hour reaction) and PDCNC 4 (4-hour reaction). For sulfur content analysis, 5 mg freeze-dried samples were used. The suspensions were frozen overnight and freeze-dried for 3 days. Three measurements were used to determine the average sulfur content with standard deviation.

3.2.6 UV-Vis Spectroscopy

A Thermo Scientific Genesys 10S UV−Vis spectrometer was used to detect the transmittance profile of the solid film samples for the wavelength range of 200−800 nm. Three different samples were cut from the self-assembled film to provide the transmittance spectra of the samples.

3.2.7 Scanning Electron Microscopy (SEM)

A field emission scanning microscope, JEOL JSM-7000F is used to capture the cross-sectional images of the samples. The samples were first dipped into the liquid nitrogen and then fractured. Further, the samples were sputter gold coated before imaging. The images were taken with 10 kV accelerating voltage and the scale bar was used 1µm and 100 nm.

3.2.8 Cross Polarized Microscopy

A Nikon (Melville, NY) Eclipse Ni microscope with a Nikon DS-RI2 camera and 20×/0.45 LU Plan Fluor was used to determine the cross polarized images of the films at 0° and 45° to observe the color contrast and intensity difference.

3.2.9 Transmittance, Haze, Clarity and Sharpness Analysis

Rhopoint ID-L A3100-001 was used to compute the haze, transmittance, clarity, and sharpness of the samples at 50% RH. An 8 mm distance spacer was used for the entire study. Solid self-assembled films were used for this analysis. Three measurements were taken to provide the average data with standard deviation.

3.2.10 Tensile Strength

An Instron, Model No. 5982, Norwood, MA was used to perform tensile tests of the films. Crosshead speed used to perform the test was 1.5 mm/min at room temperature and 50% RH. Three specimens were cut from the films to calculate average values with standard deviation.

3.2.11 Thermal Analysis (TGA)

A TGA Q500, TA instrument was used to perform Thermogravimetric analysis of freeze-dried samples under nitrogen with a rate of 10°C/min from room temperature to 800°C. To remove any residual moisture, an isothermal step was performed at 120°C for 20 minutes.

3.2.12 X-Ray Diffraction (XRD)

A Bruker diffractometer with 40 mA current and 40 kV accelerating voltage was used to conduct XRD analysis of the samples at room temperature. The scanning was performed with the rate 5°/min for the 2θ range $10^{\circ} - 40^{\circ}$. The crystallinity calculation is performed by using the following

equation: $\%CRI = \left(\frac{Ac}{A_c+A_a}\right) * 100$ where A_c represent area of the crystalline peak and A_a represents area of the amorphous phase.

3.2.13 FTIR

A Nicolet 6700 FTIR spectrometer, Thermo Scientific was used to measure the transmission spectra of pure and NaOH treated CNC for 600-4000 cm^{-1} frequency range. 64 cumulative scans were performed to determine the spectra and the resolution used was 4 cm^{-1}.

3.2.14 Film Thickness

Testing Machine Inc. Model 49-71, ranging 0 - 1.25 mm is used to determine the thickness of the samples indicated in **Table 3.1**. Three measurements were taken to calculate the average thickness with standard deviation.

Table 3.1 The average thickness of all the films

Sample	Average Film Thickness (µm)
Pure CNC (PCNC)	55.25 ± 14.45
PDCNC 1	82.00 ± 5.29
PDCNC 4	72.67 ± 7.77

3.3 Results and Discussion

3.3.1 Zeta Potential, Hydrodynamic Size and Sulfur Content Analysis

Sulfated CNC exhibits stability in dispersion through the repulsion due to the overlapping of the electric double layer. The anionic surface charge plays a crucial role in dispersing CNC in aqueous medium [20,87]. The sulfur content analysis shown in **Table 3.2** showed a decrease of ~ 16% for 4 hrs. of the NaOH treatment or partial desulfation reaction. For the 1-hour reaction, no significant decrease in sulfur content was observed through elemental analysis (CHNS/O). The PDCNC 1 and PDCNC 4 remained well dispersed in aqueous medium at ~ 1 wt% concentration. Interestingly, a

contrasting result was observed through zeta potential determination where more negative results were obtained than pure CNC, i.e., -57.93 mV for PDCNC 1 and -64.00 mV for PDCNC 4. Commercial CNC can possess organic impurities / hemicellulose, which can degrade into small molecules or charges during the reaction and have a direct effect on zeta potential if not removed entirely. Banerjee et al. [126] showed that the zeta potential varies greatly when commercial CNC is purified with different solvents. Further, Reid et al. [127] also observed no change in zeta potential post partial desulfation reaction. Most likely, the CNC used contained impurities or hemicellulose, which degraded into small anionic charges during the NaOH treatment and could not be removed entirely during multiple centrifugation and dialysis steps. These charges, retained in the CNC surroundings directly impacted the zeta potential causing it to decrease. The TGA analysis, depicted in **Figure 3.2a**, showed the two peaks for CNC, ~ 256 ^{o}C and 296 ^{o}C, whereas for PDCNC 1 and PDCNC 4, only the peak around 296 ^{o}C was retained. A similar observation was reported by Imiete et al. [123] where the author related this to the hydrolysis of sulfate half ester group. Further, Kumar et al. [128] reported similar three step degradation of CNC and associated the lower degradation temperature, around (220 - 270) ^{o}C with CNC's sulfate ester group on surface. Overall, the peak observed around (100 - 120) ^{o}C in the **Figure 3.2a** was due to the moisture removal from the sample.

The hydrodynamic particle size increased from 133.13 nm (PCNC) to 248.07 nm (PDCNC 1) and 251.50 nm (PDCNC 4). Removal of surface charge weakens the electrostatic repulsion which promotes CNCs to coalesce, thus increasing hydrodynamic particle size with overlapping the CNC double layer. Again, the presence of more anionic charges on CNC surrounding can create more electrostatic repulsion between the particles causing increased space between the CNCs which in

effect increases the effective diameter. Here, the latter was the more prominent mechanism to take place as shown by the more negative zeta potential.

Table 3.2 Sulfur content, zeta potential and hydrodynamic particle size

Sample	%S for CHNO/S	Zeta Potential (mV)	Apparent particle Size (nm)	ΔS
PCNC	0.89 ± 0.02	-49.77 ± 0.58	133.13 ± 2.61	--
PDCNC 1	0.88 ± 0.01	-57.93 ± 1.36	248.07 ± 1.06	Insignificant
PDCNC 4	0.73 ± 0.03	-64.00 ± 0.10	251.50 ± 0.79	16.09%

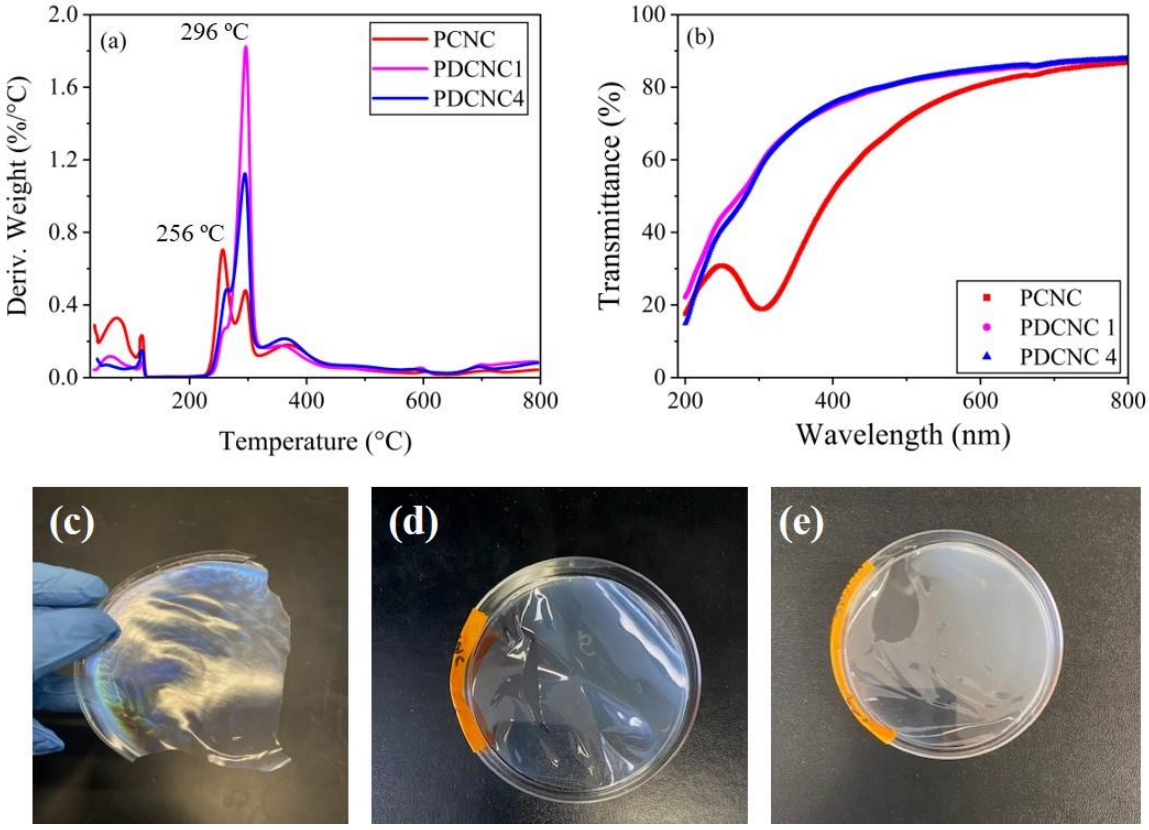

Figure 3.2 (a) TGA analysis (b) Transmittance profile for Pure CNC, PDCNC1 and PDCNC4 films; Self-assembled images of (c) PCNC, (d) PDCNC 1 and (e) PDCNC 4 film

3.3.2 Morphology and Material Properties

The self-assembled solid PCNC (Pure CNC) and PDCNC 4 films are depicted in Figure **3.2**. A completely transparent film was formed post reaction. UV-Vis spectroscopy was also performed to obtain the transmittance profile before and after the reaction, shown in **Figure 3.2b**. Typically, the chiral nematic structure results in a minimum peak in the transmittance profile which was completely absent for PDCNC 1 and PDCNC 4, confirming the absence of the chiral nematic organization. The major criteria for the formation of the chiral nematic structure in CNC is its anionic sulfate ester group coupled with the aspect ratio explained by Stroobants, Lekkerkerker, and Odijk (SLO) modified Onsager theory [10,32]. The twist action between the particles is formed due to the repulsive force. Therefore, altering the electrostatic repulsive force either by surface charge removal or introducing higher anionic charges in the system can significantly affect the chiral nematic organization. An interesting work by Abitbol et al. [9] reported the correlation of CNC's effective diameter with various surface charges of CNC and noticed the effective diameter increased for decreasing surface charge. Generally, the partial desulfation reaction selectively removes the surface groups of CNC and replaces them with hydroxyl groups. The partial removal of surface charge increased the hydrodynamic size due to the weakening of the repulsive force. Again, in this case, possibly the presence of small anionic charges in the system observed from zeta potential, generated from the impurities could also take part in influencing the repulsive force. The effect of ionic strength through pH modulation of the CNC dispersion also affects the effective diameter and create nematic domain observed and explained by Li et al. [70]

In the SEM images, typical fingerprint-like structures were observed for PCNC depicted in **Figure 3.3a and Figure 3.3d**. However, the complete absence of fingerprint structure and oriented dense structure was observed for both PDCNC 1 and PDCNC 4 indicating the formation of nematic

structure shown in **Figure 3.3b and Figure 3.3c**. Further, distinctive color change and intensity contrast from 0º to 45º shown in cross polarized images confirm the formation of the nematic domain, depicted in **Figure 7.1 (Appendix B)**.

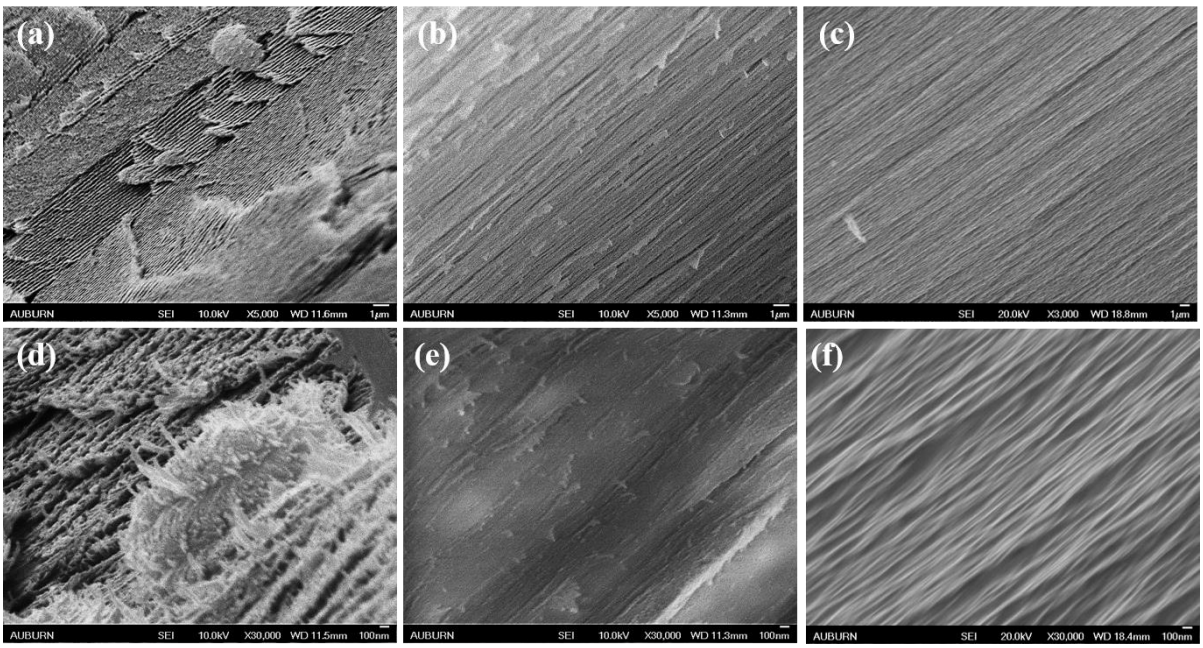

Figure 3.3 Cross sectional SEM images of the films; (a) PCNC, scale: 1 µm; (b) PDCNC 1, scale: 1 µm; (c) PDCNC 4, scale: 1 µm; (d) PCNC, scale: 100 nm; (e) PDCNC 1, scale: 100 nm & (f) PDCNC 4, scale: 100 nm

The self-assembled films were characterized by X-ray diffraction to determine the get a complete crystallinity after the reaction. In general cellulose I which is abundant in the nature shows 2θ peak at 15.1°, 16.9° and 22.9° for the reflection plane (1-10), (110) and (200) [8]. The XRD profile shown in **Figure 3.4a** indicated that the cellulose structure was not modified during the reaction as the peaks obtained were found to be the same for PCNC, PDCNC1 and PDCNC4. However, for PDCNC 1 and PDCNC 4, the intensity at 22.9° dropped and at 15.1° and 16.9° intensity increased. Possibly, NaOH treatment at elevated temperature affected the crystallite size which most likely facilitate formation of co-crystallization, thus affected the diffraction peak intensity [129]. The crystallinity index was calculated and listed in the **Table 3.3**. We observed a slight drop in

crystallinity for PDCNC 1 (85.94 ± 3.29) % and PDCNC 4 (86.82 ± 3.20) % from PCNC (88.73 ± 1.97) %. Initially, the degradation of organic impurities occurred during the reaction, thus not much change in the crystallinity was observed as the cellulosic component degradation was limited. Navarro et al. [125] observed increased in crystallinity after partial desulfation through acid hydrolysis. Other literature reported decreases in peak intensity and crystallinity post partial desulfation [122,123]. Most probably, the variability in the reported literature arises from multiple factors like CNC source, counterion type, reaction medium and its concentration. Tensile strength tests were performed on PCNC and PDCNC 4 which showed similar stress-strain profiles, shown in **Figure 3.4b**, as well as tensile strength i.e., ~ 61 MPa and 62 MPa respectively (**Table 3.3**). The crystallinity of the material was not greatly compromised; therefore, tensile property of the film was not affected.

Literature studies reported that the sulfate ester content in CNC characterized through the FTIR shows vibration in range of 1200-1300 cm^{-1}, 1020-1200 cm^{-1} for asymmetric and 950-1000 cm^{-1} for symmetric stretching [130]. FTIR analysis of PCNC, PDCNC 1 and PDCNC 4 depicted in **Figure 3.4c** showed peaks at 1108 cm^{-1} and 1160 cm^{-1} correspond to the –S-O stretching. A slight drop in peak length/intensity observed for PDCNC 4 compared to PCNC, qualitatively confirmed the successful removal of sulfate ester groups from CNC surface. TGA analysis showed thermal degradation temperature at 5 wt% loss for PDCNC 1 and PDCNC 4 increased from PCNC. The increase in the degradation temperature from ~ 247 ^{o}C to 259 ^{o}C is mostly influenced by degradation of the sulfate half ester content through NaOH hydrolysis.

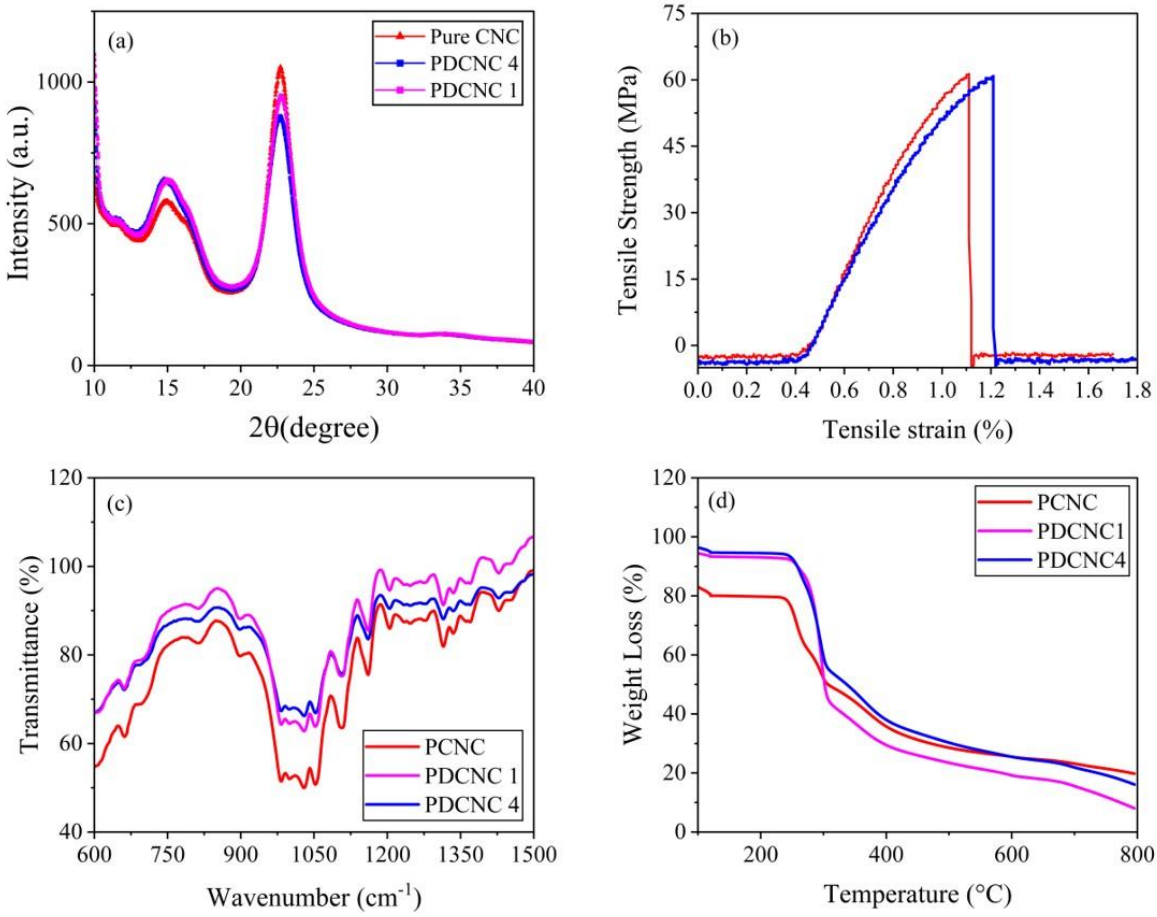

Figure 3.4 Effect of partial desulfation on film properties (a) XRD (b) Tensile strength (red – PCNC; blue – PDCNC 4) and (c) FTIR (d) TGA

Table 3.3 Crystallinity index (CRI), tensile strength and thermal degradation temperature

Sample	% CRI	Tensile Strength (MPa)	Avg. $T_{degradation}$ (5% wt. loss) (^{o}C)
PCNC	88.73 ± 1.97	61.11 ± 10.34	247.71
PDCNC 1	85.94 ± 3.29	--	259.25
PDCNC 4	86.82 ± 3.20	62.66 ± 9.05	259.16

3.3.3 Optical Properties of the Film

A qualitative haze and transparency analysis was carried out and shown in **Figure 3.5**. The view with and without film showed similar transparency through the naked eye, indicating an overall

improvement in optical property has been achieved. Further, an explicit quantitative analysis was performed to observe the effect of NaOH treatment on the optical properties of the self-assembled film, depicted in **Figure 3.6** and indicated in **Table 7.1 (Appendix B)**.

Without film With PDCNC 4 film

Figure 3.5 Qualitative analysis of transparency: imaging through PDCNC4 film

Both PDCNC 1 and PDCNC 4 films showed better optical qualities than PCNC in terms of transmittance, haze, clarity, and sharpness. The transmittance increased from ~ 82% to 88% which indicated that higher amounts of visible light pass through the film. The films also exhibited reduced the light scattering at 2.5° or higher which lowers the haze from ~7% to 3%. This haze value can be correlated to standard transparent plastic materials. A neat polypropylene (PP) substrate possesses high optical quality such as 94.04% transmittance, 2.60% haze and 98.5% clarity evaluated and reported by Nuruddin et al. [51]. Compared to this neat PP substrate, a very close transmittance and haze percentage was obtained. Additionally, the clarity (scattered light below 2.5°) of these films reached ~ 99% which is close to the PP standard as well. An additional property, sharpness, was also evaluated, which can be correlated to the fine tuning and correlated to clarity, thus an important property for electronic application. With low sharpness, the detail of an image is lowered. Thus, the low sharpness also limits the detail or acuteness of the view through

the film. PCNC films exhibit chiral nematic structure which causes optical rotation of the light, thus reducing the sharpness to ~ 59%. NaOH treatment caused the formation of a nematic structure which increased the sharpness to ~ 96%. Overall, all four optical parameters were found to be improved after the structural modification.

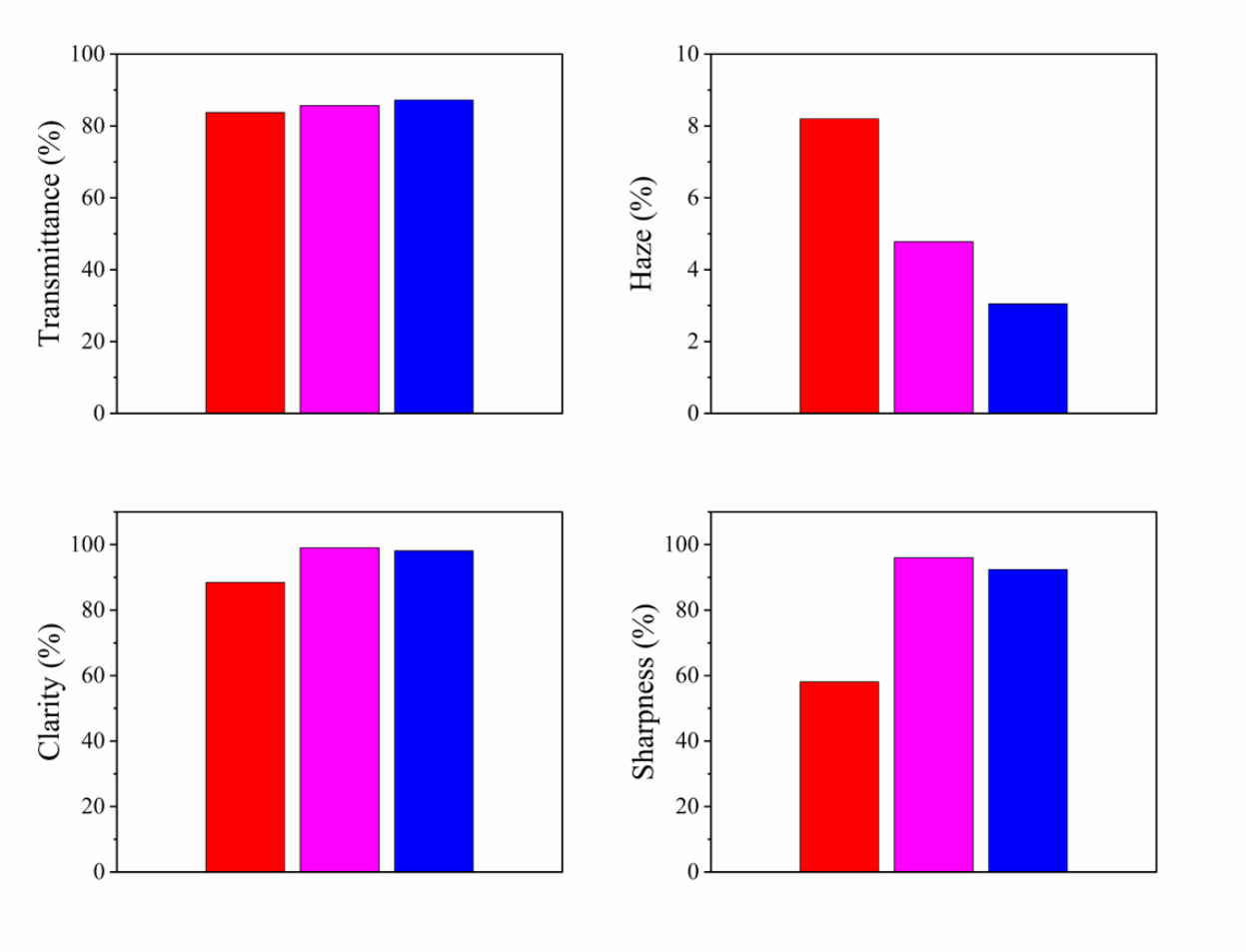

Figure 3.6 Optical properties of Pure CNC, PDCNC1 and PDCNC 4; Color code: Pure CNC - red; PDCNC1 - magenta and PDCNC4 – blue (Refer **Table 7.1 (Appendix B)** for the dataset with standard deviation)

3.3.4 Effect of PVA on optical properties

CNC-PVA composite films were prepared to observe the effect of the polymer on the film preparation and evaluate the optical properties. A comparative study was developed between

PCNC-PVA and PDCNC 4-PVA composite. At a 30% PVA concentration, the PDCNC 4 exhibited sedimentation and crack formation during evaporation of the film depicted in **Figure 7.2 (Appendix B)**. Therefore, the PVA concentration was maintained below 30% for the detailed study.

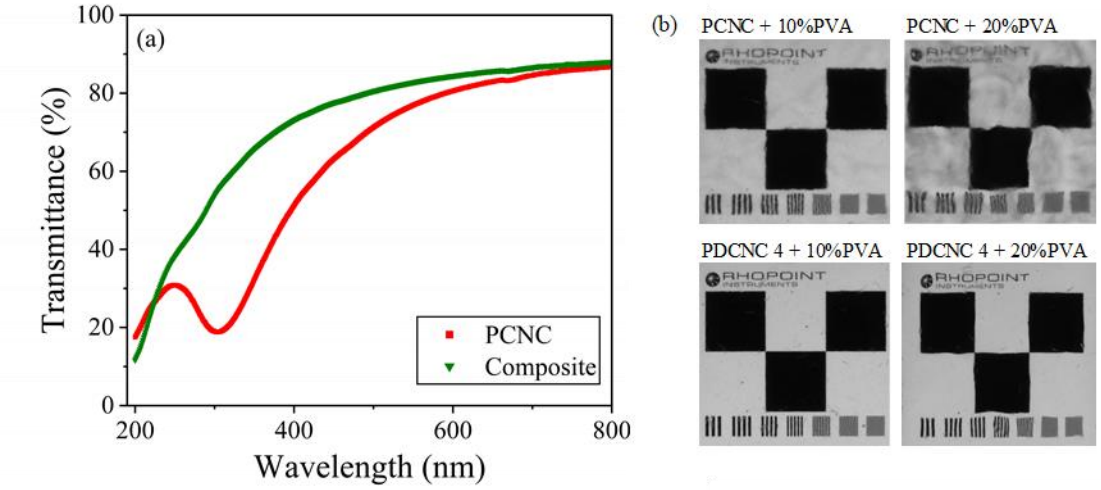

Figure 3.7 (a) Transmittance profile for Pure CNC and PDCNC 4+20%PVA composite film; Color code: Pure CNC – red, Composite – green; (b) Qualitative analysis of the optical properties of the film with addition of PVA (films prepared with constant basis of CNC: 0.4 g)

The complete absence of a transmittance peak, a characteristic property of chiral nematic structure of CNC, was observed even for addition of 20 wt% PVA indicating successful preparation of a transparent green composite film, shown in **Figure 3.7a**. The self-assembled PDCNC 4 film with 20% PVA is included in **Figure 7.2 (Appendix B)** where transparency was visually observed.

The addition of PVA to PCNC caused deterioration in the optical properties with increase in PVA concentration. At 20% PVA concentration, transmittance dropped to 78.33% with increased haze above 10.55%. Further the sharpness dropped below 30% with increased waviness of the film

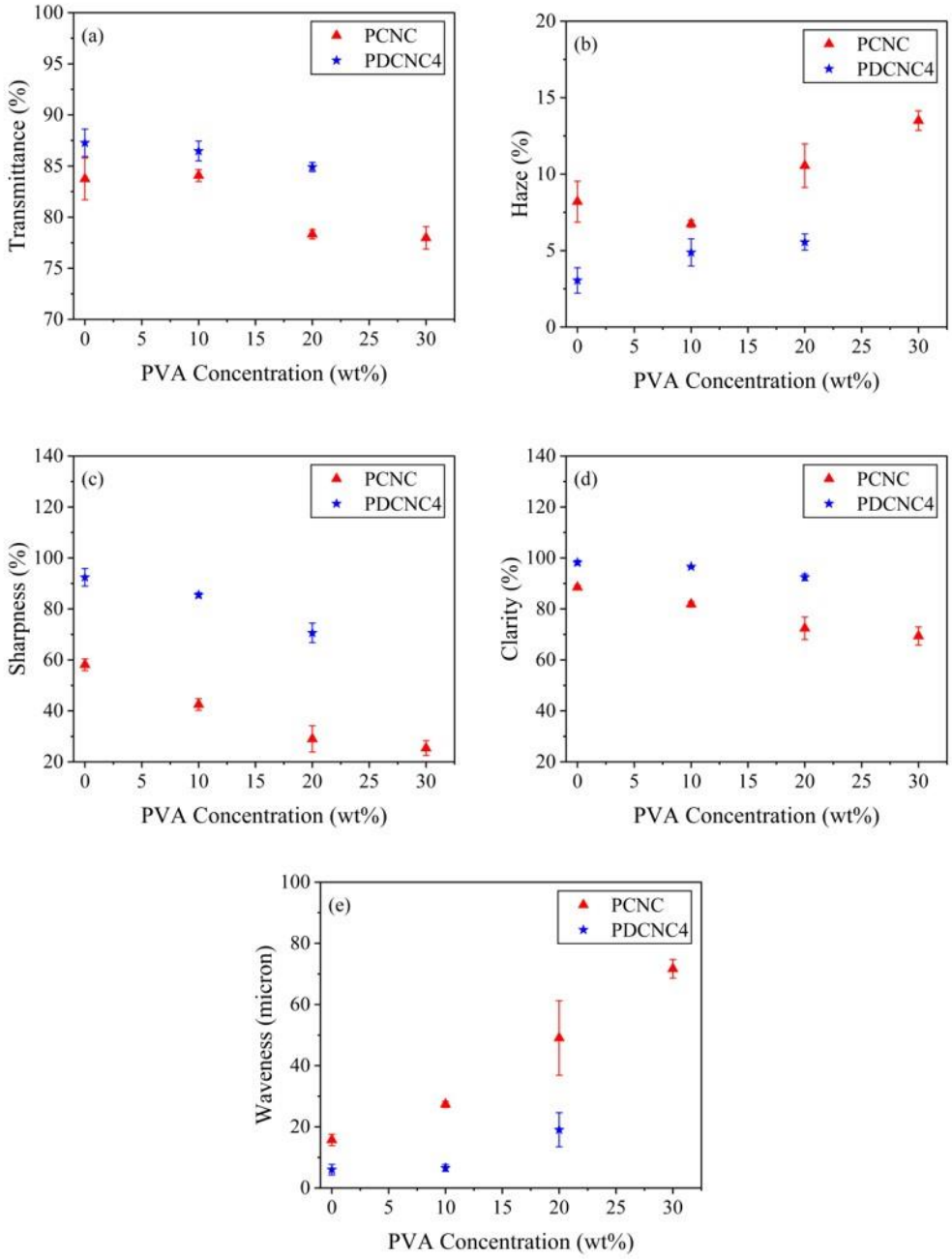

Figure 3.8 Effect of PVA concentration on the optical properties of PCNC and PDCNC 4 film

indicated in **Figure 3.8** and **Table 7.2 (Appendix B)**. Compared to this, PDCNC 4 exhibited sharpness at around 70% for 20% PVA addition. An image was captured and included in **Figure 3.7b** to explain the effect of sharpness on the image. With reduced sharpness, the edges between

the black and white checked boxes became blurry however, at higher sharpness the same box image exhibited high edge transitions. Although addition of PVA to PDCNC 4 also exhibited a decreasing profile, significant properties were not comprised in this case. For all the parameters PDCNC 4 exhibited much superior qualities than PCNC.

3.4 Conclusion

A simple NaOH hydrolysis was carried out to observe the effect of the reaction on the chiral nematic structure of solid self-assembled film. A complete transparent, nematic CNC film was formed after the reaction due to the increased hydrodynamic particle size which most likely created hindrance in twisting action. This was due to the increased anionic charges in the system due to degradation of organic impurities. The chiral nematic structure reduces the transparency of the material thus limiting its application in film packaging. In this research, a complete comparative analysis of the optical properties was completed and presented. Post NaOH treatment, CNC exhibited low haze and high clarity and sharpness. A CNC-PVA composite was prepared further to impart strength and flexibility in the film. Addition of PVA to the NaOH treated CNC exhibited improved optical quality when compared to the pure CNC film. The chiral nematic structure was not restored; thus, the resultant film showed no structural color. Further, cellulose being an insulating material, this CNC material could be a promising candidate for electronic packaging or in coating applications.

Chapter 4 Preparation and Characterization of Transparent Cellulose Nanocrystal Film Using Freeze-Thaw Technique

4.1 Background

Cellulose nanocrystal (CNC) is a renewable biomaterial produced by sulfuric acid hydrolysis of cellulose and exhibits unique optical properties due to its chiral nematic organization [131,132]. Sulfuric acid hydrolysis produces rod-shaped CNC particles with anionic sulfate ester groups, which influences the formation of chiral nematic structure [18,73,133,134]. In chiral nematic organization or cholesteric phase, a slight twist in nematic structure along the axis is formed, which resembles a helical organization. Being a lyotropic liquid crystal, CNC exhibits distinctive phase behavior in solvents (isotropic, biphasic, liquid crystalline, and gel) that can be predicted via Stroobants-Lekkerkerker-Odjik (SLO) modified Onsager's theory [10,32,68,69,135]. The different phase behavior of CNC depends on its aspect ratio (L/D), surface charge and correlates with the system's rotational and translational entropy. With increasing CNC concentration in the suspension, a chiral nematic structure forms, attributed to the loss in rotational entropy and gain in the translational entropy [10,32,69].

Transparency is an important parameter to achieve when considering applications in the coating and packaging industry as it impacts sales and marketing through visual stimulation [5]. The cholesteric structure is restored in self-assembled CNC films and gives rise to the structural color or iridescence that is mainly utilized in optical sensor applications [14,15,55]. However, this structural organization of CNC decreases the transparency of the self-assembled film, limiting its application where transparency is important. To date, transparent CNC film is achieved by disintegrating the chiral nematic structure either through physical (mechanical, magnetic, or electric field shearing [136]) or a chemical (doping with different electrolytes, modulating pH)

approach. Through mechanical shearing, a unidirectional CNC orientation can be obtained, thus, transparency can be achieved [7,51,86]. By the addition of electrolytes like sodium chloride (NaCl), calcium chloride ($CaCl_2$), and sodium hydroxide (NaOH), the chiral nematic structure can be disintegrated into the nematic structure as it screens the CNCs surface charge [102,107]. Therefore, for the preparation of a transparent self-assembled CNC film, chemical doping is essential.

In this research we aimed to develop a simple method to produce transparent self-assembled CNC film without chemical modification. Freeze-thaw is an easy technique which is mainly used to produce CNC-based hydrogels for biomedical or robotic applications [137–139]. Previously, freeze casting through a sublimation process was used to prepare unidirectional aerogels [140]. Lewis et al. [141] observed the gelation of CNC dispersions by the freeze-thaw method and reported aerogel formation by physical aggregation of the ice crystal structure. However, the investigation of CNC film formation and its properties resulting from the freeze-thaw method has not been investigated so far to the best of our knowledge. Here, we prepared transparent CNC films using the freeze-thaw method and presented a systematic study on their structural and optical properties through SEM, XRD, transmittance profile and transmittance, haze, sharpness, and clarity analysis. The arrangement of CNC in the dried film depends on the history of the dispersion as well as its properties [28]. In this process, the CNCs undergo a kinetic arrest state during freezing, which cannot be reversed during thawing. Therefore, a chiral nematic structure cannot be formed. To the best of our knowledge, this is the first time that CNC film was prepared through the freeze-thaw technique with detailed structure-property analysis.

4.2 Materials and Method

4.2.1 Sample Preparation

We utilized the sodium form of an aqueous dispersion of CNC in the concentration of 11 wt% with 1.1% sulfur from the University of Maine (Lot number 2021-FPL-CNC-170) and diluted the CNC aqueous gel with deionized water to a concentration of ~ 2 wt% to obtain isotropic behavior. The zeta potential obtained for a 0.84 wt% CNC suspension was -49.77 ± 0.58. We define this CNC suspension as Pure CNC or PCNC. We prepared the self-assembled solid CNC film by pouring the isotropic CNC suspension into a polystyrene petri dish and allowing the evaporation to occur under ambient conditions, which takes around three days for complete drying. Similarly, films prepared by the freeze-thaw method from the same ~ 2 wt% CNC isotropic suspension were frozen overnight in a -20°C freezer. The frozen suspension was then kept at room temperature around 2 hours to thaw. For freeze-thaw cycle 1 (FT1), the thawed suspension was then dried under ambient conditions for solid film preparation. For a higher number of cycles (FT2), the thawed suspension was frozen overnight, thawed, and dried. All films were prepared with 0.4 g CNC as a basis.

4.2.2 Characterization

A field emission scanning electron microscope, JEOL JSM-7000F with accelerating voltage 20 kV was used to capture the cross-sectional image of PCNC and FT1 sample. All the samples were first exposed to liquid nitrogen for a few seconds and then fractured. The samples were gold sputter-coated before taking the images. Cross-polarized microscopy was performed with a Nikon (Melville, NY) Eclipse Ni microscope with a Nikon DS-RI2 camera at 0º and 45º to detect the intensity changes when the specimen was rotated with respect to the polarizer.

XRD analysis was performed with a Bruker diffractometer. The accelerating voltage and current used were 40 kV and 40 mA, respectively, with a scanning rate of 5° min^{-1}. The 2θ range was used

(10 – 40) °. A Thermo Scientific Genesys 10S UV−Vis spectrometer was used to detect the transmittance profile for the range of (200 – 800) nm. Three measurements were taken to compute an average transmittance profile for all the samples. Rhopoint ID-L A3100-001, a haze meter, was used to perform a quantitative analysis of the optical properties of the samples to determine transmittance, haze, clarity and sharpness. Rhopoint ID-L uses an image-based system to quantify the degree of transparency [142]. Three measurements were taken from different spots in a film to compute an average value and standard deviation. All the measurements were taken with an 8 mm spacer at room temperature and 50% RH. A thickness tester, Testing Machine Inc. Model 49-71, ranging 0 - 1.25 mm was utilized to compute the sample thickness, listed in **Table 4.1**. Measurements were taken from the different locations of the film to analyze the average thickness with standard deviation. Tensile strength was performed on pure CNC and FT1 samples at 50% RH by using Instron, Model No. 5982, Norwood, MA, with a crosshead speed of 1.5 mm/min.

4.3 Result and Discussion

We observed the formation of a completely transparent film through the freeze-thaw method, whereas the self-assembled film showed the formation of a fingerprint-like structure, indicating the presence of the chiral nematic organization depicted in **Figure 4.1**. This is likely because freezing the suspension caused physical aggregation of CNC through ice crystal formation that restricted the formation of the chiral nematic structure during thawing and drying. The formation of ice crystals towards the temperature gradient during the freezing of a colloid has been reported previously [140,141]. Onsager's theory discussed that the phase behavior of CNC in solvents is attributed to the system entropy [68]. More likely, during the thawing of the frozen CNC suspension, the CNC could not go back to its original state of crystal arrangement and lacked enough energy to rearrange itself into a chiral nematic structure while drying. This allows the

formation of a self-assembled CNC film without any structural color. We performed UV-Vis Spectroscopy to observe the transmittance profile over the wavelength ranging from 200 nm to 800 nm, shown in **Figure 4.2a**. The typical self-assembled CNC film shows a transmittance peak minimum as the chiral nematic structure causes circular polarization, resulting in iridescence [28]. The complete absence of the transmittance peak minima also confirmed that FT1 and FT2 film lacks any chiral nematic organization.

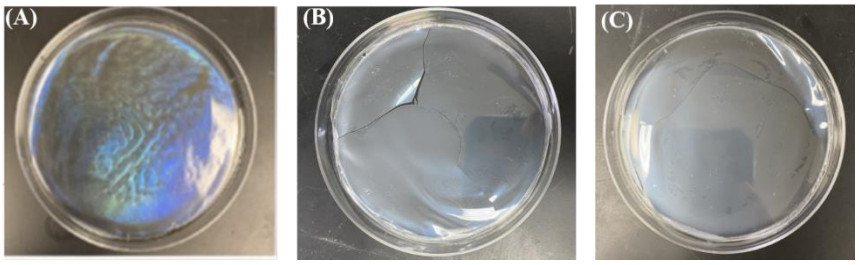

Figure 4.1 (A) Self-assembled Pure CNC film; (B) Freeze-Thaw cycle 1(FT1); (C) Freeze-Thaw cycle 2 (FT2)

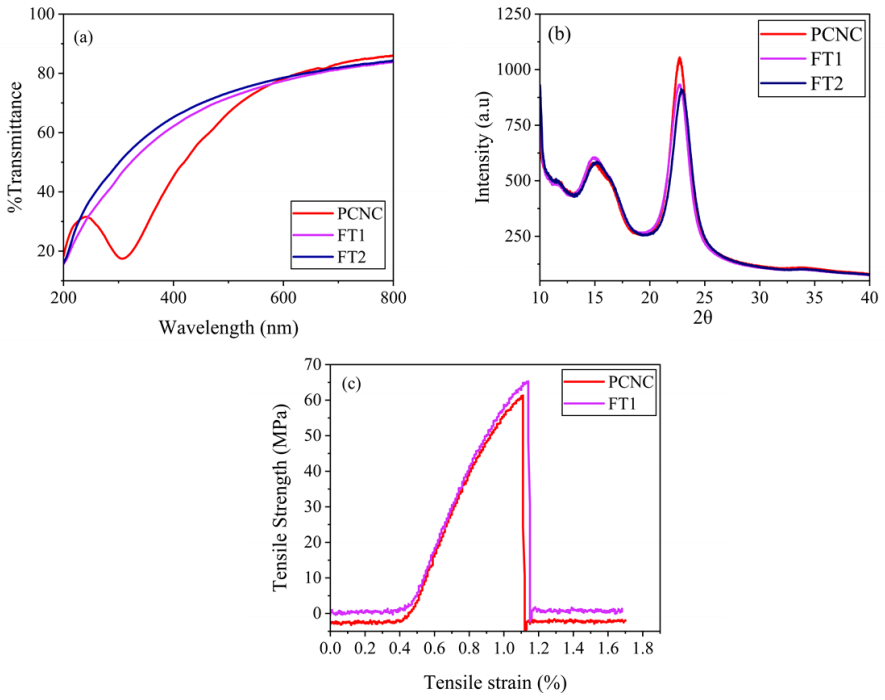

Figure 4.2 (a) Transmittance profile of the freeze-thaw film sample (b) XRD analysis of pure CNC (PCNC) and FT1 and FT2 sample (c) Tensile strength determination of PCNC and FT1

The X-ray diffraction, depicted in **Figure 4.2b**, was performed to check the crystalline structure of PCNC, FT1, and FT2 films. The CNC peaks were found at similar angles as pure CNC, 15.1°, 16.9°, and 22.7°, which indicated the preservation of the cellulose I crystalline structure [8,143]. This observation was also in agreement with Lewis et al. [141]. Only a slight drop in peak intensity was observed at 22.7°. Tensile strength determination, depicted in **Figure 4.2c, s**howed similar values as the pure CNC film (PCNC: 61.11 ± 10.34 and FT1: 60.37 ± 6.01). Porous CNC aerogel structure formation due to the freeze-thaw method was reported by Lewis et al. [141]. Further, an increase in water permeability was observed by Sun et al. [144] when a whey protein-CNC composite film was exposed to several freeze-thaw cycles post-film formation due to imposing stress on the structure. Possibly, the formation of physical aggregate, facilitated by ice crystals, created a void in the film structure, which caused a slight drop in intensity. This can be more clearly observed in the cross-sectional microscopic image, depicted in **Figure 4.3B, C**, and **D**, which shows a unidirectional straw-like structure devoid of any chiral nematic or fingerprint-like structure, as shown in **Figure 4.3A**. Ice crystal growth during freezing occurs in the same direction as the temperature gradient, which causes more compact and oriented CNC particles in the excluded volume between ice crystals. During thawing, the ice changed to a liquid phase without compromising the crystal orientation and evaporated during drying, likely without disorientation of the CNC arrangement. An observation by Han et al. [12] reported similar oriented ultrafine fiber texture formation for freeze-dried CNC. Further, slight voids or craters in the structure are also observed due to the formation of physical aggregates due to the formation of ice crystals. The cross polarized images of FT 1 and FT 2 in **Figure 4.4** showed a uniform texture, with a color and intensity contrast when rotated with respect to the polarizer. This further indicates the presence of nematic structure in the sample. Generally, the typical randomly localized multicolored domain

for self-assembled CNC film, depicted in **Figure 4.4,** was completely absent post freeze-thaw cycle.

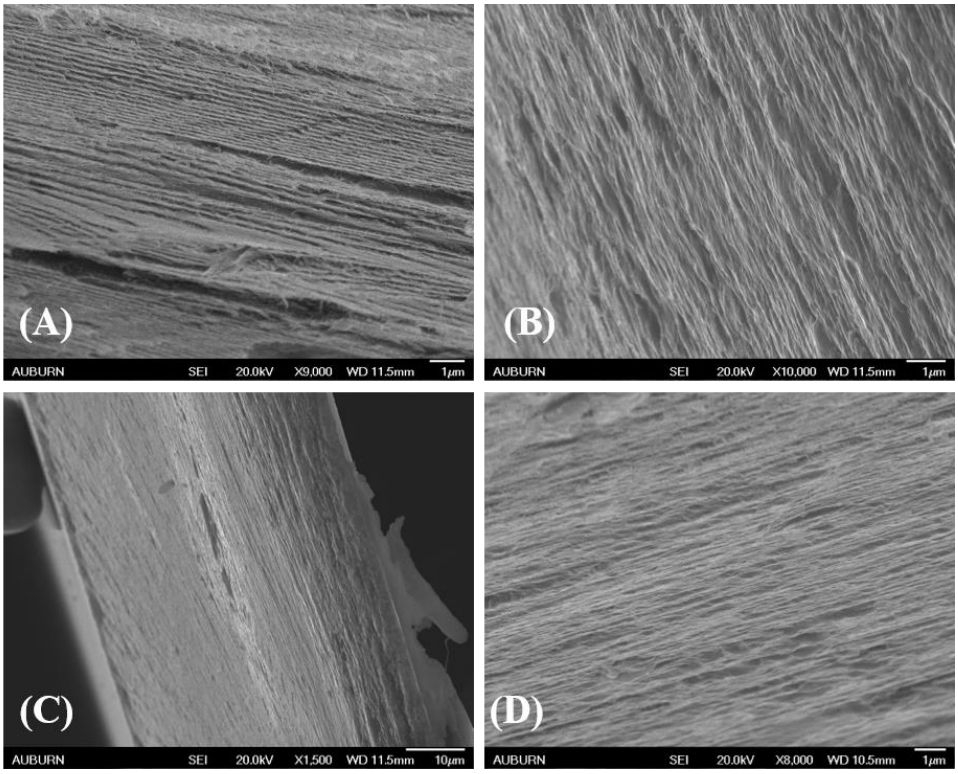

Figure 4.3 Cross-sectional SEM images of (A) Pure CNC (PCNC) film and (B-D) FT1 film; The working distance used for images A-C: 11.5 mm and D: 10.5 mm

We recorded the film thickness for PCNC and FT films, listed in **Table 4.1**, which indicated lower standard deviation value for FT films. Non uniformity in self-assembled film of pure CNC is reported by many and depends mainly on the rate of drying and the initial concentration [31,145]. Chang et al. [145] reported obtaining higher uniformity in the CNC film through slow drying with controlled humidity as compared to ambient air dryng. Interestingly, the freeze-thaw technique promoted ice crystal growth uniformly thorugout the dispersion, thus reducing non uniformity in the film to a certain extent.

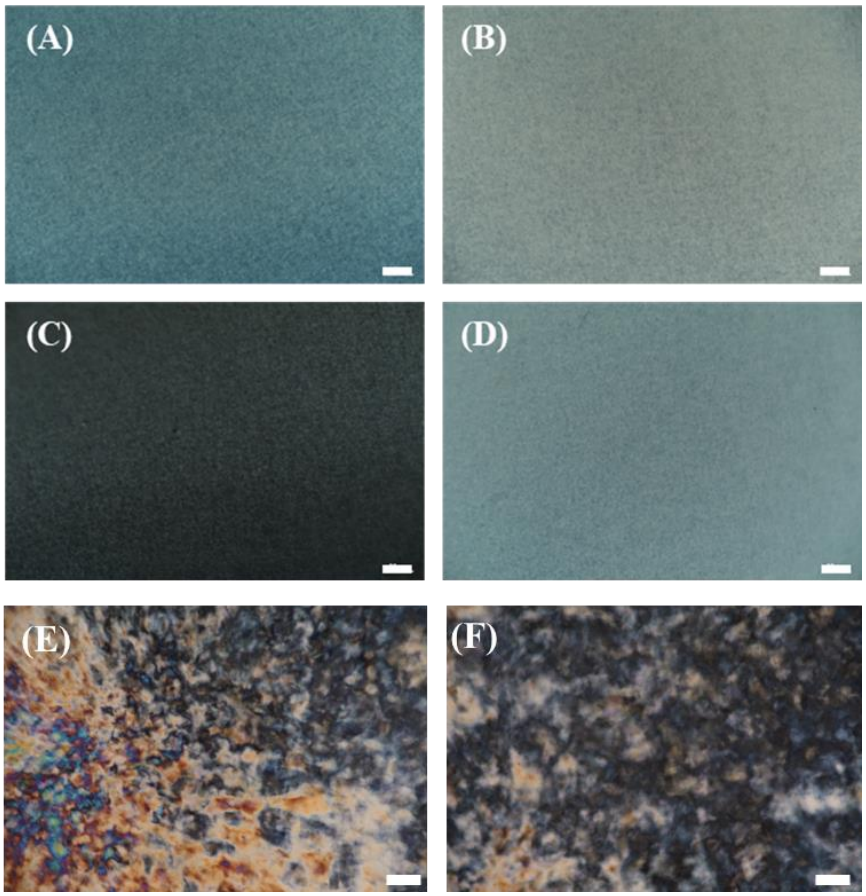

Figure 4.4 Cross-polarized images of: (A) FT1 at 0º, (B) FT1 at 45º (C) FT2 at 0º, (D) FT2 at 45º (E) PCNC at 0º, (F) PCNC at 45º Scale: 50 µm, Resolution: 20x

Table 4.1 Average thickness of the self-assembled films (PCNC, FT1 and FT2)

Sample	Average Film Thickness (µm)
Pure CNC (PCNC)	57.75 ± 18.95
Freeze-Thaw Cycle 1 (FT1)	40.60 ± 9.73
Freeze-Thaw Cycle 2 (FT2)	42.57 ± 12.54

We performed a detailed optical property analysis to quantify the transparency as listed in **Table 4.2**. The degree of transparency could be significant for certain applications such as in the electronic industry, coating on glasses, lenses, windows or packaging. A significant improvement in all the parameters compared to pure CNC film was observed. Though the change in transmittance and haze for FT1 and FT2 films did not significantly differ from pure CNC, remarkable improvement in clarity and sharpness factors was observed. Traditionally, low-angle

light scattering below 2.5° defines clarity [142,146]. The novel image based technique by Busato et al. [142] determine the transparency factor through illumination diffusion. Beside haze and clarity, a new factor, sharpness, is also introduced to quantify the resolution in fine detailing [142]. This sharpness can be considered as the function of clarity in quantification of see through quality of the material. The chiral nematic structure creates circular polarization of light. Thus, low-angle diffraction influences its optical quality. Further, the fingerprint structure of pure CNC film restricts sharp edge transition, thus reducing the sharpness of the film to a significant level, ~55%, depicted in **Figure 4.5 (A-B)**. The unidirectional CNC structure in FT films reduces the light scattering, and therefore, improves the clarity and sharpness to a significant level, i.e., ~ 99% and ~ 96%, respectively. The higher resolution of these FT films shown in **Figure 4.5 (C-D)**.

Table 4.2 Quantified optical properties of PCNC, FT1, and FT2 film (determined by imaging-based method [142,147])

Self-assembled film property				
	Transmittance (%) ~ 510 nm	**Haze (%)**	**Clarity (%)**	**Sharpness (%)**
PCNC	82.48 ± 1.91	9.38 ± 1.81	87.38 ± 1.71	55.35 ± 4.44
FT1	80.20 ± 0.28	11.95 ± 0.50	98.56 ± 0.13	93.86 ± 0.54
FT2	82.35 ± 0.49	9.36 ± 0.13	99.04 ± 0.06	96.06 ± 0.26

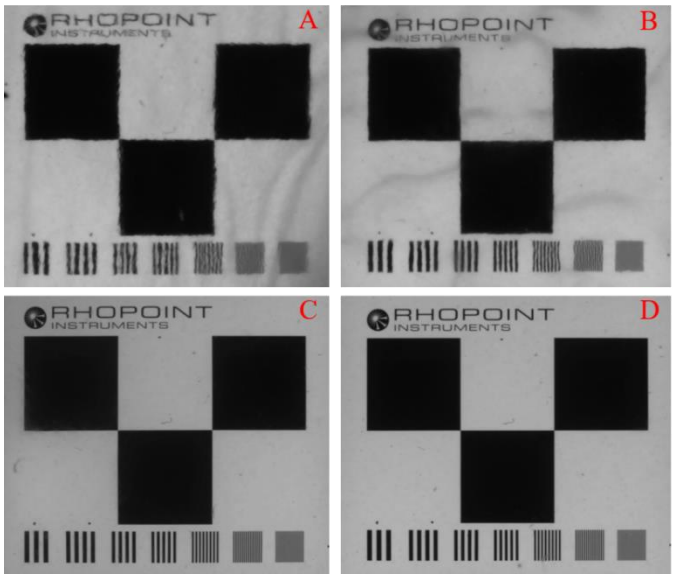

Figure 4.5 Image through Rhopoint ID-L to demonstrate higher sharpness or resolution visually (A-B) Pure CNC, PCNC film (C) FT1 film (D) FT2 film

4.4 Conclusion

We successfully demonstrated the formation of completely transparent CNC film through the freeze-thaw method. Thermodynamically, the self-assembly of charged CNC particles correlates with rotational and translational entropy. Freezing of isotropic CNC suspensions forms ice crystals and promotes physical aggregates of CNC crystal in an oriented manner. Our investigation showed that the phase change from ice to water did not affect the oriented CNC configuration. The system can likely does not have enough energy to revert to its original state while thawing. Thus, the formation of a chiral nematic structure was observed in the film. Remarkable improvement was obtained in the clarity and sharpness of the film without compromising transmittance and haze. Thus, the freeze-thaw technique could be a promising approach to produce transparent CNC film with good optical properties, and this method may be further utilized during composite preparation.

Chapter 5 Investigating Cellulose Nanocrystal and Polyvinyl Alcohol Composite Film in Moisture Sensing Application

5.1 Background

Optical sensors can have numerous advantages in industries like food, semiconductors, beverages, and packaging. Easy maintenance, wireless connectivity, and low-cost colorimetric optical sensors could be highly beneficial in detecting humidity or moisture content in systems [148]. Optical sensors are made by utilizing building blocks with unique structural colors generated due to light interference. Bird's feathers, fish scales, or insect cuticles are some examples of natural materials available [15]. Currently, colorimetric humidity sensors used for such applications contain cobalt chloride, which adversely affects human health [13,149]. Moreover, finite fossil fuel resources pose additional challenges as the photonic materials used to develop optical sensors are mostly from polymers, polystyrene spheres, graphene oxide [150–152]. Therefore, exploring biobased photonic materials to develop green, efficient, durable, low-cost, and non-toxic sensors is important.

Cellulose nanocrystal (CNC) is a biodegradable and renewable nanomaterial produced from biomass or agricultural waste, which is abundantly present in nature. [18,20,116]. Besides many valuable properties [6,20,51,63,99,118,123,137–139], CNC offers unique structural colors which can be utilized as a photonic material to develop optical sensors, ink, and displays [15,54,117]. Commercially, a rod-shaped CNC is extracted from cellulose by degrading the amorphous region through sulfuric acid hydrolysis [153,154]. This also incorporates sulfate esters on the surface of the CNC, by which the dispersion of CNC exhibits liquid crystal properties at higher concentrations [9,20]. CNC's liquid crystal structure exhibits chiral nematic organization, which is a helical arrangement of nematic layers around the cholesteric axis [20,68]. A complete rotation

of the structure around the axis is defined as a cholesteric pitch. This chiral nematic structure is restored in the solid self-assembled CNC film and exhibits structural color or iridescence. A typical reflectance or transmittance peak is observed for self-assembled CNC film in the range between 200 nm to 800 nm. The reflected wavelength can be tuned by altering the structure's chiral nematic pitch. This tuning can be obtained by the addition of external stimuli such as moisture, electrolytes, or polymers. The change in reflected wavelength directly alters the color of the material surface, thus creating an optical sensing capability for different conditions. It has been observed that the increment in pitch length causes the wavelength peak to shift to a higher value, thus exhibiting a redshift.

The iridescent property of CNC film has been investigated for use in optical sensor applications, which has been widely reported by many [13–15,55]. The re-dissolution of CNC in water creates poor cycling stability. Thus, CNC-based optical sensors are prepared by adding stimuli-responsive materials to CNC to prepare a composite that can offer stability as well as efficiency [148]. A CNC/polyethylene glycol (PEG) composite was reported to detect different humidity conditions [15]. Similarly, composites with glucose and glycerol were also used for humidity sensing [84,155]. The presence of abundant hydroxyl groups on CNC, coupled with these hydrophilic materials further increases the moisture intercalation in the structure to cause a redshift. However, higher humidity increases moisture absorption in the structure, which weakens the adhesion in the matrix, therefore softening the structure and impacting the structural stability and durability of the material [156]. CNC was also utilized with other materials, such as polyacrylamide, polyacrylic acid, polyvinyl pyrrolidone, and silver nanoparticles to detect organic solvents and their concentration, pH, and acid vapor [14,54–56,157]. Although multiple studies were carried out to

develop CNC-based optical sensors, factors like wireless connectivity, ease of operation, multifunctionality, durability, and biodegradability still need to be addressed.

Polyvinyl alcohol (PVA) is a non-toxic, biodegradable polymer containing abundant hydroxyl groups in its structure [158]. Several researchers obtained high mechanical strength and enhanced moisture barrier properties when CNC is added to PVA [159,160]. The application of PVA was also reported in developing optical fiber sensors for humidity sensing applications [161–164] or as self-healable electronic skin [165]. However, the utilization of PVA as a moisture-responsive material to develop a CNC-based photonic material is limited. Moreover, the utilization of PVA with CNC to prepare a colorimetric sensor or indicator is limited as well. Yu et al. [84] prepared a smart humidity-responsive photonic material with the addition of CNC/glycerol/glucose/PVA. In this study, glycerol and glucose both contributed to moisture absorption, whereas PVA addition was focused on the reduction of the film brittleness. An excellent solvent, acid, and alkali-resistant optical coating was developed by Zhang et al. [166] through the preparation of a CNC-PVA composite by glutaraldehyde crosslinking. Overall, the investigation of CNC-PVA composites as a colorimetric sensor in a moisture sensing application is still under evaluation and, therefore, requires a thorough investigation.

We have conducted the research in two parts. First, we investigated the responsiveness of the composite to moisture with respect to the following factors: PVA molecular weight, concentration, thermal crosslinking, and functionality of CNC. The addition of PVA to CNC causes reduced moisture sensitivity despite PVA's hydrophilic nature. In this study, we used PVA of varying molecular weight to investigate its effect on moisture sensitivity and prepared a complete green optical sensor with CNC and PVA that is responsive to high humidity conditions. We completed a study on the CNC-PVA composite's applicability in humidity sensing. Thermal crosslinking was

performed on the sensor to provide structural integrity during application. Therefore, its effect on optical properties was also determined. A detailed sensitivity analysis was provided for CNC-PVA composites by using PVA with three different (low, medium, and high) molecular weights. We further replaced the sulfated CNC with TEMPO-CNC to observe the sensor's moisture sensitivity. In the second part, a smart photonic material was developed that can broadly detect ethanol-water concentration. The insoluble nature of PVA in polar organic solvents made it resistant to structural disintegration when submerged in the solution. To the author's knowledge, this is the first time a detailed study has been presented to show the effect of PVA molecular weight, thermal cross-linking, and CNC functionality on designing CNC-PVA composite for moisture sensing application.

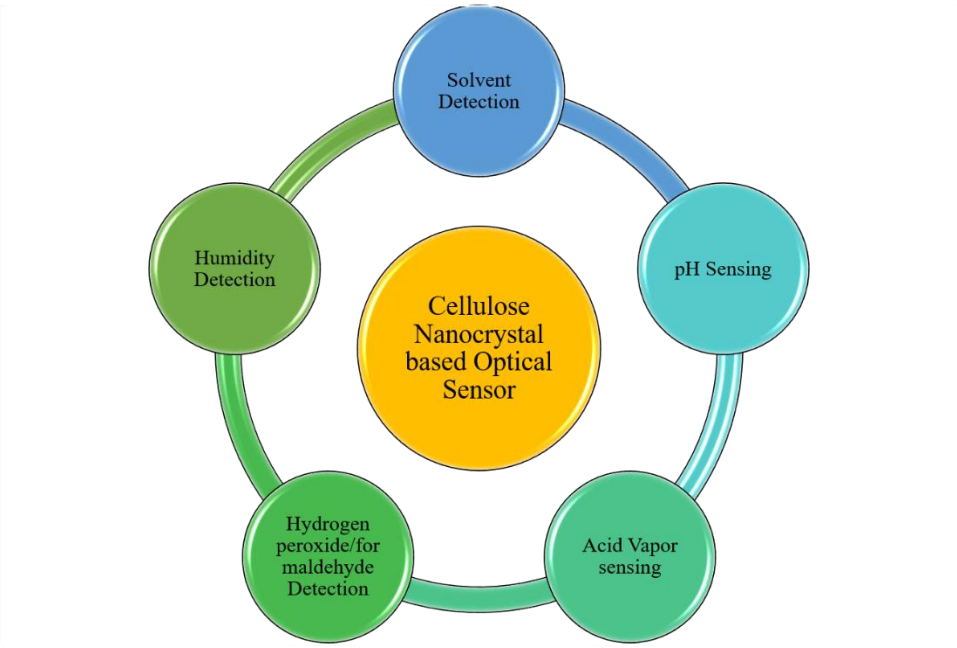

Figure 5.1 A overall schematic of the application area of CNC-based optical sensors

5.2 Materials and Methods:

Sodium form cellulose nanocrystal (CNC) aqueous gel was purchased from the University of Maine (Lot number 2021-FPL-CNC-170) with 11 wt% concentration and 1.1 wt% sulfur. 6.7 wt%

TEMPO-CNC (2,2,6,6-tetramethylpiperidin-1-piperidinyloxy oxidized CNC) was purchased from Anomera. Hydrolyzed polyvinyl alcohol (PVA) of different molecular weights was purchased: n = 1750 ± 50 (extremely low molecular weight - LLMW), 10k – 15k (low molecular weight - LMW) and 88k – 97 k (high molecular weight - HMW) was purchased from TCI America Inc., Alfa Aesar and BTC respectively. For organic solvent detection, anhydrous ethanol (200 proof) was purchased from VWR.

5.2.1 Composite Preparation

A self-assembled pure CNC and Tempo CNC were prepared by diluting the initial stock material with deionized (DI) water to 1.66 wt%. 0.4 g of CNC suspension was mixed with various weight percentages of PVA based on the initial amount of CNC, i.e., 0% to 50% and 100%. The detailed composition is listed in **Table 5.1**. A total 20 g suspension was prepared and magnetically stirred for 2 hours at room temperature. The films were developed by pouring the suspension into a polystyrene Petri dish and allowing evaporation at room temperature. The solid film was taken out after 3 days. The films were kept at 50% relative humidity (RH) with controlled room temperature. Thermal crosslinking was only performed on pure CNC-PVA composite films, which were kept in an oven at 150°C for 30 min. After this, the films were kept in a controlled environment for at least 24 hours before further experimentation. The final sensor preparation for ethanol-water concentration detection was carried out by sonicating the suspension for 1 minute with 25% amplitude to give uniform particle dispersion. Longer sonication time was avoided so that the CNC structure was not affected. A test paper method detection was used to determine the color change for organic solvent concentration detection. The sensor was cut into small rectangular strips and submerged in the solution for 4 minutes. A cyclic test was performed to determine the reusability of the film. 50 wt% ethanol-water solution was selected, and transmittance minima were recorded

for 10 iterations. At first, the dry initial state transmittance was determined, and then the film was dipped for 4 min in the solution for data collection. Around 7 to 10 min was required for the composite to return to its initial dry state.

5.2.2 Zeta Potential

The Zeta potential of pure CNC and TEMPO-CNC was determined using a Zeta sizer Nano ZS, Malvern instrument, listed in **Table 5.2**. The concentration used for the measurement is 0.83 wt%. A minimum of three measurements were performed to report the average value with standard deviation.

5.2.3 Scanning Electron Microscopy

A field emission scanning electron microscope, JEOL JSM-7000F, was used to take the cross-sectional image of pure CNC, TEMPO-CNC and CNC-PVA composite films. The films were exposed to liquid nitrogen before fracture and gold sputtered before imaging.

5.2.4 Cross-polarized Microscopy

Cross-polarized microscopy was performed by a Nikon (Melville, NY) Eclipse Ni microscope with a Nikon DS-RI2 camera and 20×/0.45 LU Plan Fluor to observe the birefringence property of the CNC-PVA composite. Two different angles, 0º and 45º was used to capture the image of the composite.

5.2.5 UV-Vis Spectroscopy

A Thermo Scientific Genesys 10S UV−vis spectrometer with a wavelength range of 200−800 nm was used to determine the transmittance profile of the samples. The minimum transmittance peak was used to indirectly correlate the pitch length and to detect the optical changes under external stimuli conditions.

5.2.6 Fourier Transform Infrared Spectroscopy (FTIR)

FTIR was performed to measure transmission spectra of pure CNC and TEMPO-CNC solid film by a Nicolet 6700 FTIR spectrometer, Thermo Scientific for the frequency range 500 - 4000 cm^{-1} with 64 cumulative scans.

5.2.7 Sensitivity Analysis

A relative humidity (RH) glass box was used to detect the transmittance peak shift when exposed to higher humidity conditions. Various saturated salt solutions produce different humidity conditions within a closed container. This study used 50% RH (controlled RH chamber) and 95% RH (humidity box) to conduct the following experiments.

5.2.8 Tensile Strength Determination

The tensile strength of the films was determined by using Instron, Model No. 5982, Norwood, MA (Load cell: 1 kN). Rectangular strips were cut and placed within a half rectangular frame to perform the test at 50% RH. The crosshead speed used for all the experiments was 1.5 mm/min.

5.2.9 Film Thickness

The thickness of the films was determined by Testing Machine Inc. Model 49-71 (0 - 1.25 mm range). Mostly, the thickness varied from (50-70) microns for Pure CNC and composite films.

Table 5.1 The detailed composition formulations for composite preparation (0.4g basis)

	Composite	PVA Concentration (wt%)
	Pure CNC	0%
CNC-PVA	CNC-LLMW	10%,20%,30%,40%,50%, 100%
	CNC-LMW	10%,20%,30%,40%,50%, 100%
	CNC-HMW	5%,10%,20%,30%
	Tempo CNC	0%
Tempo CNC-PVA	Tempo CNC-LLMW	30%,50%

Table 5.2 Zeta potential of pure CNC and Tempo CNC, the concentration used 0.83 wt%

Sample	Avg. zeta potential, mV
Pure CNC	-49.60 ± 0.71
Tempo CNC	-47.00 ± 0.42

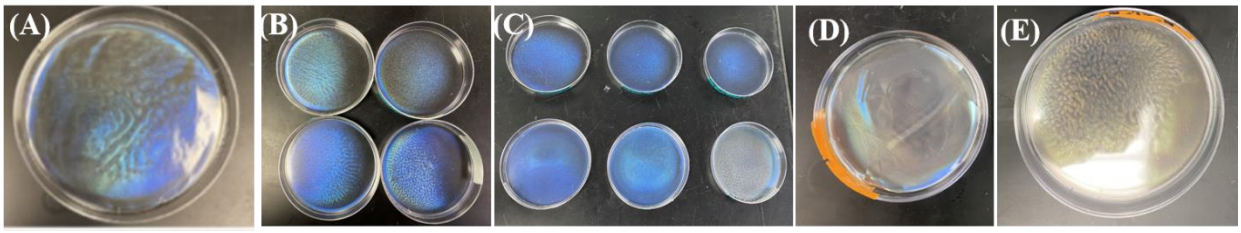

Figure 5.2 (A) Pure CNC and (B) Pure CNC - HMW PVA composite film; (C) Pure CNC - LMW PVA composite film (D) TEMPO-CNC (E) TEMPO-CNC – 50wt% LLMW PVA composite

5.3 Result & Discussion:

5.3.1 Effect of different MW PVA on Optical Response of Composite Films

The typical fingerprint or chiral nematic structure of self-assembled CNC film, depicted in **Figure 5.2A** becomes more uniformly distributed by the addition of PVA, shown in **Figure 5.2B** and **Figure 5.2C**. The addition of the PVA caused the red shift in the transmittance peak minima, λ_{min}, therefore a slight greenish appearance was observed with higher PVA concentration, depicted in **Figure 5.2**. The intercalation of a polymer chain in the CNC's helical structure expands the pitch,

which results in a redshift depicted in **Figure 5.3**. Wang et al. [167] reported the increase in half pitch of CNC structure with increasing PVA concentration and observed loss of ordered structure beyond 55 wt% PVA concentration. We observed this concentration was dependent on the molecular weight of PVA. The cholesteric pitch is correlated with Bragg's diffraction. Therefore, an indirect correlation can be drawn through the transmittance peak minima, λ_{min}. The absence of minima in the transmittance profile was considered as the disintegration of the chiral nematic structure, also reported and discussed by Wang et al. [34], and Parit et al. [107]. For LMW, up to 50 wt% concentration does not show any disintegration of the chiral nematic structure; however, at 100 wt% concentration, λ_{min} disappeared, indicating the loss of ordered structure, shown in **Figure 8.1a (Appendix C)**. For HMW PVA, 30 wt% concentration showed a drop in the peak wavelength, shown in **Figure 5.4a** indicating the chiral structure was in the process of disintegration (**Figure 8.1b (Appendix C)**). In contrast, an increase around ~200nm in λ_{min} was observed for the LLMW PVA addition from 10 wt% to 100 wt%, shown in **Figure 5.3** and **Figure 5.4b** and no structural disintegration was observed even for 100 wt%. Since a higher molecular weight represents longer polymeric chains with higher stiffness, when introduced into the CNC structure, it restricts movement during film formation, thus incorporating instability and disintegrating the chiral nematic structure [168]. Moreover, Yu et al. also reported the relationship between the threshold concentration and molecular weight [84].

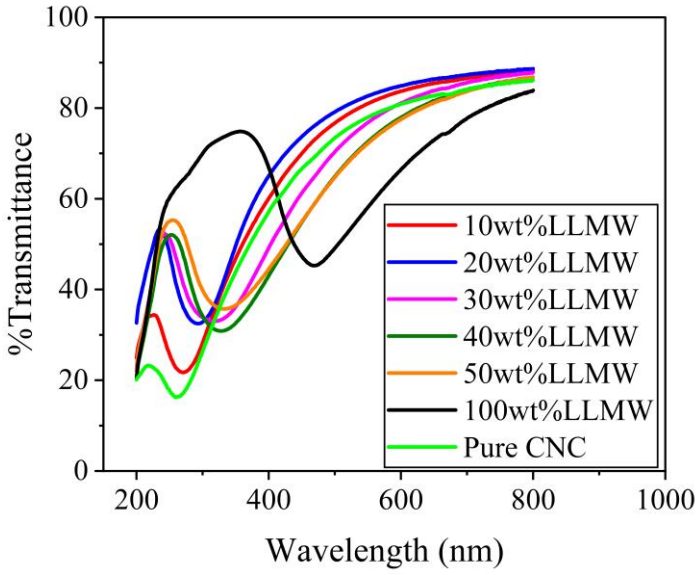

Figure 5.3 Transmission spectra of CNC-LLMW PVA composite films at various concentrations at 50% RH (without thermal curing)

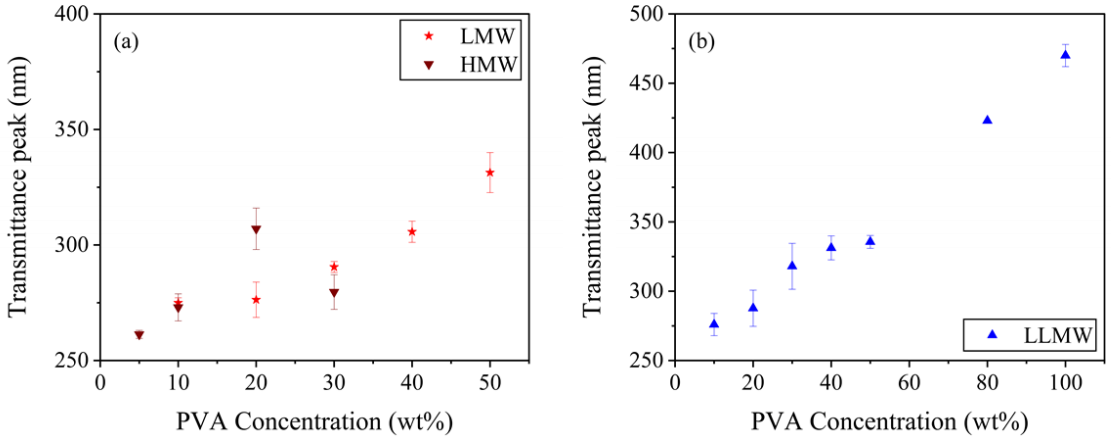

Figure 5.4 Transmission peak increment of (a) CNC – LMW, CNC – HMW, and (b) CNC-LLPVA composite films at various concentrations at 50% RH

5.3.2 Moisture Sensitivity Analysis of Composite Films

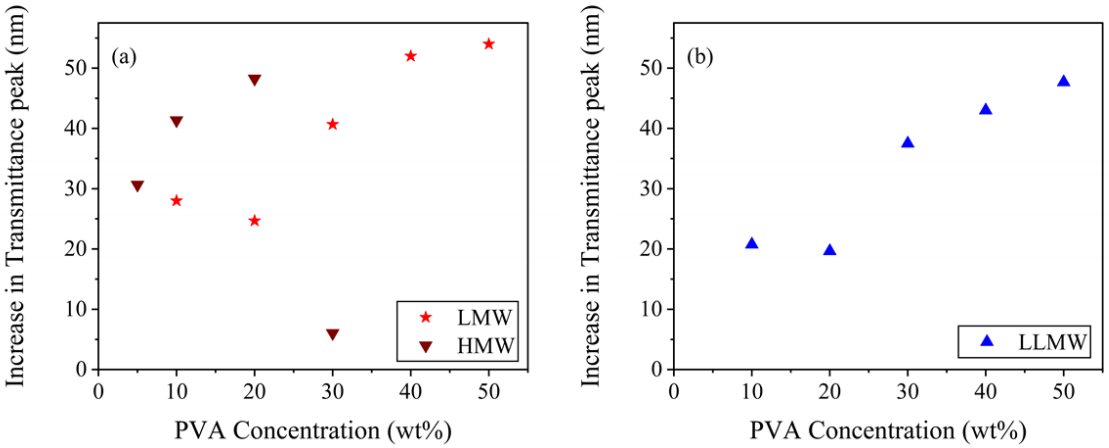

Figure 5.5 Moisture sensitivity analysis with respect to the different molecular weight of PVA (a) CNC – LMW and CNC-HMW and (b) CNC-LLMW composite films; peak increment from 50% RH to 95% RH

The composite films were exposed to 95% RH for 2 days to reach full saturation, and the λ_{min} was recorded to observe the change from 50% RH. The sensitivity analysis was performed to determine the composite's moisture absorption capacity at various PVA concentrations for different molecular weights, as shown in **Figure 5.5**. In the literature, a CNC/PVA composite was reported to have higher mechanical properties with low moisture uptake. Thus, the sensitivity analysis was important to determine the optimal molecular weight and concentration requirement. Nguyen et al. [169] and Silvério et al. [170] observed an increase in tensile strength and a decrease in water vapor permeability for CNC addition as an additive to neat PVA. For all molecular weights, the increase in moisture sensitivity was found to be quite low as ~ (10 - 15) nm. The addition of PVA to the CNC matrix creates hydrogen bond interactions between two components thus, reducing the accessible hydroxyl groups for moisture intercalation. Yu et al. [84] observed a drop in responsiveness to moisture with increasing molecular weight of PVA. This creates a challenge in the utilization of PVA with CNC as a moisture-responsive material for humidity detection. The

upper limit of the higher molecular weight PVA to prepare a stable composite further poses a challenge. Therefore, LLMW PVA was selected for high humidity detection.

5.3.3 Effect of Thermal Crosslinking on the Transmittance Peak Minima

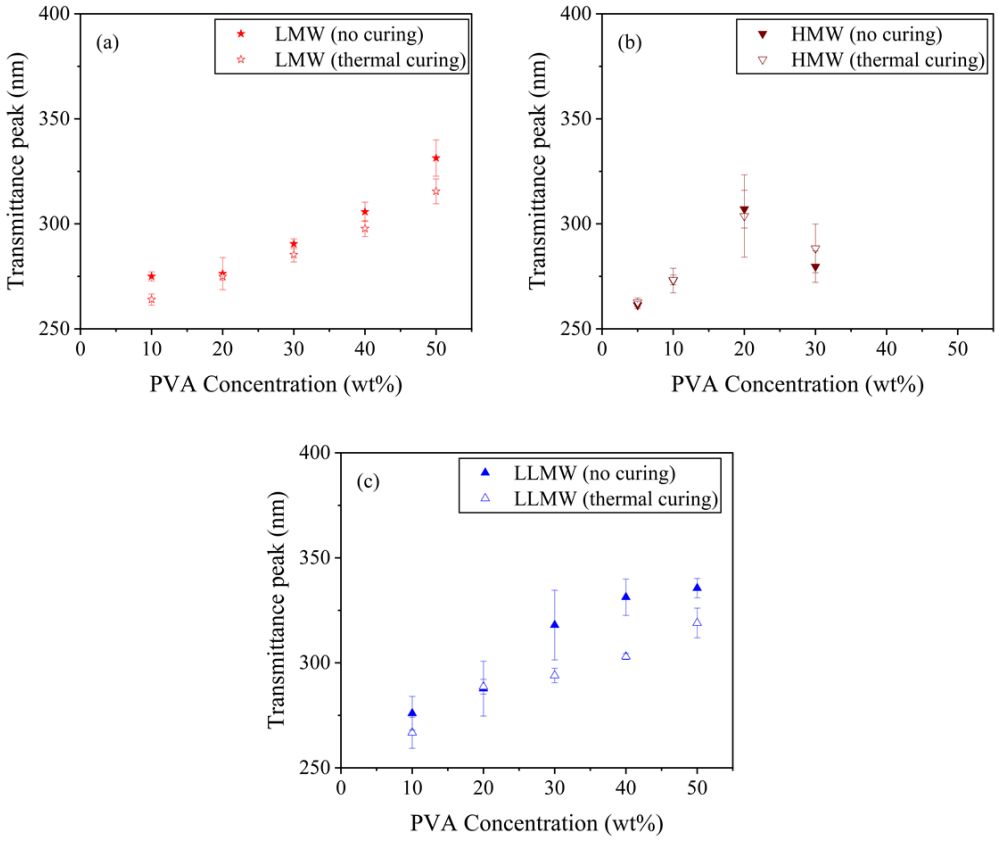

Figure 5.6 Transmission peak before and after thermal curing (a) CNC – LMW (b) CNC – HMW, and (c) CNC-LLMW composite films at various concentrations at 50% RH

The higher humidity exposure on the composite film causes a swollen structure due to moisture intercalation in the structure. This makes the composite more susceptible to structural damage and can affect the durability of the sensor. Thermal crosslinking causes the formation of hydrogen bonds by evaporating moisture from the structure. An increase in hydrogen bonds through thermal crosslinking was reported by Tsioptsias et al. [171]. Although thermal crosslinking can provide structural integrity [166,169] this can lead to the loss of available hydroxyl groups, thus reducing

the responsiveness to moisture. The effect of thermal crosslinking is depicted in **Figure 5.6**. A slight drop of transmittance peak minima was observed post thermal crosslinking due to the formation of more hydrogen bonding, which facilitates a shorter pitch. Around ~ 25 nm a decrease in λ_{min} was observed for 40 wt% LLMW PVA after thermal crosslinking. Since the λ_{min} decrease is not large, a thermally cross-linked CNC-PVA sensor can be considered for further experimentation.

5.3.4 Humidity Detection

The detection of high humidity was carried out using the CNC-80 wt% LLMW composite, and the result is shown in **Figure 5.7**. The presence of birefringence in the film, depicted in **Figure 8.2 (Appendix C)**, confirms the presence of the chiral nematic structure at 80 wt% LLMW PVA addition. Adding PVA restricts moisture intercalation in the structure and allows ~ 15 nm peak shift. Thus, a higher amount of PVA was required to ensure enough moisture penetration in the structure to observe the visual color change of the composite. LLMW PVA was selected as it can be used at up to 100 wt% in the composite preparation. Thermal crosslinking was also performed to evaluate the composite performance. The transmittance peak minima shift of around 80 nm was obtained for both with and without thermal crosslinking. Visually, the color change was identifiable and similar in both cases. The increase in the transmittance peak due to high humidity exposure was caused by swelling the chiral nematic structure, thus increasing the cholesteric pitch. This observation is in line with previously reported literature reported by Yao et al. [15] for CNC/Polyethylene glycol, and Lu et al. [148] for CNC/Polyacrylamide, etc. [13,54]. Lu et al. [148] observed a red shift of around 92 nm for relative humidity that increased to 97% RH. Again, the redshift was found to be quite significant for the CNC-PEG composite. The composite changed from green to orange when relative humidity increased from 30% RH to 90% RH [15]. The

composite's detection time was also experimentally determined and depicted in **Figure 5.7a.** The experiment continued up to 6 hours.; however, the maximum peak shift was observed at 2 hours and remained almost constant for the rest of the time. The structural integrity of the structure remained intact as the composites original state can be regained by exposing the film in 50% RH condition. To increase moisture sensitivity and response time, we further investigated the TEMPO-CNC-PVA.

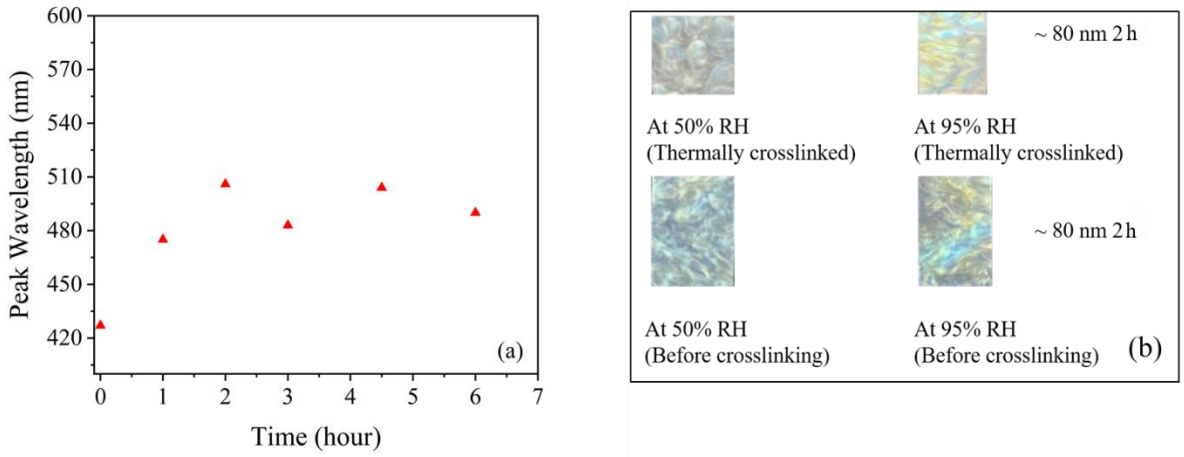

Figure 5.7 Humidity detection at 50% RH and 95% RH with CNC- 80wt%LLMW PVA composite (a) required time detection (b) visual color change (refer **Figure S.3** for transmittance spectra)

5.3.5 Effect of Polyvinyl Alcohol on Carboxylated CNC

The addition of the PVA to the CNC matrix caused limited sensitivity to moisture and showed prominent color change only at high humidity conditions. Moisture uptake was found to be dependent on the functionalization of cellulose. Previous studies showed higher moisture absorption for TEMPO-oxidized cellulose nanofibrils than sulfated ones [156,172]. Therefore, we incorporated carboxylated CNC in the composite to determine the composite's moisture sensitivity at 95% RH. Previously, glucose or glucan was used by Meng et al. [173] to develop a CNC based

humidity sensor. Additionally, Yu et al. [84] prepared a CNC/glucose/glycerol/PVA composite for a similar application. The chiral nematic structure of pure TEMPO-CNC is shown in Figure 8A, where the typical fingerprint structure can be observed. Compared to the pure CNC, TEMPO-CNC showed a peak shift from 1637 to 1602 cm^{-1}. Hop et al. also noticed this typical peak shift post-TEMPO oxidation [174]. Further, a broad and higher intensity peak from ~ 1602 to 1637 cm-1 was noticed, indicating a qualitatively higher amount of carboxylic acid groups in the structure, depicted in **Figure 5.8B**. Carboxylated CNC was used to prepare a composite with PVA and moisture intercalation, and time was recorded. Pure TEMPO-CNC exhibited transmittance minima around 440 nm, which red shifted ~ 520 nm for 30 wt% LLMW PVA addition and completely disappeared for 50 wt% PVA, shown in **Figure 5.8C**. Visually, the structural iridescence was weaker than the pure CNC, depicted in **Figure 5.2D** and **Figure 5.2E**. This limits the range of PVA addition that can be used to prepare the composite. TEMPO-CNC was also used to further evaluate the increase in sensitivity and observed only a slight increment in λ_{min} ~ 60 nm for 30wt% LLMW PVA addition. Although we observed increased moisture absorption through λ_{min} shift by introducing carboxylic acid groups, the upper limit to add LLMW PVA was lower than pure CNC, thus limiting the application in humidity detection.

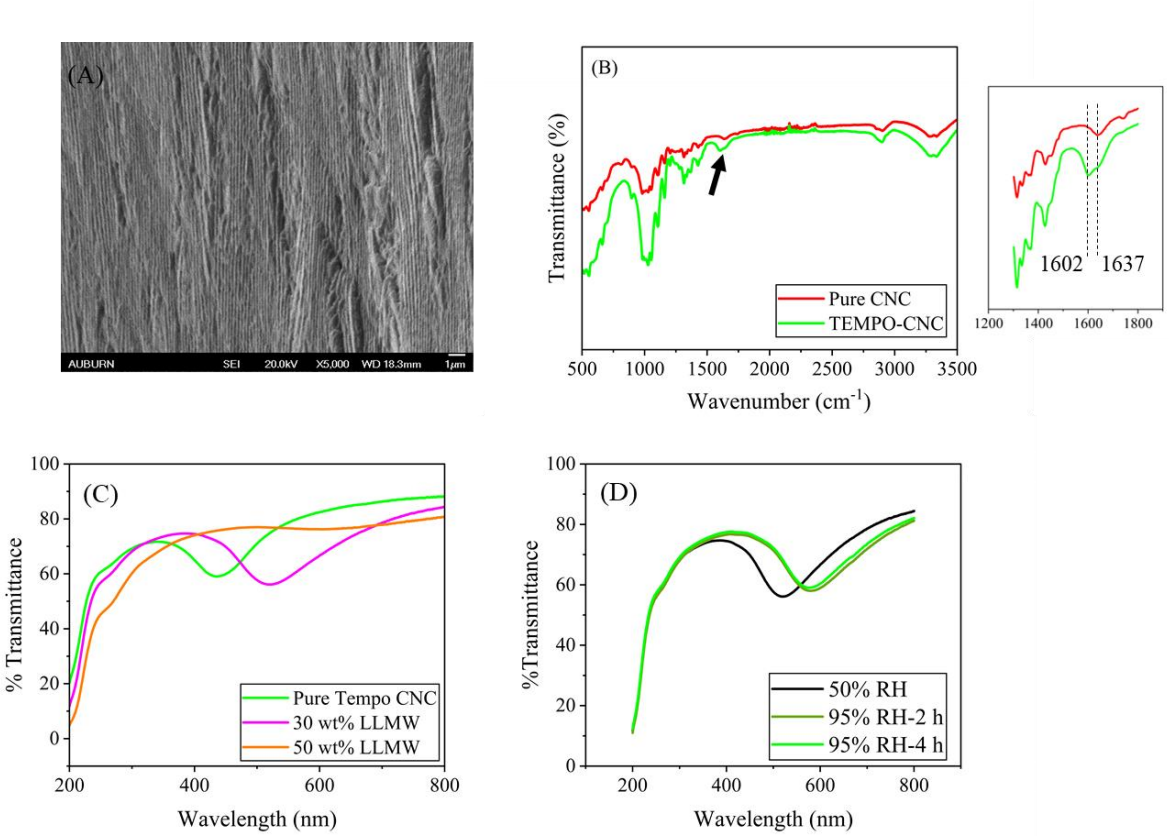

Figure 5.8 (A) Cross-sectional SEM image of TEMPO-CNC, scale bar: 1 μm, (B) FTIR spectroscopy of Pure CNC and TEMPO-CNC, (C) Transmission spectra for TEMPO-CNC with 30wt% and 50wt% LLMW PVA, (D) Transmission spectra of Tempo CNC-30wt%LLPVA composite films at 50% RH and 95% RH for 2 and 4 hrs.

5.3.6 Morphology and Mechanical Property

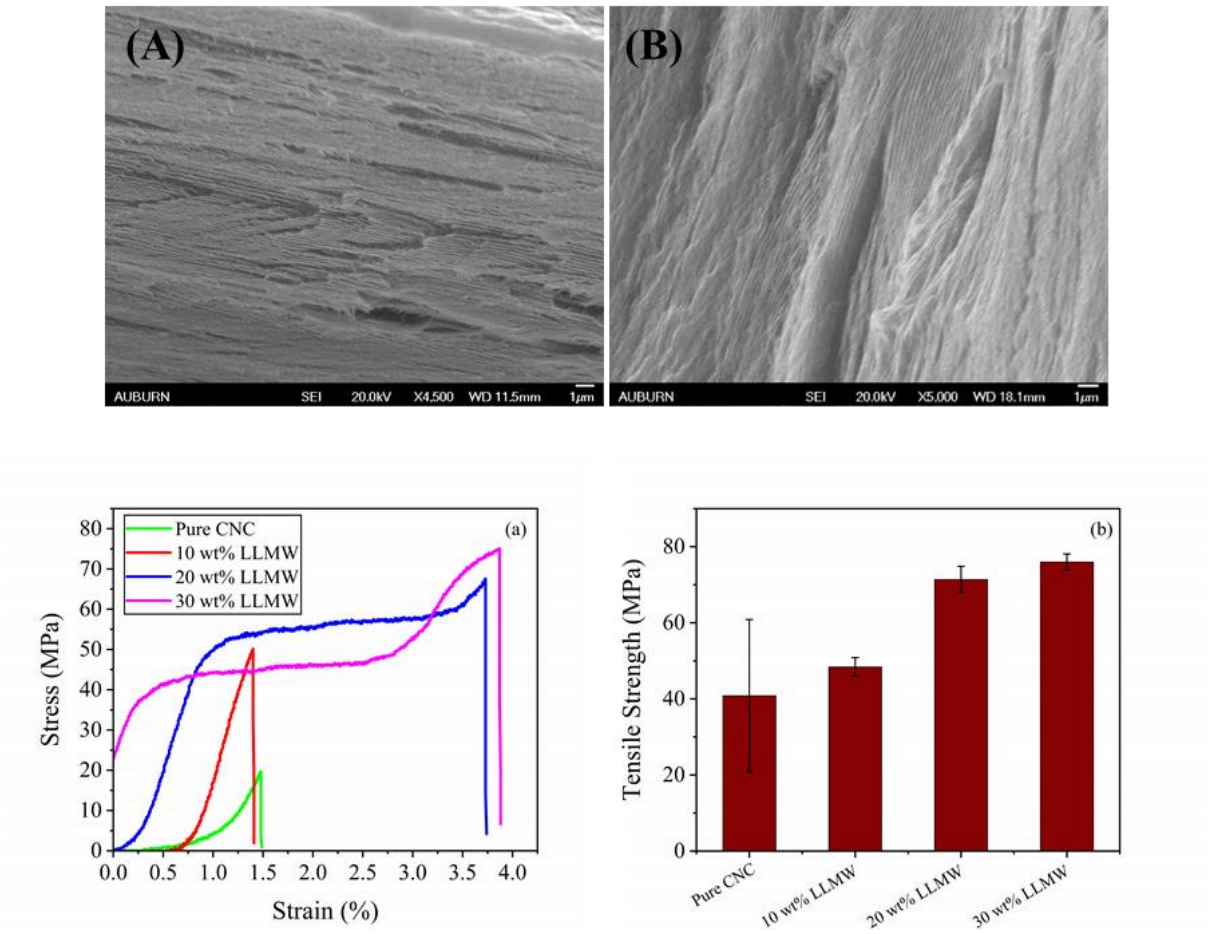

Figure 5.9 Upper row: Cross-sectional images of (A) Pure CNC (B) CNC-80wt% LLMW PVA composite, scale bar 1μm; Bottom row: (a) Stress-strain property of pure CNC and LLMW PVA composite film (10-30) wt%, (b) Tensile strength of pure CNC, CNC-PVA composite

The cross-sectional image of pure CNC shows the typical finger print texture, depicted in **Figure 5.9A.** The CNC-PVA cross-sectional image shows the presence of CNC structure between the PVA matrix. The tensile strength was determined for 10 to 30 wt% LLMW CNC-PVA composite to demonstrate the structural integrity of the composite. Addition of PVA exhibited increase in elongation at break, that is, from ~ 1.5% to 3.8% for 30wt% PVA. The addition of soft PVA in the CNC matrix provided more energy dissipation while stretching, displaying prominent plastic deformation, whereas pure CNC showed a sharp fracture depicted in **Figure 5.9a (bottom row)**

[166]. Similarly, Zhang et al. [166] also reported observing plastic deformation for CNC and PVA composite as well. We observed an increase of tensile strength from ~ 40 MPa to ~ 70 MPa by the addition of 30 wt% LLMW PVA. The hydrogen interaction between CNC and PVA created a stronger structure, thus increasing tensile strength. A similar observation was reported by Zhou et al. [51], where tensile strength and elongation at break increased up to 3 wt% CNC addition in neat PVA.

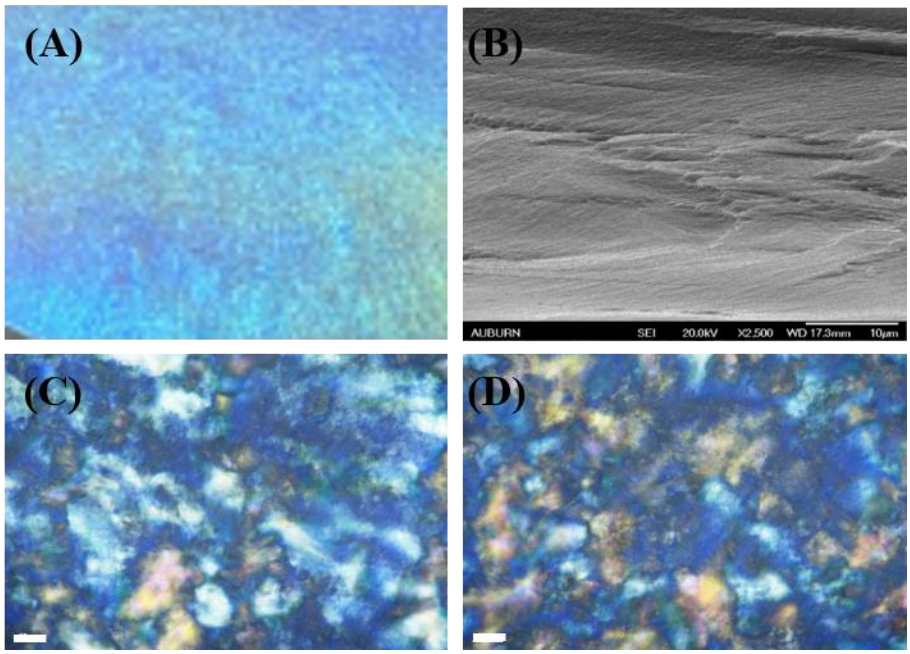

Figure 5.10 Final sensor images of CNC-40wt% LLMW PVA (sonicated) (A) Digital image (B) SEM image; scale bar 10 µm (C) Cross polarized image at 0º to polarizer; scale bar 50 µm (D) Cross polarized image at 45º to polarizer; scale bar 50 µm

The physical mixing of CNC and PVA through magnetic stirring does not create a uniform matrix. Therefore, to prepare the final sensor for ethanol-water concentration detection, 1 min of sonication of the suspension was performed to disperse the CNC and PVA homogeneously, which produced a more uniform visual texture in the matrix, as shown in **Figure 5.10 (A) (B)**. Extended sonication can impact CNC morphology, therefore sonicating the suspension for longer time was

avoided. The colorful texture shown in **Figure 5.10 (C) (D)** confirms signature birefringence, thus confirming the available photonic property of the composite. We utilized 40 wt% LLMW PVA to prepare the sensor, which can deliver sufficient resilience to the sensor and provide the required performance.

5.3.7 Ethanol-Water Concentration Detection

The reported literature on organic solvent concentration detection through CNC-based optical sensors is limited. Gao et al. [55] developed a CNC/polyvinylpyrrolidone composite for determining different organic solvents, including methanol, ethanol, and chloroform. Similarly, Bai et al. [117] and Verma et al. [152] prepared CNC/citric acid composites to detect different organic solvents. Kelly et al. [54] demonstrated CNC/polyacrylamide-based photonic hydrogels for the detection of water concentration in ethanol and broadly depicted the hydrogel's color change through polarized optical microscopy.

The insoluble nature of PVA in polar organic solvents was utilized here to develop a biodegradable, easy maintenance, low-cost, and durable sensor that can efficiently detect water concentration in ethanol. The insoluble nature of PVA to polar organic solvent prevents the composite from disintegrating or swelling when submerged for a day, as depicted in **Figure 8.4 (Appendix C)**. Adding PVA to CNC allowed the composite to remain stable in ethanol-water solution at different concentrations. An easy and facile method, i.e., dipping the film in the solution (4 min), was developed to record λ_{min} (immediately after taking the film out) shift at different ethanol-water concentrations, as depicted in **Figure 5.11.** This allowed the composite to remain intact post-experimentation. The method is detailed in the **Section 5.2.1**.

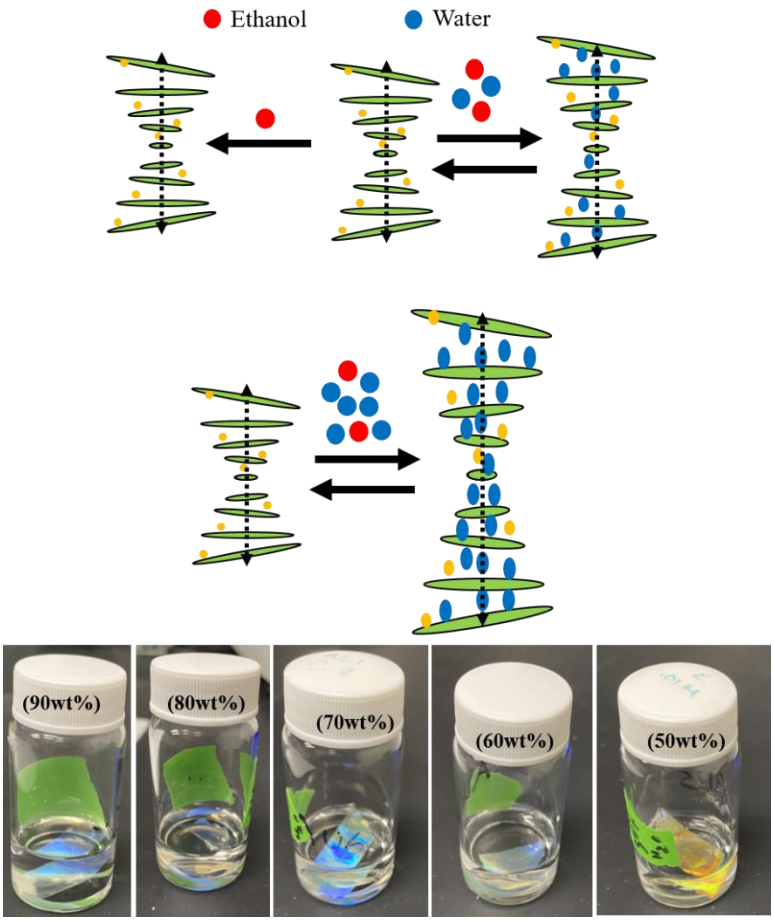

Figure 5.11 The Pure CNC – 40wt%LLMW PVA – test method demonstration, image taken after 2 min of submerging

With increasing water concentration, the red shift in the transmittance profile was observed for the composite, which is shown in **Figure 5.12**. The exposure time for all concentrations was 4 minutes. Therefore, the cholesteric pitch increment occurred due to increased available water molecules in the solution, illustrated in **Figure 5.11**. The addition of 20 wt% water shifted the λ_{min} around 55nm. The more significant color change began from 30 wt% water content, resulting in olive green color with a peak shift of ~ 116 nm. A complete orange color was obtained for 50 wt% water content, and a significant transmittance minima shift occurred ~ 230 nm. Though 10 wt% water content did not show significant color change, a slight peak shift occurred, as depicted in **Figure 5.12**. Interestingly, the highest peak in the transmittance profile also showed an increase in

percent transmittance and a small red shift in wavelength as well. A slope ratio was calculated by considering the slope of the before and after the peak (**explained in Figure 8.5 (Appendix C)**), which showed a consistent behavior with increasing water content in ethanol-water solution. The ratio of this slope exhibited a decreasing pattern with increasing water concentration, as shown in **Figure 5.13a**.

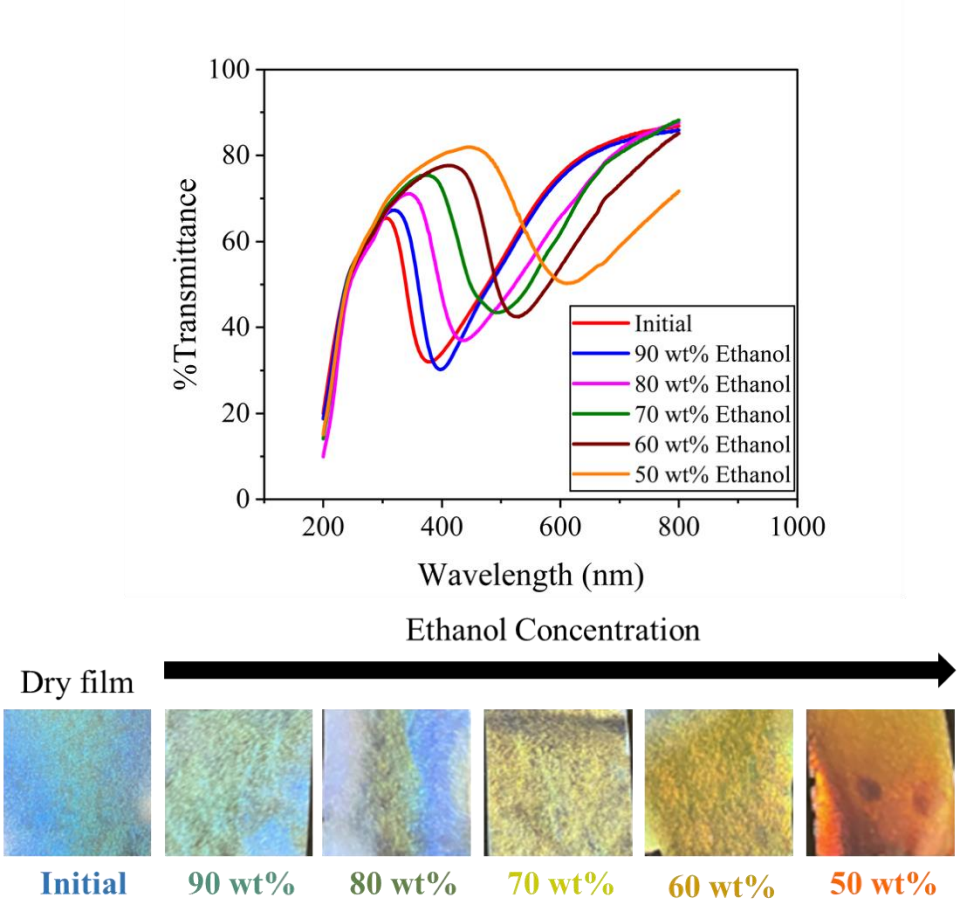

Figure 5.12 The Pure CNC – 40 wt%LLMW PVA film color variation at time = 4 min with different water concentrations in ethanol and transmittance profile at different ethanol-water concentration

Finally, a cyclic test was performed for 10 iterations with the 50 wt% water concentration in the solution to conduct a performance check. The detailed description of the cyclic test is included in the **Section 5.2.1**. The presence of a higher amount of water can affect the film's performance;

therefore, we opted for a 50 wt% ethanol-water solution, which demonstrated repeatable data throughout all the iterations, as depicted in **Figure 5.13b**. Therefore, the water concentration in ethanol can be detected via this composite through its transmittance profile and color change up to 10 wt% water concentration. This optical sensor can broadly be utilized in organic solvent dehydration applications.

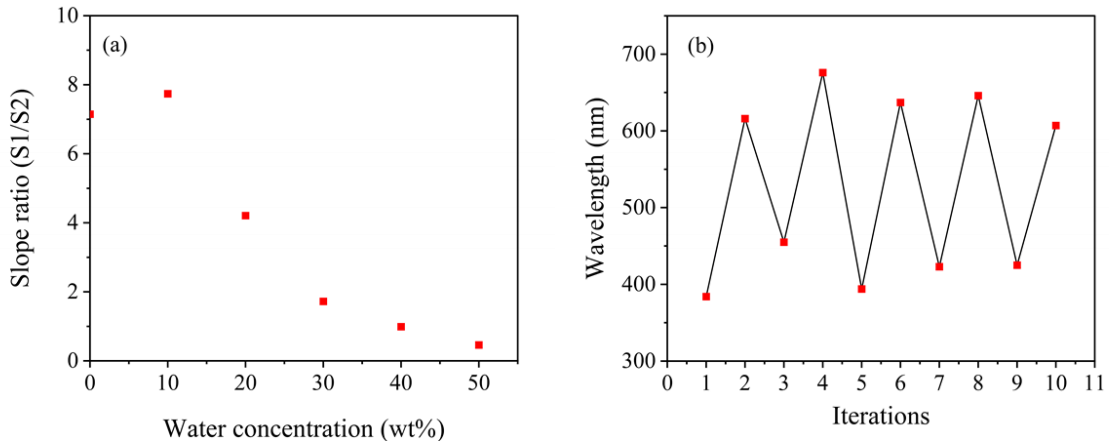

Figure 5.13 The Pure CNC – 40 wt%LLMW PVA film: (a) Slope ratio with respect to the water concentration (b) Cyclic test performed with 50% ethanol-water solution

5.4 Conclusion

The CNC-PVA composite showed excellent optical sensing properties when detecting water concentration in ethanol-water solution. Significant visual color change of the composite has been observed with distinct transmittance minima increments. We also observed that the slope ratio of the curve changed and exhibited a decreasing pattern with the increased water concentration. Consistent results were found when the composite was subjected to 10 iterations.

The detailed study on the moisture sensitivity of the CNC-PVA composite exhibited limited applicability in humidity sensing. The addition of PVA to CNC forms hydrogen interactions that reduce the availability of hydroxyl groups for moisture capture. A similar observation was also found for TEMPO-CNC as well. We observed a slightly increased moisture sensitivity for

TEMPO-CNC; however, adding 50 wt% of the lowest molecular weight PVA (n =1750) showed structural disintegration, which again imposed limitations on the formulation and moisture sensitivity. Our study demonstrated that with increasing molecular weight of PVA, CNC's structural disintegration occurs with a reduced amount of PVA addition. Further, moisture sensitivity did not differ much with the thermal crosslinking of the composite. Therefore, we believe this composite can be useful in high humidity sensing and ethanol-water concentration detection.

Conclusion

The research successfully demonstrated the different routes to develop CNC and CNC-based green composite films which exhibit good optical properties and can be used in various domains like coating, packaging, piezoelectric applications and as an optical sensor. Transparency is achieved in such films either by higher CNC orientation or by restricting the formation of cholesteric or chiral nematic structure. Addition of electrolytes (NaCl, CsCl, $CaCl_2$ and NaOH) to CNC gel to their transition concentration screens off the double layer by neutralizing anionic surface charge, thus weakening the electrostatic repulsive force which plays a crucial role in formation of cholesteric phase. At transition concentration, chiral nematic structure collapses into the nematic structure, therefore, by mechanical shearing to these electrolytes added CNC gel, high order parameter S ~ 0.88 at 20 s^{-1} was achieved whereas only S ~ 0.32 order parameter was obtained for pure CNC gel for 20 s^{-1}, 40 s^{-1} and 100 s^{-1} shear rate. The cationic bridging strength of these electrolytes played a crucial role in determining the required shear rate to achieve a similar degree of orientation. A larger or softer cation (Cs^{+}) or higher valency (Ca^{2+}) cation exhibit stronger interaction with CNC, thus creating a much stronger gel which required a higher shear rate to orient the CNC. Contrastingly, altering the pH ~ 12 resulted in entirely different behavior and produced weaker gels compared to other electrolytes. Higher pH is responsible for deprotonation which affects stability of the CNC gel and showed a sharp increase in storage modulus over a small-time span. The ionic migration could be a possible explanation for this which also affected the CNC alignment during drying, thus achieving order parameter S ~ 0.6 which was low in comparison to the other electrolytes. Additionally, the flexibility of these electrolyte added films improved which was observed qualitatively. Overall, being a common salt, NaCl was found to be

a suitable choice for practical application as it showed higher CNC alignment for a very low shear rate i.e., 20 s^{-1}.

Restriction to form cholesteric structures was also observed when isotropic dispersion of commercial CNC was treated with NaOH. NaOH treatment of commercial CNC created an oriented structure for both 1 and 4 hours. of reaction. Commercial CNC contains impurities like hemicellulose or small organic molecules that degrade during alkali hydrolysis, and small anionic species are retained even after extensive lab-based purification. Obtaining more of a negative zeta potential post reaction indicates the presence of higher anionic charges in the system. Most likely, these excess anionic charges coupled with reduced sulfur content in CNC promoted the formation of a complete nematic structure in dried self-assembled film. Excess anions in the system restricted the formation of cholesteric structures through the increased electrostatic repulsion, creating a nematic configuration. A thorough analysis of the optical properties of these films in comparison to pure CNC film showed remarkable improvement in terms of haze, clarity, and sharpness. A green composite preparation with modified CNC and PVA resulted in better optical performance, which can be utilized in packaging or coating applications especially in the electronic domain where transparency is important. Beyond the chemical treatments, facile methods like freeze-thaw can create CNC films with better optical properties. The freeze-thaw technique created an orientated template in the frozen CNC isotropic dispersion through ice crystal formation which restricted the formation of chiral nematic structure in a self-assembled film, thus creating a completely transparent, nematic CNC film suitable for packaging application. The frozen CNC configuration formed during freezing lacked the energy to revert back to its original self-assembled state throughout the thaw and drying process. Interestingly, improved uniformity was identified in the film through the process without compromising the mechanical property as well.

Lastly, CNC-PVA a biodegradable composite was prepared to demonstrate its applicability in detecting water concentration in ethanol through color change which can have potential application in organic solvent dehydration industry. The insoluble nature of PVA to ethanol provides stability to the composite. On the other hand, the hydrophilic nature of PVA also assisted in the moisture absorption in higher humidity conditions. The composite efficiently detected the water concentration in ethanol in the range 10 to 50 wt% through distinct color change from blue to red. With increasing water content, the red shift was observed in transmittance peak minima. The composite showed moisture sensing capacity at higher humidity, such as 95% RH which can be beneficial in food packaging application. Addition of PVA results in structural integrity which further increased through thermal crosslinking. A detailed investigation showed thermal crosslinking did not compromise the moisture sensing capability, thus could be an interesting method to use the composite in the related application.

Future Work

Effect of Circular Shear on the Optical Properties of Cellulose Nanocrystal Film

Cellulose nanocrystal (CNC) is a green nanomaterial produced from cellulose that has gained popularity over the years for its multiple applications in various fields, like additives in composite preparations to increase mechanical strength, as a coating material to improve gas barrier properties, in composite preparations for packaging industries, and piezoelectric application [6,18,48,49,51,52,57]. Numerous studies have been carried out to enhance the properties of CNC and improve utilization of the material in various fields. In the packaging and coating area, optical properties of the CNC film are important to consider. Self-assembled CNC solid film exhibits structural color or iridescence due to CNC's chiral nematic organization in dispersion. Different mechanisms have been explored in the literature for the formation of transparent, homogenous CNC solid film, however, a detailed correlation with the optical properties and investigation on CNC types has not been widely discussed before.

Sulfuric acid hydrolysis is used widely to generate CNC by degrading the amorphous region, thus retaining the crystalline part with anionic sulfate ester groups on the surface [9,33]. These anionic surface charges play a crucial role in the dispersion of CNC in aqueous media as well as formation of chiral nematic structure at higher concentrations. Four distinct phase behaviors are observed for sulfated CNC at different concentration, isotropic, biphasic, liquid crystalline and the gel phase [68]. The chiral nematic structure can be understood as the director n or nematic planes arranged in a left-handed helical fashion around the cholesteric axis. The length required to complete 360º rotation by the director, n is defined as helical pitch, P [175]. The helix orientation in a CNC dried film can vary in three different ways: planar (helix orientation perpendicular to surface of the film), homeotropic (parallel helix to the film surface) and focal conic (where both helix arrangements

can be observed) [175]. The homeotropic arrangement exhibits the characteristic fingerprint texture under cross-polarized microscopy. CNC films exhibit multicolored structure post evaporation. The digital color was observed in a dried CNC film as it selectively reflects left-handed circular polarized light at a particular wavelength reported by Dumanli et al. [176] . The local arrangement of the helixes and the pitch length in the film results in small domains which reflect different set of wavelengths, therefore controlling the optical property of the film [20,82]. The photonic property of CNC film can be used in various domains such as optical sensor, decorative films, and security papers. However, obtaining uniform helix distribution from self-assembled air-dried CNC film is challenging due to poor control over helix arrangement, resulting in a mosaic-like, defect-rich structure [175,176].

Previous literature demonstrated a facile method to control helix orientation and pitch length to provide uniformity in the film. Park et al. [177] observed the formation of planar anchoring through orbital shear flow, however, pitch length variation in the film was observed. Further, nullifying the concentration gradient due to rotational shear created higher uniformity in the film reported by Ličen et al. [178]. Later, Saha et al. [175] demonstrated reduction in pitch variation through humidity controlled drying. Overall, factors like CNC concentration, controlled evaporation and orbital shear speed affect the optical property of the CNC film [175–179].

To determine the effect of rotational shear through orbital shear on CNCs counterion, functional group and overall transparency, a framework was developed where sulfated CNC, dialyzed CNC and TEMPO-CNC were used. 11 wt% sodium form CNC aqueous gel was purchased from University Maine with 1.1 wt% sulfur content. This sodium form of sulfated CNC was termed as PCNC. Further, this CNC was dialyzed extensively for 20 days and termed as DCNC. Lastly, 6.7 wt% TEMPO-CNC was purchased from Anomera and named as TCNC. Two different methods

were used to prepare to the CNC film, self-assembled (S.A.) and films prepared by orbital shaker. 1.66 wt% aqueous dispersion of CNC was used to prepare all types of CNC film. The self-assembled films were prepared by pouring 20 ml dispersion into a polystyrene Petri dish and allowing the water to evaporate under ambient conditions. Around 2-3 days were necessary to prepare a completely dried CNC self-assembled film. To prepare circular shear-based films, 60 and 85 rpm were used in the orbital shaker and the films were allowed to dry under rotating motion under ambient conditions. 0.4 g of CNC was used as the basis to prepare the dispersion for film preparation.

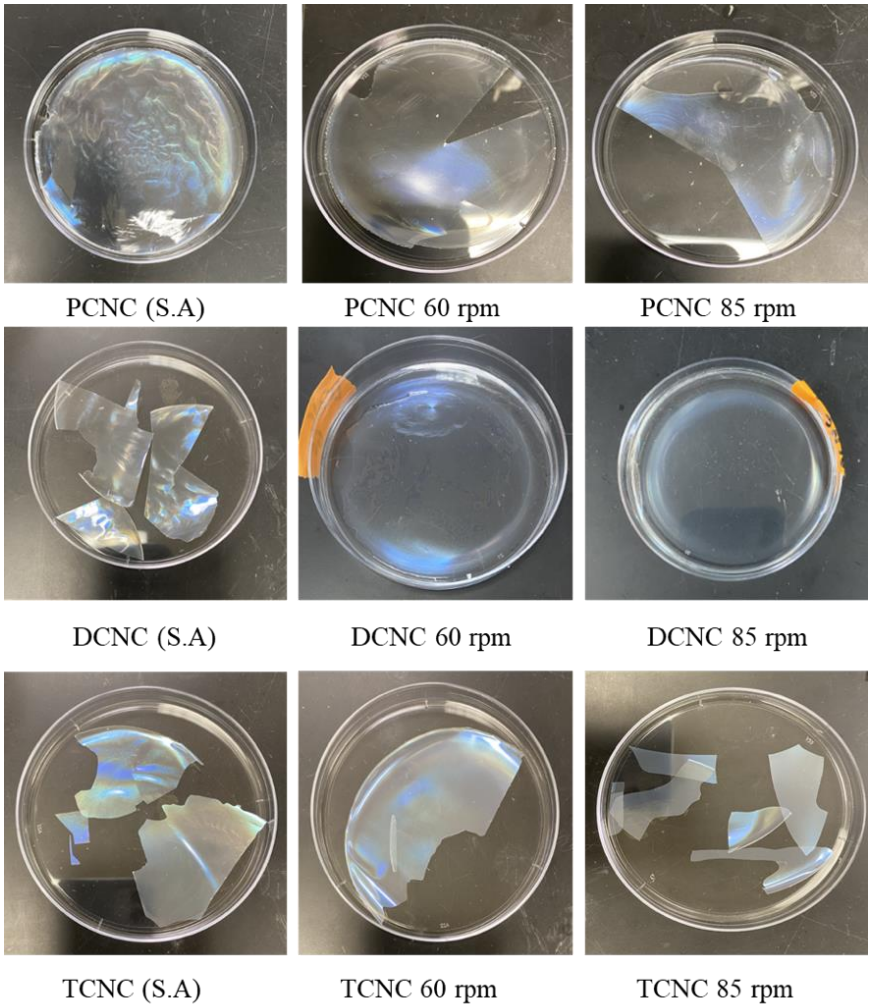

A Zeta sizer Nano ZS, Malvern instrument was used to measure zeta potential of pure CNC (PCNC), dialyzed CNC (DCNC) and TEMPO-CNC (TCNC), listed in the following **Table A**. The concentration used for the measurements is 0.83 wt%. An average value with standard deviation was reported by measuring a minimum of three readings.

Table A: Zeta potential of PCNC, DCNC and TCNC at 0.83 wt%

Sample	Avg. zeta potential, mV
Pure CNC (PCNC)	-49.60 ± 0.71
Dialyzed CNC (DCNC)	-50.83 ± 2.16
Tempo CNC (TCNC)	-47.00 ± 0.42

Cross-polarized microscopy was performed to capture transmitted light microscopic images to observe the birefringence property and orientation in the films. The images were taken at 0º and 45º to identify the CNC orientation in the film induced through orbital shaker or circular shear. To perform the microscopy, a triangular piece was cut from center towards the edge to observe CNC orientation at different locations of the film.

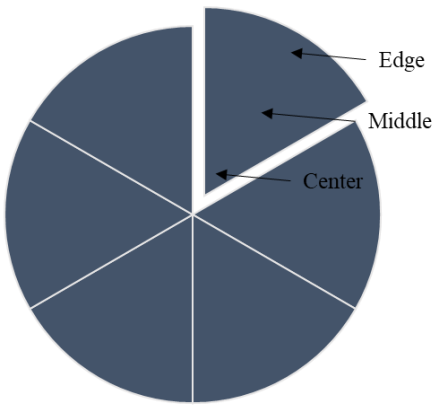

Further, the transmittance profile of the films was determined using a Thermo Scientific Genesys 10S UV−Vis spectrometer with a wavelength range of 200−800 nm. To quantitively evaluate

optical properties, a haze meter, Rhopoint ID-L A3100-001, was used to determine the transmittance, haze, clarity and sharpness of the films. An 8 mm spacer was used to take three measurements from different spots in a film to compute an average value and standard deviation. All the measurements were taken at room temperature and 50% RH condition.

The self-assembled pure CNC film, depicted in **Figure A** showed multicolored domains for all three positions. These small domains also indicate the non-uniformity of the resultant film, previously noticed as well [175–177]. The randomly localized formation of a helix in the film was generally observed for lower CNC concentration or from the isotropic phase [177]. For the entire regions of PCNC film, no signature digital color region was observed, thus the presence of any planar anchoring in the film could not be confirmed. In contrast, the application of 60 and 85 rpm provided more uniform birefringence and forms nematic domains as we observed distinctive contrast in intensity from 0º to 45º. We mostly observed a significant improvement in contrast at the edge of the film than at the center. Park et al. [177] noticed the absence of optical contrast in the center of the film and reported the formation of a vertical orientated helix or planar anchoring. However, the loss of selective reflection occurred at the edge where helix distortion took place, as reported by the author. Therefore, in this case, a reflective POM (Polarized light optical microscopy) study on the middle and center of the films could further elucidate the CNC arrangement.

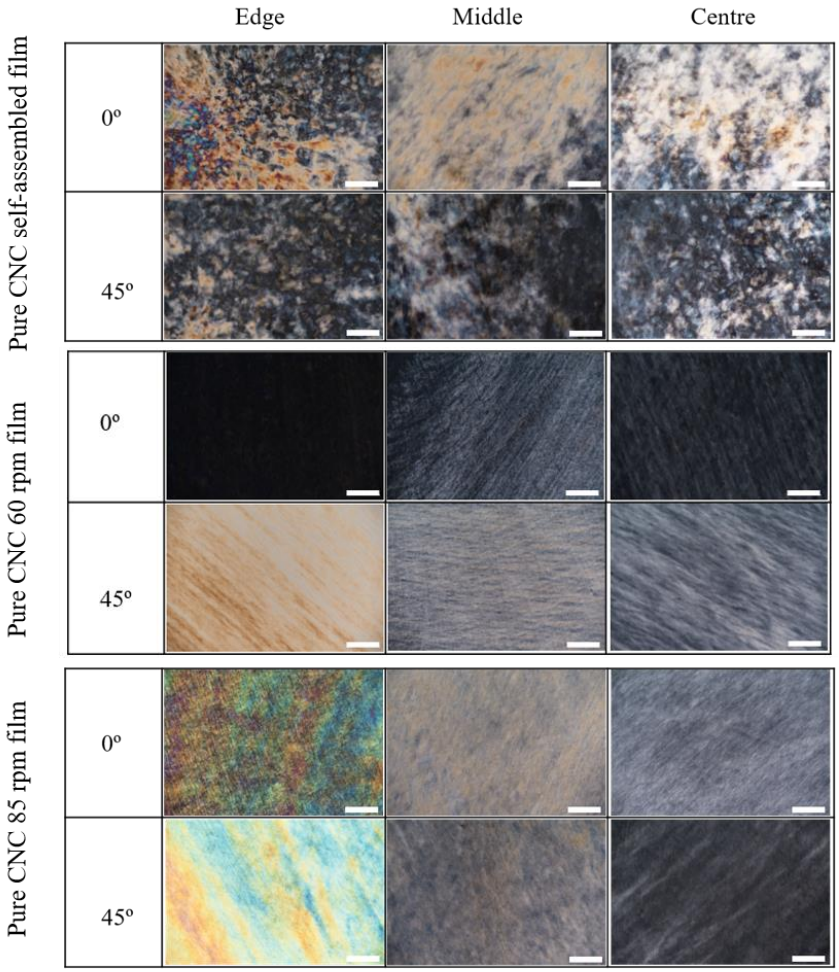

Figure A: Cross-polarized transmitted light microscopic images of pure CNC films; scale bar: 100 µm; resolution 20x

The transmittance profile, depicted in **Figure B(a)**, showed a blue shift in the transmittance peak minima with induced orbital shear with weakening transmittance peak minima. The self-assembled film showed a definitive peak minimum around ~ 300 nm which shifted to ~240 nm for 60 rpm thus shortening of pitch through orbital shear. The Bragg's formula clearly presents a direct correlation between the maximum reflection wavelength (λ_{max}) to the CNC pitch (P), therefore, an indirect correlation with minimum transmittance wavelength can be understood.

$$\lambda_{max=} n_{av} P \sin\theta$$

[n_{av} = average refractive index of CNC and θ = angle of incidence of light with respect to the surface of the film]

In addition to this, the weak transmittance peak at 85 rpm further indicates towards distorted chiral nematic structure. The similar distortion or unwinding of helix was also recorded by Park et al. [177] with increasing rotational speed. Moreover, a complete removal of transmittance minima was also reported previously for nematic CNC films by addition salt, modulation of pH or through shearing [8,102,107].

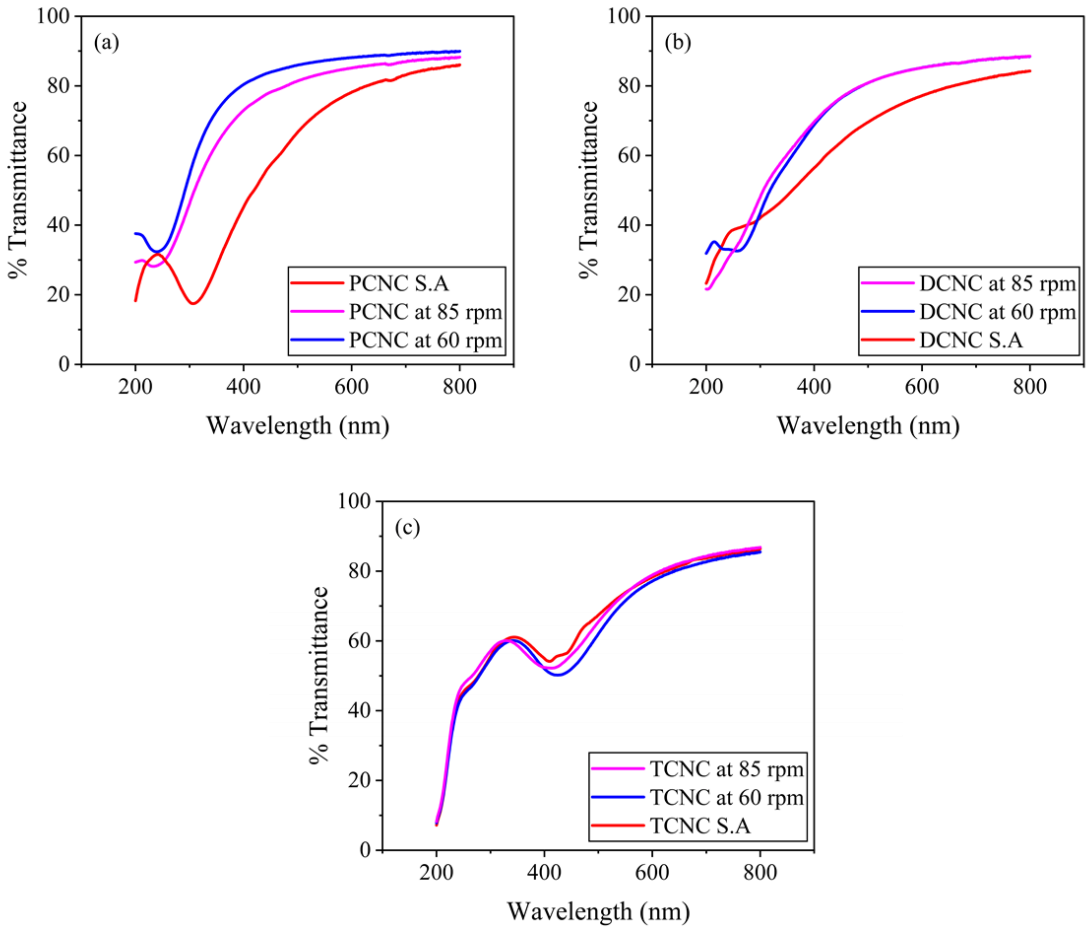

Figure B: Transmittance spectra of (a) pure CNC films (b) dialyzed CNC films (c) TEMPO-CNC films (S.A – self-assembled)

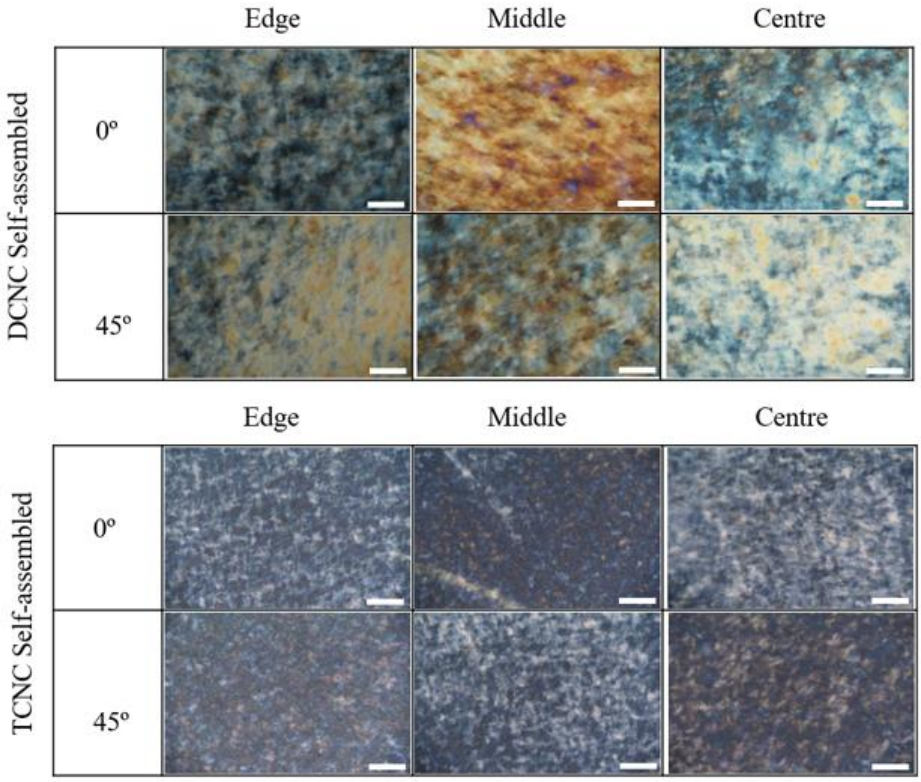

Figure C: Cross-polarized transmitted light microscopic images of dialyzed CNC (DCNC) films and tempo – CNC (TCNC) film; scale bar: 100 µm, resolution 20x

A contrasting behavior was noticed for dialyzed CNC (DCNC) films where non-uniformity and uniformity were both present in the self-assembled films, depicted in **Figure C**. Some areas of the film also showed intensity contrast, which also indicates the presence of some alignment in that region. We have noticed the presence of a distorted transmittance profile for DCNC self-assembled film, depicted in **Figure B(b)**., Dialysis mostly removes the residual salt and free acid molecules that are retained in the CNC as impurities [126]. The zeta potential after dialysis became more negative than the pure CNC dispersion, listed in **Table A**. Similar results were also reported by Parit et al. [8] where the author observed a more negative zeta potential with the disappearance of characteristic chiral nematic transmittance profile of dialyzed CNC film. An extensive dialysis

causes removal of counterions such as Na^+ and H^+ which are likely to cause an increase in effective diameter and dispersion phase boundaries. This increased repulsion due to loss of counterion, most likely influenced a distorted helix structure formation. In addition to this, CNC aspect ratio and impurities present in the batch can impact the results. Further, the application of 60 rpm showed improved alignment in the edge where intensity contrast was definitive with presence of intense birefringent color was also observed, however, the middle and center of the film lack any contrast and stage rotation did not result in color variation, and therefore cannot be claimed to have nematic structure (**Figure D**). There is a possibility of formation of planar anchoring in the middle and center of the film, however, further microscopic investigation is needed for confirmation. At 85 rpm a complete elimination of the transmittance peak was observed from **Figure B(b)**.

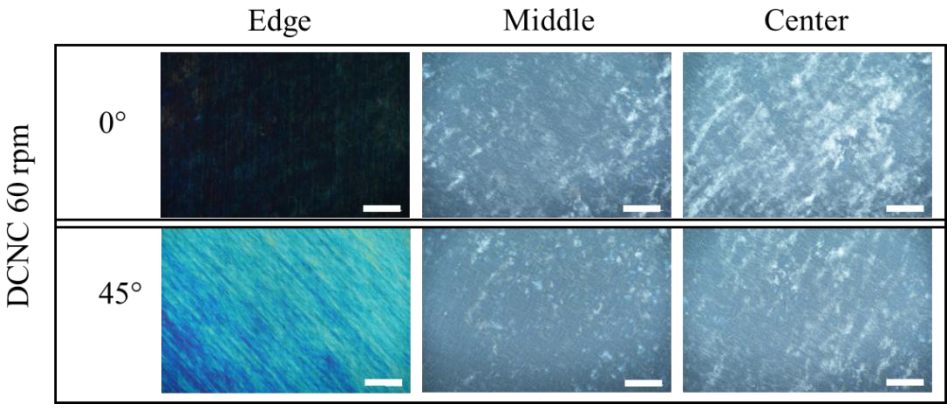

Figure D: Cross-polarized transmitted light microscopic images of dialyzed CNC (DCNC) film at 60 rpm; scale bar: 100 µm, resolution 20x

Similarly, TEMPO-CNC (TCNC) also showed formation of more aligned domains around the edge under orbital shaking, depicted in **Figure E**. Although the color contrast was present, compared to the PCNC and DCNC, TCNC showed less contrast in intensity at the edge. Like DCNC, at the center, TCNC at 85 rpm did not show color and intensity contrast with the stage rotation. Contrasting behavior from transmittance profile was also observed for TCNC depicted in

Figure B(c) where the blue shift was not observed for 60 rpm and a slight blue shift was located for 85 rpm. TCNC contains $COOH^-$ groups in the structure which are most likely to influence the behavior. Most likely, TCNC needs much higher rotation rates to exhibit similar patterns as PCNC and DCNC. However, with an orbital shaker, more uniformity was introduced in the film as observed through microscopic and digital images.

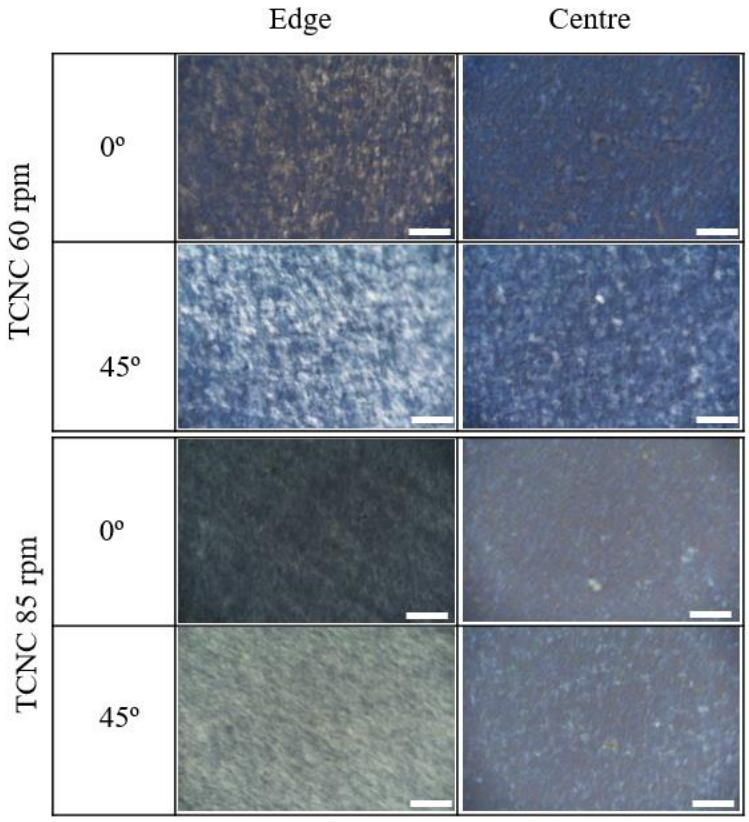

Figure E: Cross-polarized transmitted light microscopic images tempo – CNC (TCNC) film at 60 and 85 rpm; scale bar: 100 µm, resolution 20x

Quantitatively, the application of rotational motion through an orbital shaker improved the haze, clarity, and sharpness to a great extent. This is more visible for PCNC and DCNC where the haze reduced from ~ 9% to 5%, however, TCNC showed less sensitiveness. We observed haze to be reduced from ~ 11% to 9% in this case. Similarly, the sharpness only increased around ~ 80% whereas PCNC and DCNC showed improvement beyond 90%.

Self-assembled film property				
	Transmittance (%)	**Haze (%)**	**Clarity (%)**	**Sharpness (%)**
PCNC	82.48 ± 1.91	9.38 ± 1.81	87.38 ± 1.71	55.35 ± 4.44
DCNC	79.50 ± 4.10	9.27 ± 0.18	92.96 ± 1.94	72.08 ± 0.35
TCNC	77.35 ± 1.20	11.40 ± 1.00	88.31 ± 0.15	58.56 ± 6.70
60 rpm circular shear film property				
	Transmittance (%)	**Haze (%)**	**Clarity (%)**	**Sharpness (%)**
PCNC	89.00 ± 0.71	4.55 ± 0.25	97.18 ± 0.95	88.03 ± 3.80
DCNC	84.45 ± 1.06	6.11 ± 0.54	98.42 ± 0.06	93.21 ± 0.26
TCNC	81.60 ± 2.83	7.91 ± 1.20	95.49 ± 0.51	81.05 ± 1.93
85 rpm circular shear film property				
	Transmittance (%)	**Haze (%)**	**Clarity (%)**	**Sharpness (%)**
PCNC	86.50 ± 1.68	5.32 ± 1.13	98.00 ± 0.60	91.46 ± 2.58
DCNC	86.1	4.74	98.59	94.06
TCNC	77.8	9.02	94.84	78.5

Overall, optical properties were greatly improved with rotational shear through an orbital shaker. The CNCs counterion and functionality has a large impact on the haze, clarity, and sharpness of

the films as well. CNC alignment varies throughout the film, where mostly nematic domain formation is observed at the edge under rotational movement. The inner part of the films did not greatly show the nematic domain formation except the pure CNC. A few major points that can affect the final film properties are:

I. CNC source, counterion and functional group

II. Concentration of the dispersion

III. Rotational speed, ambient condition (humidity)

To deepen the fundamental understanding, further LCP (left-handed circular polarization) and RCP (right-handed circular polarization) microscopy would be useful for identifying if the planar anchoring was formed in the inner part of the film of DCNC and TCNC. Additionally, film formation from biphasic and liquid crystalline phases and its effect on the optical properties of the CNC film would be interesting to observe as well.

Chapter 6 Appendix A

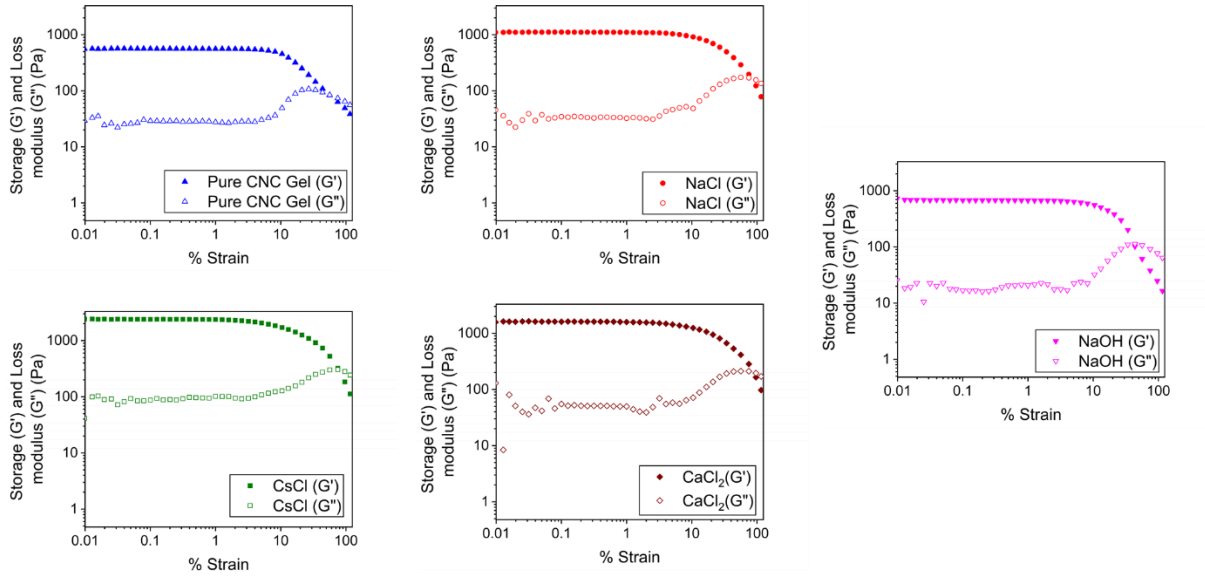

Figure 6.1 Strain Sweep

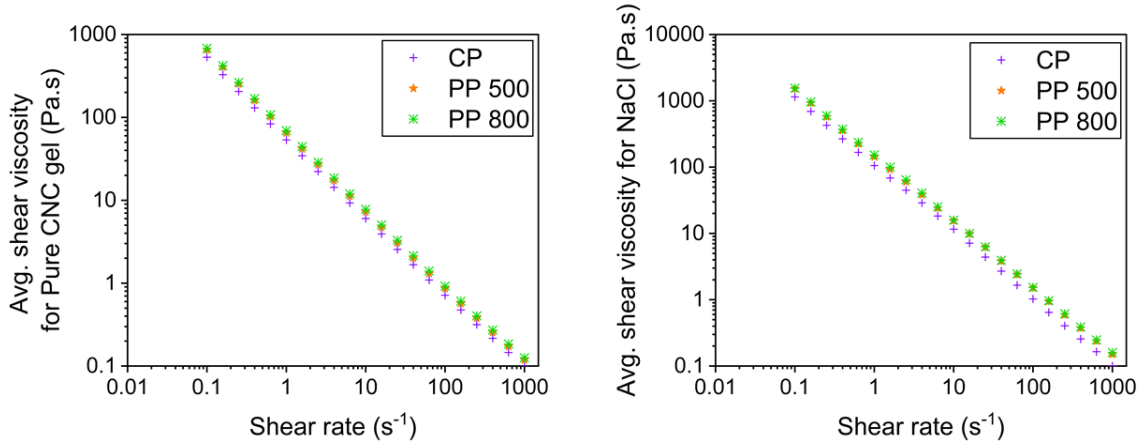

Figure 6.2 Slip Measurement (Parallel plate-PP, Cone and plate-CP, gap size for PP: 800 and 500µm)

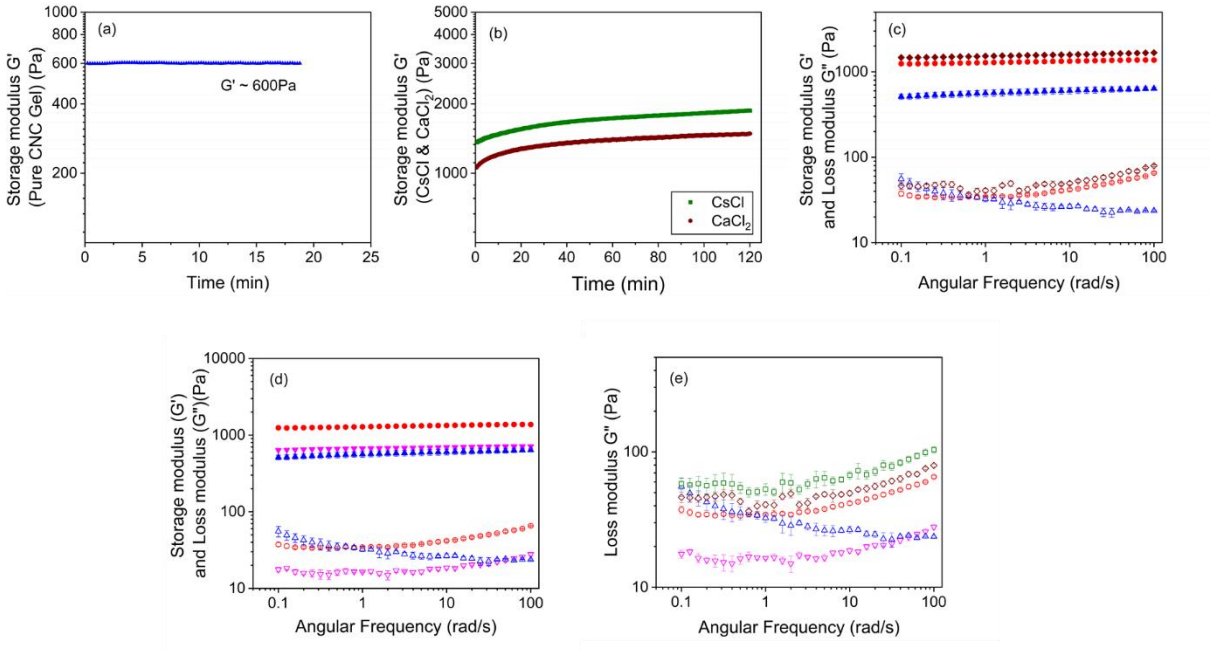

Figure 6.3 Time Sweep: (a) Pure CNC gel, (b) CsCl, $CaCl_2$; Frequency sweep: (c) valency, (d) pH and (e) all G″

Figure 6.4 Sample Image of NaOH (left) and NaCl (right) to Show the Effect of Ionization – The deprotonation caused NaOH added CNC to exhibit more fluidic behavior

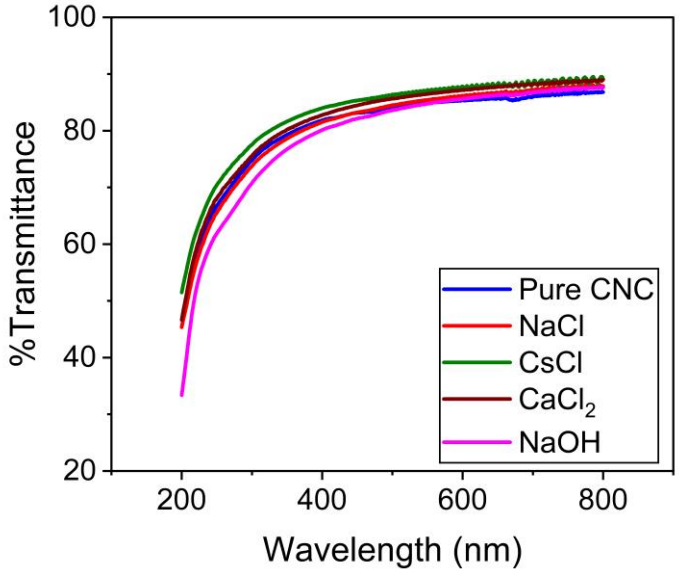

Figure 6.5 UV-Vis Spectroscopy of the all electrolyte contained film prepared at 100 s^{-1}

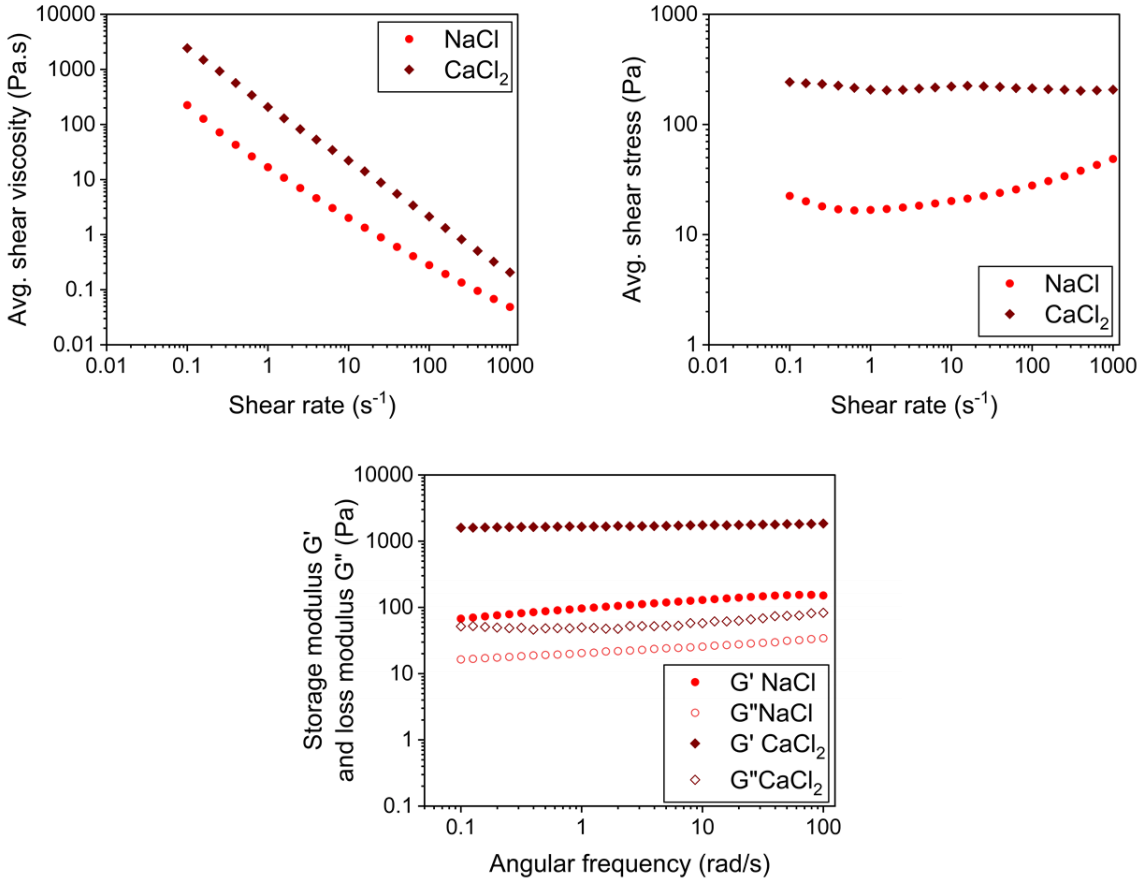

Figure 6.6 Transition Concentration Data Comparison (0.12mmol/g concentration used for both)

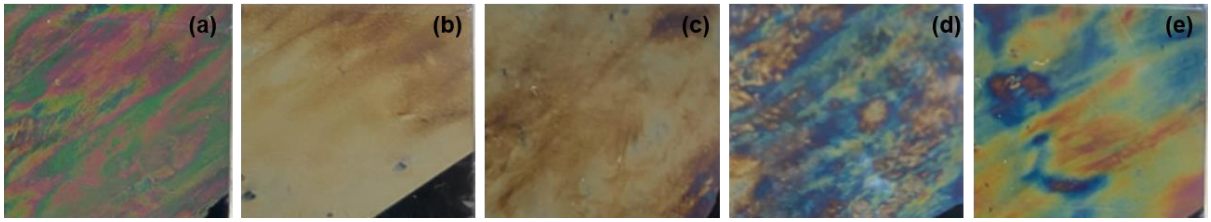

Figure 6.7 Overall Film Images at 20s-1 Shear Rate in Increased Dimension - (a) Pure CNC (b) NaCl (c) CsCl (d) CaCl2 and (e) NaOH (not on scale)

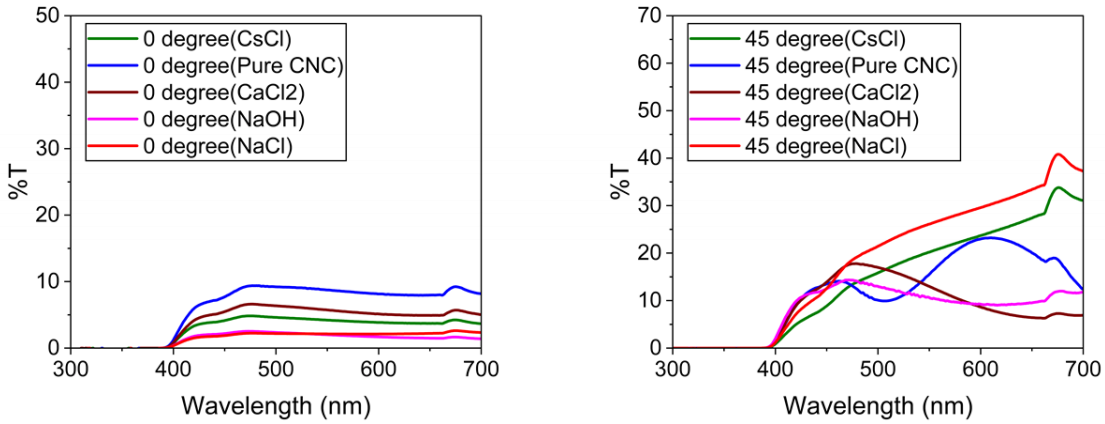

Figure 6.8 Cross-polarized transmission spectra at $20s^{-1}$ Shear Rate

Chapter 7 Appendix B

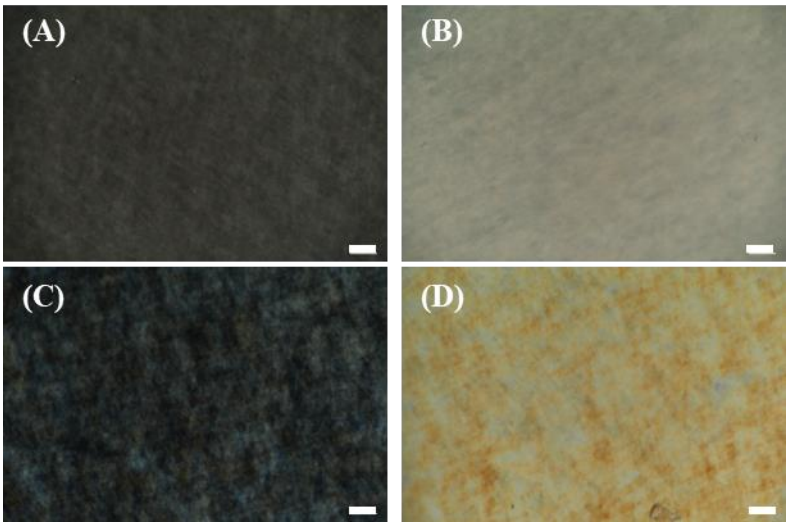

Figure 7.1 Cross-polarized images of PDCNC 1 and PDCNC 4 films: (A) PDCNC 1 at 0º (B) PDCNC 1 at 45º (C) PDCNC 4 at 0º (D) PDCNC 4 at 45º; Scale: 50 µm, Resolution: 20x

Table 7.1 Haze, transmittance, sharpness, clarity and waviness of the film

Sample	Transmittance %	Haze %	Sharpness %	Clarity %	Waviness (µm)
PCNC	83.73 ± 2.05	8.20 ± 1.34	58.11 ± 2.29	88.48 ± 0.80	15.72 ± 1.82
PDCNC1	85.70 ± 2.26	4.78 ± 1.36	96.03 ± 0.27	99.04 ± 0.06	2.43 ± 0.32
PDCNC4	87.25 ± 1.34	3.05 ± 0.83	92.42 ± 3.47	98.14 ± 0.91	6.00 ± 1.70

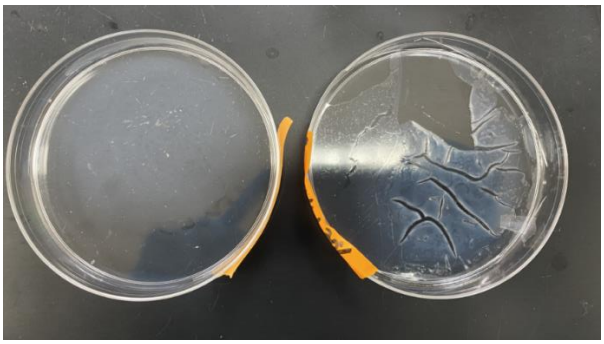

Figure 7.2 Left: PDCNC 4+20%PVA; Right: PDCNC 4+30%PVA

Table 7.2 Haze, transmittance, sharpness, clarity and waviness of the composite film

Sample	Transmittance	Haze	Sharpness	Clarity	Waviness
	%	%	%	%	(μm)
PCNC	83.73 ± 2.05	8.20 ± 1.34	58.11 ± 2.29	88.48 ± 0.80	15.72 ± 1.82
PCNC+10%PVA	84.07 ± 0.58	6.75 ± 0.23	42.52 ± 2.28	81.84 ± 1.10	27.33 ± 1.00
PCNC+20%PVA	78.33 ± 0.45	10.55 ± 1.42	29.01 ± 5.14	72.40 ± 4.42	49.04 ± 12.15
PCNC+30%PVA	77.97 ± 1.10	13.50 ± 0.64	25.38 ± 2.88	69.39 ± 3.52	71.67 ± 3.05
PDCNC4	87.25 ± 1.34	3.05 ± 0.83	92.42 ± 3.47	98.14 ± 0.91	6.00 ± 1.70
PDCNC4+10% PVA	86.47 ± 0.97	4.88 ± 0.89	85.42 ± 0.93	96.58 ± 0.21	6.56 ± 1.09
PDCNC4+20% PVA	84.90 ± 0.44	5.56 ± 0.53	70.61 ± 3.83	92.4 ± 1.27	19.05 ± 5.57

Chapter 8 Appendix C

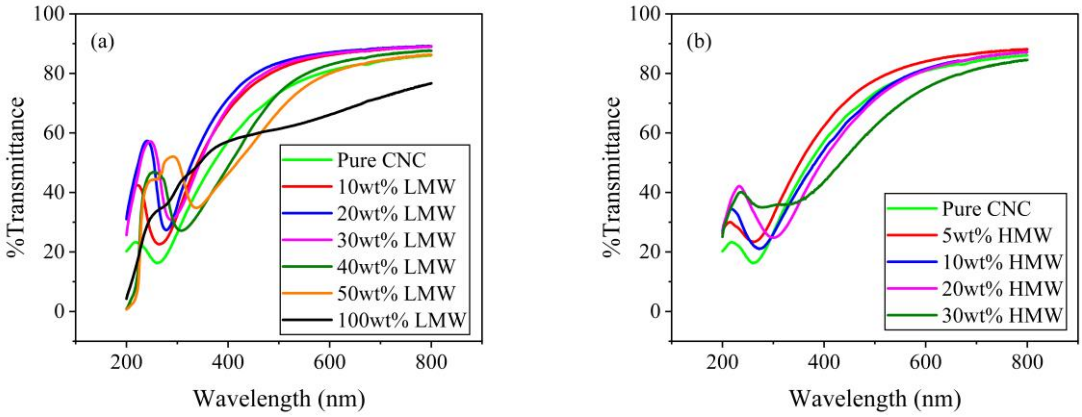

Figure 8.1 Effect of LMW and HMW on the transmittance spectra at 50% RH

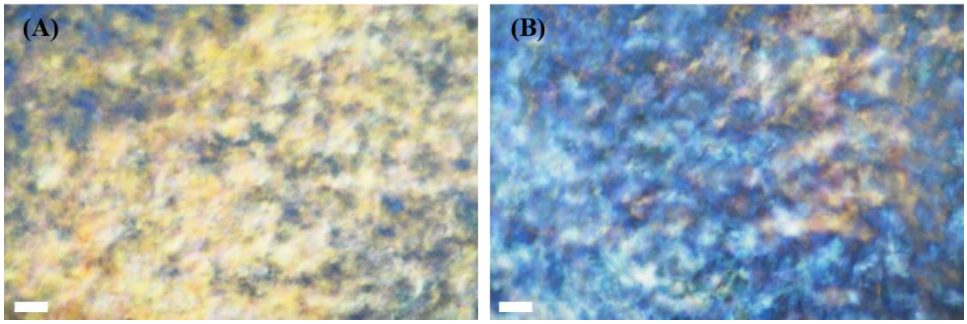

Figure 8.2 Cross polarized image of CNC – 80 wt% LLMW PVA (A) at 0º to the polarizer (B) at 45º to the polarizer; scale bar: 50 µm

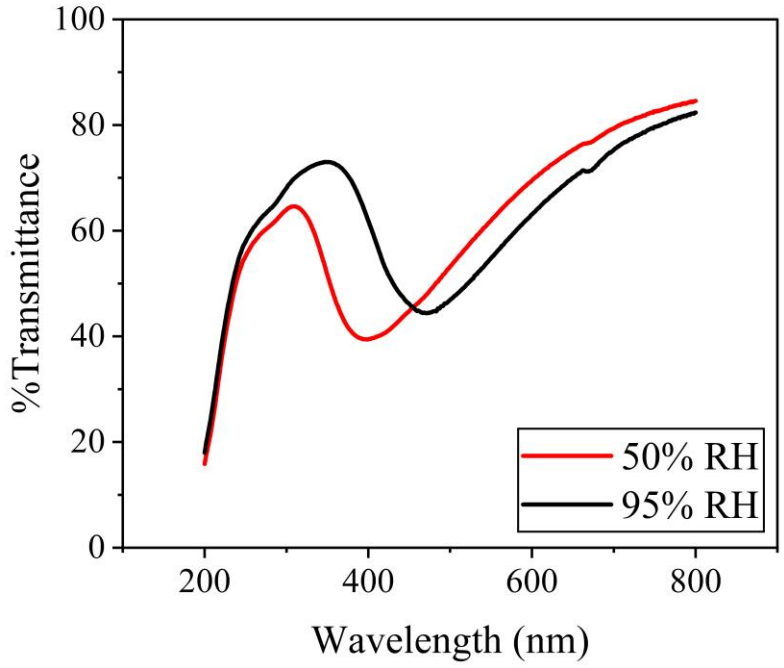

Figure 8.3 Transmission spectra of thermally crosslinked CNC-80%LLMW film at 50% RH and 95% RH

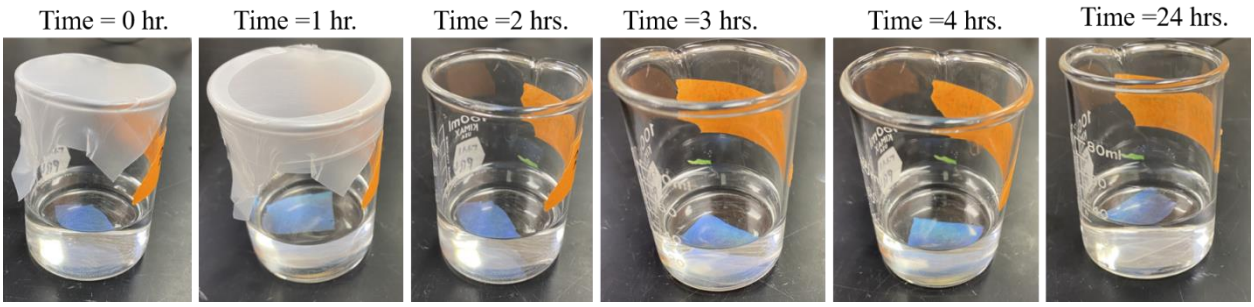

Figure 8.4 The Pure CNC – 40wt%LLMW PVA –composite film stability in pure ethanol (200 proof) demonstrated with varied time

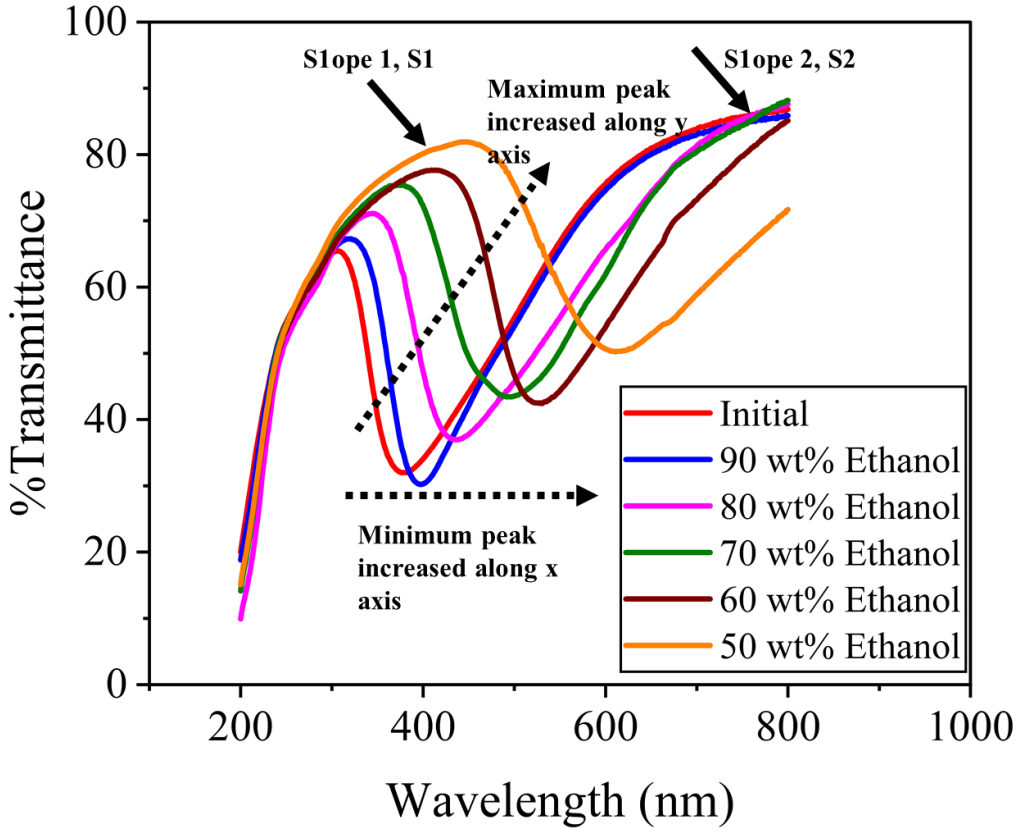

Figure 8.5 Three different ways to identify change in trasnmittacne profile for various ethanol-water solution

References

[1] K.W. Meereboer, M. Misra, A.K. Mohanty, Review of recent advances in the biodegradability of polyhydroxyalkanoate (PHA) bioplastics and their composites, Green Chemistry 22 (2020) 5519–5558.

[2] D.E. Henton, P. Gruber, J. Lunt, J. Randall, Polylactic acid technology, in: Natural Fibers, Biopolymers, and Biocomposites, CRC Press, 2005: pp. 559–607.

[3] N. Grishkewich, N. Mohammed, J. Tang, K.C. Tam, Recent advances in the application of cellulose nanocrystals, Curr Opin Colloid Interface Sci 29 (2017) 32–45.

[4] R. Moon, S. Beck, A. Rudie, Cellulose nanocrystals–A material with unique properties and many potential applications, Production and Applications of Cellulose Nanomaterials 9 (2013).

[5] O. Sabri, H. Van Doan, F. Malek, H. Bachouche, When is transparent packaging beneficial?, International Journal of Retail & Distribution Management 48 (2020) 781–801.

[6] R.A. Chowdhury, M. Nuruddin, C. Clarkson, F. Montes, J. Howarter, J.P. Youngblood, Cellulose nanocrystal (CNC) coatings with controlled anisotropy as high-performance gas barrier films, ACS Appl Mater Interfaces 11 (2018) 1376–1383.

[7] R.A. Chowdhury, S.X. Peng, J. Youngblood, Improved order parameter (alignment) determination in cellulose nanocrystal (CNC) films by a simple optical birefringence method, Cellulose 24 (2017) 1957–1970.

[8] M. Parit, Valorization of Lignocellulosic Materials-Designing, Synthesis, and Processing of Functional Polymer Nanocomposites., 2021.

[9] T. Abitbol, D. Kam, Y. Levi-Kalisman, D.G. Gray, O. Shoseyov, Surface charge influence on the phase separation and viscosity of cellulose nanocrystals, Langmuir 34 (2018) 3925–3933.

[10] A. Stroobants, H.N.W. Lekkerkerker, T. Odijk, Effect of electrostatic interaction on the liquid crystal phase transition in solutions of rodlike polyelectrolytes, Macromolecules 19 (1986) 2232–2238.

[11] J.H. Jordan, M.W. Easson, B.D. Condon, Alkali hydrolysis of sulfated cellulose nanocrystals: optimization of reaction conditions and tailored surface charge, Nanomaterials 9 (2019) 1232.

[12] J. Han, C. Zhou, Y. Wu, F. Liu, Q. Wu, Self-assembling behavior of cellulose nanoparticles during freeze-drying: effect of suspension concentration, particle size, crystal structure, and surface charge, Biomacromolecules 14 (2013) 1529–1540.

[13] N. Bumbudsanpharoke, S. Kwon, W. Lee, S. Ko, Optical response of photonic cellulose nanocrystal film for a novel humidity indicator, Int J Biol Macromol 140 (2019) 91–97.

[14] Y. Zhao, G. Gao, D. Liu, D. Tian, Y. Zhu, Y. Chang, Vapor sensing with color-tunable multilayered coatings of cellulose nanocrystals, Carbohydr Polym 174 (2017) 39–47.

[15] K. Yao, Q. Meng, V. Bulone, Q. Zhou, Flexible and responsive chiral nematic cellulose nanocrystal/poly (ethylene glycol) composite films with uniform and tunable structural color, Advanced Materials 29 (2017) 1701323.

[16] A. Kafy, A. Akther, M.I.R. Shishir, H.C. Kim, Y. Yun, J. Kim, Cellulose nanocrystal/graphene oxide composite film as humidity sensor, Sens Actuators A Phys 247 (2016) 221–226.

[17] K.W. Klockars, B.L. Tardy, M. Borghei, A. Tripathi, L.G. Greca, O.J. Rojas, Effect of anisotropy of cellulose nanocrystal suspensions on stratification, domain structure formation, and structural colors, Biomacromolecules 19 (2018) 2931–2943.

[18] J. George, S.N. Sabapathi, Cellulose nanocrystals: synthesis, functional properties, and applications, Nanotechnol Sci Appl (2015) 45–54.

[19] A. Karppinen, Rheology and flocculation of polymer-modified microfibrillated cellulose suspensions, (2014).

[20] Y. Habibi, L.A. Lucia, O.J. Rojas, Cellulose nanocrystals: chemistry, self-assembly, and applications, Chem Rev 110 (2010) 3479–3500.

[21] R.J. Moon, A. Martini, J. Nairn, J. Simonsen, J. Youngblood, Cellulose nanomaterials review: structure, properties and nanocomposites, Chem Soc Rev 40 (2011) 3941–3994.

[22] S. Beck-Candanedo, M. Roman, D.G. Gray, Effect of reaction conditions on the properties and behavior of wood cellulose nanocrystal suspensions, Biomacromolecules 6 (2005) 1048–1054.

[23] M.T. Postek, A. Vladar, J. Dagata, N. Farkas, B. Ming, R. Sabo, T.H. Wegner, J. Beecher, Cellulose nanocrystals the next big nano-thing?, in: Instrumentation, Metrology, and Standards for Nanomanufacturing II, SPIE, 2008: pp. 119–129.

[24] Y. Peng, D.J. Gardner, Y. Han, A. Kiziltas, Z. Cai, M.A. Tshabalala, Influence of drying method on the material properties of nanocellulose I: thermostability and crystallinity, Cellulose 20 (2013) 2379–2392.

[25] D. Bondeson, A. Mathew, K. Oksman, Optimization of the isolation of nanocrystals from microcrystalline cellulose by acid hydrolysis, Cellulose 13 (2006) 171–180.

[26] S. Elazzouzi-Hafraoui, Y. Nishiyama, J.-L. Putaux, L. Heux, F. Dubreuil, C. Rochas, The shape and size distribution of crystalline nanoparticles prepared by acid hydrolysis of native cellulose, Biomacromolecules 9 (2008) 57–65.

[27] R.H. Marchessault, F.F. Morehead, N.M. Walter, Liquid crystal systems from fibrillar polysaccharides, Nature 184 (1959) 632–633.

[28] J.P.F. Lagerwall, C. Schütz, M. Salajkova, J. Noh, J. Hyun Park, G. Scalia, L. Bergström, Cellulose nanocrystal-based materials: from liquid crystal self-assembly and glass formation to multifunctional thin films, NPG Asia Mater 6 (2014) e80–e80.

[29] X. Mu, D.G. Gray, Formation of chiral nematic films from cellulose nanocrystal suspensions is a two-stage process, Langmuir 30 (2014) 9256–9260.

[30] J.-F. Revol, L. Godbout, D.G. Gray, Solid self-assembled films of cellulose with chiral nematic order and optically variable properties, Journal of Pulp and Paper Science 24 (1998) 146–149.

[31] J.-F. Revol, H. Bradford, J. Giasson, R.H. Marchessault, D.G. Gray, Helicoidal self-ordering of cellulose microfibrils in aqueous suspension, Int J Biol Macromol 14 (1992) 170–172.

[32] X.M. Dong, T. Kimura, J.-F. Revol, D.G. Gray, Effects of ionic strength on the isotropic−chiral nematic phase transition of suspensions of cellulose crystallites, Langmuir 12 (1996) 2076–2082.

[33] W.J. Orts, L. Godbout, R.H. Marchessault, J.-F. Revol, Enhanced ordering of liquid crystalline suspensions of cellulose microfibrils: a small angle neutron scattering study, Macromolecules 31 (1998) 5717–5725.

[34] C. Schutz, M. Agthe, A.B. Fall, K. Gordeyeva, V. Guccini, M. Salajková, T.S. Plivelic, J.P.F. Lagerwall, G. Salazar-Alvarez, L. Bergstrom, Rod packing in chiral nematic cellulose nanocrystal dispersions studied by small-angle X-ray scattering and laser diffraction, Langmuir 31 (2015) 6507–6513.

[35] R.M. Parker, G. Guidetti, C.A. Williams, T. Zhao, A. Narkevicius, S. Vignolini, B. Frka-Petesic, The self-assembly of cellulose nanocrystals: Hierarchical design of visual appearance, Advanced Materials 30 (2018) 1704477.

[36] S. Beck, J. Bouchard, G. Chauve, R. Berry, Controlled production of patterns in iridescent solid films of cellulose nanocrystals, Cellulose 20 (2013) 1401–1411.

[37] H. Xie, H. Du, X. Yang, C. Si, Recent strategies in preparation of cellulose nanocrystals and cellulose nanofibrils derived from raw cellulose materials, Int J Polym Sci 2018 (2018).

[38] B.G. Rånby, A. Banderet, L.G. Sillén, Aqueous Colloidal Solutions of Cellulose Micelles., Acta Chem Scand 3 (1949) 649–650.

[39] S.M. Mukherjee, H.J. Woods, X-ray and electron microscope studies of the degradation of cellulose by sulphuric acid, Biochim Biophys Acta 10 (1953) 499–511.

[40] R.S. Reiner, A.W. Rudie, Process scale-up of cellulose nanocrystal production to 25 kg per batch at the forest products laboratory, In: Production and Applications of Cellulose Nanomaterials, TAPPI Press, Chapter 1.1, 2013; Pp. 21-24. 1 (2013) 21–24.

[41] H. Yu, Z. Qin, B. Liang, N. Liu, Z. Zhou, L. Chen, Facile extraction of thermally stable cellulose nanocrystals with a high yield of 93% through hydrochloric acid hydrolysis under hydrothermal conditions, J Mater Chem A Mater 1 (2013) 3938–3944.

[42] S. Camarero Espinosa, T. Kuhnt, E.J. Foster, C. Weder, Isolation of thermally stable cellulose nanocrystals by phosphoric acid hydrolysis, Biomacromolecules 14 (2013) 1223–1230.

[43] N. Wang, E. Ding, R. Cheng, Preparation and liquid crystalline properties of spherical cellulose nanocrystals, Langmuir 24 (2008) 5–8.

[44] W. Li, J. Yue, S. Liu, Preparation of nanocrystalline cellulose via ultrasound and its reinforcement capability for poly (vinyl alcohol) composites, Ultrason Sonochem 19 (2012) 479–485.

[45] B.S.L. Brito, F. V Pereira, J.-L. Putaux, B. Jean, Preparation, morphology and structure of cellulose nanocrystals from bamboo fibers, Cellulose 19 (2012) 1527–1536.

[46] N.F. Vasconcelos, J.P.A. Feitosa, F.M.P. da Gama, J.P.S. Morais, F.K. Andrade, M. de S.M. de Souza, M. de Freitas Rosa, Bacterial cellulose nanocrystals produced under

different hydrolysis conditions: Properties and morphological features, Carbohydr Polym 155 (2017) 425–431.

[47] V.F. Korolovych, V. Cherpak, D. Nepal, A. Ng, N.R. Shaikh, A. Grant, R. Xiong, T.J. Bunning, V. V Tsukruk, Cellulose nanocrystals with different morphologies and chiral properties, Polymer (Guildf) 145 (2018) 334–347.

[48] R. Mu, X. Hong, Y. Ni, Y. Li, J. Pang, Q. Wang, J. Xiao, Y. Zheng, Recent trends and applications of cellulose nanocrystals in food industry, Trends Food Sci Technol 93 (2019) 136–144.

[49] S. Xie, X. Zhang, M.P. Walcott, H. Lin, Applications of cellulose nanocrystals: a review, Engineered Science 2 (2018) 4–16.

[50] J. Shojaeiarani, D.S. Bajwa, N.M. Stark, S.G. Bajwa, Rheological properties of cellulose nanocrystals engineered polylactic acid nanocomposites, Compos B Eng 161 (2019) 483–489.

[51] M. Nuruddin, R.A. Chowdhury, R. Szeto, J.A. Howarter, K.A. Erk, C.R. Szczepanski, J.P. Youngblood, Structure–property relationship of cellulose nanocrystal–polyvinyl alcohol thin films for high barrier coating applications, ACS Appl Mater Interfaces 13 (2021) 12472–12482.

[52] J. Goswami, E. Haque, D.M. Fox, J.W. Gilman, G.A. Holmes, R.J. Moon, K. Kalaitzidou, The effect of cellulose nanocrystal coatings on the glass fiber–epoxy interphase, Materials 12 (2019) 1951.

[53] J. He, K. Bian, N. Li, G. Piao, Volatile acid responsiveness of chiral nematic luminescent cellulose nanocrystal/9, 10-Bis ((Z)-2-phenyl-2-(pyridin-2-yl) vinyl) anthracene composite films, ACS Sustain Chem Eng 7 (2019) 12369–12375.

[54] J.A. Kelly, A.M. Shukaliak, C.C.Y. Cheung, K.E. Shopsowitz, W.Y. Hamad, M.J. MacLachlan, Responsive photonic hydrogels based on nanocrystalline cellulose, Angewandte Chemie 34 (2013) 9080–9084.

[55] Y. Gao, Z. Jin, Iridescent chiral nematic cellulose nanocrystal/polyvinylpyrrolidone nanocomposite films for distinguishing similar organic solvents, ACS Sustain Chem Eng 6 (2018) 6192–6202.

[56] K.B.R. Teodoro, F.L. Migliorini, W.A. Christinelli, D.S. Correa, Detection of hydrogen peroxide (H2O2) using a colorimetric sensor based on cellulose nanowhiskers and silver nanoparticles, Carbohydr Polym 212 (2019) 235–241.

[57] W. Song, J.-K. Lee, M.S. Gong, K. Heo, W.-J. Chung, B.Y. Lee, Cellulose nanocrystal-based colored thin films for colorimetric detection of aldehyde gases, ACS Appl Mater Interfaces 10 (2018) 10353–10361.

[58] S. Tuukkanen, S. Rajala, Nanocellulose as a piezoelectric material, Piezoelectricity—Organic and Inorganic Materials and Applications (2018) 1–14.

[59] E. Fukada, Piezoelectricity of wood, J Physical Soc Japan 10 (1955) 149–154.

[60] X. Yang, K. Shi, I. Zhitomirsky, E.D. Cranston, Cellulose Nanocrystal Aerogels as Universal 3D Lightweight Substrates for Supercapacitor Materials., Adv Mater 27 (2015) 6104–6109.

[61] E. Fukada, Piezoelectricity as a fundamental property of wood, Wood Sci Technol 2 (1968) 299–307.

[62] R.J. Ross, J. Kan, X. Wang, J. Blankenburg, J.I. Stockhausen, R.F. Pellerin, Wood and Wood-based Materials as Sensors-a Review of the Piezoelectric Effect in Wood, (2012).

[63] L. Csoka, I.C. Hoeger, O.J. Rojas, I. Peszlen, J.J. Pawlak, P.N. Peralta, Piezoelectric effect of cellulose nanocrystals thin films, ACS Macro Lett 1 (2012) 867–870.

[64] J.P.F. Lagerwall, G. Scalia, A new era for liquid crystal research: Applications of liquid crystals in soft matter nano-, bio-and microtechnology, Current Applied Physics 12 (2012) 1387–1412.

[65] F. Hamade, S.K. Amit, M.B. Woods, V.A. Davis, The effects of size and shape dispersity on the phase behavior of nanomesogen lyotropic liquid crystals, Crystals (Basel) 10 (2020) 715.

[66] K. Hiltrop, Lyotropic liquid crystals, in: Liq Cryst, Springer, 1994: pp. 143–171.

[67] G.W., Gray, Introduction and Historical Development in HandBook of Liquid Crystals., 1998.

[68] V.A. Davis, Liquid crystalline assembly of nanocylinders, J Mater Res 26 (2011) 140–153.

[69] P. Saha, Optimization of cellulose nanocrystal films for optical and micromechanical applications., Auburn University, 2018.

[70] C. Li, J. Evans, N. Wang, T. Guo, S. He, pH dependence of the chirality of nematic cellulose nanocrystals, Sci Rep 9 (2019) 11290.

[71] V.A. Davis, L.M. Ericson, A.N.G. Parra-Vasquez, H. Fan, Y. Wang, V. Prieto, J.A. Longoria, S. Ramesh, R.K. Saini, C. Kittrell, Phase behavior and rheology of SWNTs in superacids, Macromolecules 37 (2004) 154–160.

[72] E.E. Ureña-Benavides, G. Ao, V.A. Davis, C.L. Kitchens, Rheology and phase behavior of lyotropic cellulose nanocrystal suspensions, Macromolecules 44 (2011) 8990–8998.

[73] X.M. Dong, D.G. Gray, Effect of counterions on ordered phase formation in suspensions of charged rodlike cellulose crystallites, Langmuir 13 (1997) 2404–2409.

[74] C. Honorato-Rios, A. Kuhnhold, J.R. Bruckner, R. Dannert, T. Schilling, J.P.F. Lagerwall, Equilibrium liquid crystal phase diagrams and detection of kinetic arrest in cellulose nanocrystal suspensions, Front Mater 3 (2016) 21.

[75] A.D. Haywood, K.M. Weigandt, P. Saha, M. Noor, M.J. Green, V.A. Davis, New insights into the flow and microstructural relaxation behavior of biphasic cellulose nanocrystal dispersions from RheoSANS, Soft Matter 13 (2017) 8451–8462.

[76] S. Shafiei-Sabet, W.Y. Hamad, S.G. Hatzikiriakos, Rheology of nanocrystalline cellulose aqueous suspensions, Langmuir 28 (2012) 17124–17133.

[77] A.D. Haywood, V.A. Davis, Effects of liquid crystalline and shear alignment on the optical properties of cellulose nanocrystal films, Cellulose 24 (2017) 705–716.

[78] S. Onogi, T. Asada, Rheology and rheo-optics of polymer liquid crystals, in: Rheology: Volume 1: Principles, Springer, 1980: pp. 127–147.

[79] R.G. Larson, The structure and rheology of complex fluids, Oxford university press New York, 1999.

[80] J. Li, J.F. Revol, R.H. Marchessault, Rheological properties of aqueous suspensions of chitin crystallites, J Colloid Interface Sci 183 (1996) 365–373.

[81] S. Shafiei-Sabet, W.Y. Hamad, S.G. Hatzikiriakos, Ionic strength effects on the microstructure and shear rheology of cellulose nanocrystal suspensions, Cellulose 21 (2014) 3347–3359.

[82] J. Pan, W. Hamad, S.K. Straus, Parameters affecting the chiral nematic phase of nanocrystalline cellulose films, Macromolecules 43 (2010) 3851–3858.

[83] M. Bercea, P. Navard, Shear dynamics of aqueous suspensions of cellulose whiskers, Macromolecules 33 (2000) 6011–6016.

[84] Z. Yu, K. Wang, X. Lu, Flexible cellulose nanocrystal-based bionanocomposite film as a smart photonic material responsive to humidity, Int J Biol Macromol 188 (2021) 385–390.

[85] J. Pan, W. Hamad, S.K. Straus, Parameters affecting the chiral nematic phase of nanocrystalline cellulose films, Macromolecules 43 (2010) 3851–3858.

[86] A.B. Reising, R.J. Moon, J.P. Youngblood, Effect of particle alignment on mechanical properties of neat cellulose nanocrystal films, J Sci Technol For Prod Process 2 (2012) 32–41.

[87] S. Peng, Q. Luo, G. Zhou, X. Xu, Recent advances on cellulose nanocrystals and their derivatives, Polymers (Basel) 13 (2021) 3247.

[88] K. Song, X. Zhu, W. Zhu, X. Li, Preparation and characterization of cellulose nanocrystal extracted from Calotropis procera biomass, Bioresour Bioprocess 6 (2019) 1–8.

[89] D. Trache, A.F. Tarchoun, M. Derradji, T.S. Hamidon, N. Masruchin, N. Brosse, M.H. Hussin, Nanocellulose: from fundamentals to advanced applications, Front Chem 8 (2020) 392.

[90] F. Chen, C. Chi, Development of pullulan/carboxylated cellulose nanocrystal/tea polyphenol bionanocomposite films for active food packaging, Int J Biol Macromol 186 (2021) 405–413.

[91] B. An, M. Xu, J. Sun, W. Sun, Y. Miao, C. Ma, S. Luo, J. Li, W. Li, S. Liu, Cellulose nanocrystals-based bio-composite optical materials for reversible colorimetric responsive films and coatings, Int J Biol Macromol 233 (2023) 123600.

[92] E.J. Foster, R.J. Moon, U.P. Agarwal, M.J. Bortner, J. Bras, S. Camarero-Espinosa, K.J. Chan, M.J.D. Clift, E.D. Cranston, S.J. Eichhorn, Current characterization methods for cellulose nanomaterials, Chem Soc Rev 47 (2018) 2609–2679.

[93] A.A. Moud, A.A. Moud, Flow and assembly of cellulose nanocrystals (CNC): A bottom-up perspective-A review, Int J Biol Macromol (2023) 123391.

[94] D.G. Gray, Recent advances in chiral nematic structure and iridescent color of cellulose nanocrystal films, Nanomaterials 6 (2016) 213.

[95] J. Araki, S. Kuga, Effect of trace electrolyte on liquid crystal type of cellulose microcrystals, Langmuir 17 (2001) 4493–4496.

[96] X.M. Dong, T. Kimura, J.-F. Revol, D.G. Gray, Effects of ionic strength on the isotropic−chiral nematic phase transition of suspensions of cellulose crystallites, Langmuir 12 (1996) 2076–2082.

[97] R. Kádár, S. Spirk, T. Nypelo, Cellulose nanocrystal liquid crystal phases: Progress and challenges in characterization using rheology coupled to optics, scattering, and spectroscopy, ACS Nano 15 (2021) 7931–7945.

[98] Y. Qin, R. Chang, S. Ge, L. Xiong, Q. Sun, Synergistic effect of glycerol and ionic strength on the rheological behavior of cellulose nanocrystals suspension system, Int J Biol Macromol 102 (2017) 1073–1082.

[99] J. Wang, C. Carlos, Z. Zhang, J. Li, Y. Long, F. Yang, Y. Dong, X. Qiu, Y. Qian, X. Wang, Piezoelectric nanocellulose thin film with large-scale vertical crystal alignment, ACS Appl Mater Interfaces 12 (2020) 26399–26404.

[100] X. Ding, J. Liu, T.A.L. Harris, A review of the operating limits in slot die coating processes, AIChE Journal 62 (2016) 2508–2524.

[101] H. Lv, K. Yang, J. You, S. Wang, Operational Stability Analysis on the Roller-Coating Process for a Roll Coating-Simulation Test Equipment, Machines 10 (2022) 304.

[102] M. Parit, P. Saha, V.A. Davis, Z. Jiang, Transparent and homogenous cellulose nanocrystal/lignin UV-protection films, ACS Omega 3 (2018) 10679–10691.

[103] D.G. Gray, X. Mu, Chiral nematic structure of cellulose nanocrystal suspensions and films; polarized light and atomic force microscopy, Materials 8 (2015) 7873–7888.

[104] J. Fernández-Santos, C. Valls, O. Cusola, M.B. Roncero, Improving filmogenic and barrier properties of nanocellulose films by addition of biodegradable plasticizers, ACS Sustain Chem Eng 9 (2021) 9647–9660.

[105] F. Nan, S. Nagarajan, Y. Chen, P. Liu, Y. Duan, Y. Men, J. Zhang, Enhanced toughness and thermal stability of cellulose nanocrystal iridescent films by alkali treatment, ACS Sustain Chem Eng 5 (2017) 8951–8958.

[106] C. Browne, V.S. Raghuwanshi, G. Garnier, W. Batchelor, Modulating the chiral nematic structure of cellulose nanocrystal suspensions with electrolytes, J Colloid Interface Sci 650 (2023) 1064–1072.

[107] M. Parit, Z. Jiang, Cellulose nanocrystal films: effect of electrolyte and lignin addition on self-assembly, optical, and mechanical properties, Cellulose 30 (2023) 9405–9423.

[108] T. Phan-Xuan, A. Thuresson, M. Skepö, A. Labrador, R. Bordes, A. Matic, Aggregation behavior of aqueous cellulose nanocrystals: the effect of inorganic salts, Cellulose 23 (2016) 3653–3663.

[109] G. Lenfant, M.-C. Heuzey, T.G.M. van de Ven, P.J. Carreau, A comparative study of ECNC and CNC suspensions: effect of salt on rheological properties, Rheol Acta 56 (2017) 51–62.

[110] K. Nyamayaro, P. Mehrkhodavandi, S.G. Hatzikiriakos, Impact of counterion valency on the rheology of sulfonated cellulose nanocrystal hydrogels, Carbohydr Polym 302 (2023) 120378.

[111] D. Bukharina, M. Kim, M.J. Han, V. V Tsukruk, Cellulose nanocrystals' assembly under ionic strength variation: from high orientation ordering to a random orientation, Langmuir 38 (2022) 6363–6375.

[112] W. Qi, J. Yu, Z. Zhang, H.-N. Xu, Effect of pH on the aggregation behavior of cellulose nanocrystals in aqueous medium, Mater Res Express 6 (2019) 125078.

[113] M. Danesh, D. Mauran, S. Hojabr, R. Berry, M. Pawlik, S.G. Hatzikiriakos, Yielding of cellulose nanocrystal suspensions in the presence of electrolytes, Physics of Fluids 32 (2020).

[114] A. Hirai, O. Inui, F. Horii, M. Tsuji, Phase separation behavior in aqueous suspensions of bacterial cellulose nanocrystals prepared by sulfuric acid treatment, Langmuir 25 (2009) 497–502.

[115] C. Schütz, J. Van Rie, S. Eyley, A. Gençer, H. Van Gorp, S. Rosenfeldt, K. Kang, W. Thielemans, Effect of source on the properties and behavior of cellulose nanocrystal suspensions, ACS Sustain Chem Eng 6 (2018) 8317–8324.

[116] J. Shojaeiarani, D.S. Bajwa, S. Chanda, Cellulose nanocrystal based composites: A review, Composites Part C: Open Access 5 (2021) 100164.

[117] L. Bai, Z. Wang, Y. He, F. Song, X. Wang, Y. Wang, Flexible photonic cellulose nanocrystal films as a platform with multisensing functions, ACS Sustain Chem Eng 8 (2020) 18484–18491.

[118] Y. Ji, D.E. Shen, Y. Lu, G.T. Schueneman, M.L. Shofner, J.C. Meredith, Aqueous-Based Recycling of Cellulose Nanocrystal/Chitin Nanowhisker Barrier Coatings, ACS Sustain Chem Eng 11 (2023) 10874–10883.

[119] E.E. Jaekel, S. Kluge, S. Tröger-Müller, M. Tutuş, S. Filonenko, Tunable Gas Permeation Behavior in Self-Standing Cellulose Nanocrystal-Based Membranes, ACS Sustain Chem Eng 10 (2022) 12895–12905.

[120] K. Feng, X. Gao, Z. Gu, Z. Jin, Improving homogeneity of iridescent cellulose nanocrystal films by surfactant-assisted spreading self-assembly, ACS Sustain Chem Eng 7 (2019) 19062–19071.

[121] S. Beck, J. Bouchard, Auto-catalyzed acidic desulfation of cellulose nanocrystals, Nord Pulp Paper Res J 29 (2014) 6–14.

[122] C. Pires, B.M. Régnier, M.J.R. dos Santos, R.A. de Freitas, Effect of sulfate-ester content and nanocellulose allomorph on stability of amylopectin-xyloglucan water-in-water emulsions, Food Hydrocoll 141 (2023) 108700.

[123] I.E. Imiete, L. Giannini, L. Tadiello, M. Orlandi, L. Zoia, The effect of sulfate half-ester groups on the mechanical performance of cellulose nanocrystal-natural rubber composites, Cellulose 30 (2023) 8929–8940.

[124] S. Wojno, A. Ahlinder, A. Altskär, M. Stading, T. Abitbol, R. Kádár, Percolation and phase behavior in cellulose nanocrystal suspensions from nonlinear rheological analysis, Carbohydr Polym 308 (2023) 120622.

[125] S. Llàcer Navarro, K. Nakayama, A. Idström, L. Evenäs, A. Ström, T. Nypelö, The effect of sulfate half-ester groups on cellulose nanocrystal periodate oxidation, Cellulose 28 (2021) 9633–9644.

[126] M. Banerjee, S. Saraswatula, A. Williams, B. Brettmann, Effect of purification methods on commercially available cellulose nanocrystal properties and TEMPO Oxidation, Processes 8 (2020) 698.

[127] M.S. Reid, S.A. Kedzior, M. Villalobos, E.D. Cranston, Effect of ionic strength and surface charge density on the kinetics of cellulose nanocrystal thin film swelling, Langmuir 33 (2017) 7403–7411.

[128] A. Kumar, Y.S. Negi, V. Choudhary, N.K. Bhardwaj, Characterization of cellulose nanocrystals produced by acid-hydrolysis from sugarcane bagasse as agro-waste, J. Mater. Phys. Chem 2 (2014) 1–8.

[129] C. Driemeier, F.M. Mendes, B.S. Santucci, M.T.B. Pimenta, Cellulose co-crystallization and related phenomena occurring in hydrothermal treatment of sugarcane bagasse, Cellulose 22 (2015) 2183–2195.

[130] M.A. Ibrahim, A. Salama, F. Zahran, M.S. Abdelfattah, A. Al-Salme, M. Bechelany, A. Barhoum, Fabrication of cellulose nanocrystals/carboxymethyl cellulose/zeolite membranes for methylene blue dye removal: understanding factors, adsorption kinetics, and thermodynamic isotherms, Front Chem 12 (2024) 1330810.

[131] Z. Hanif, D. Choi, M.Z. Tariq, M. La, S.J. Park, Water-stable flexible nanocellulose chiral nematic films through acid vapor cross-linked glutaraldehyde for chiral nematic templating, ACS Macro Lett 9 (2020) 146–151.

[132] V. Calvo, M.A. Álvarez Sánchez, L. Güemes, C. Martinez-Baron, S. Baúlde, A. Criado, J.M. Gonzalez-Dominguez, W.K. Maser, A.M. Benito, Preparation of cellulose

nanocrystals: controlling the crystalline type by one-pot acid hydrolysis, ACS Macro Lett 12 (2023) 152–158.

[133] Y. Dong, C. Rossner, A. Fery, Design Strategies for Creating Cellulose-Based Nanomaterials with Tailored Optical Functionality, ACS Applied Optical Materials 1 (2023) 1862–1878.

[134] A.E. Way, L. Hsu, K. Shanmuganathan, C. Weder, S.J. Rowan, pH-responsive cellulose nanocrystal gels and nanocomposites, ACS Macro Lett 1 (2012) 1001–1006.

[135] L. Morlet-Decarnin, T. Divoux, S. Manneville, Critical-like gelation dynamics in cellulose nanocrystal suspensions, ACS Macro Lett 12 (2023) 1733–1738.

[136] R. Prathapan, R.F. Tabor, G. Garnier, J. Hu, Recent progress in cellulose nanocrystal alignment and its applications, ACS Appl Bio Mater 3 (2020) 1828–1844.

[137] S. Butylina, S. Geng, K. Laatikainen, K. Oksman, Cellulose nanocomposite hydrogels: From formulation to material properties, Front Chem 8 (2020) 655.

[138] X. Huang, X. Ao, L. Yang, J. Ye, C. Wang, Preparation and properties of cellulose nanocrystal-based ion-conductive hydrogels, RSC Adv 13 (2023) 527–533.

[139] T. Jayaramudu, H.-U. Ko, H.C. Kim, J.W. Kim, R.M. Muthoka, J. Kim, Electroactive hydrogels made with polyvinyl alcohol/cellulose nanocrystals, Materials 11 (2018) 1615.

[140] G. Chu, D. Qu, E. Zussman, Y. Xu, Ice-assisted assembly of liquid crystalline cellulose nanocrystals for preparing anisotropic aerogels with ordered structures, Chemistry of Materials 29 (2017) 3980–3988.

[141] L. Lewis, S.G. Hatzikiriakos, W.Y. Hamad, M.J. MacLachlan, Freeze–thaw gelation of cellulose nanocrystals, ACS Macro Lett 8 (2019) 486–491.

[142] S. Busato, D. Kremer, A. Perevedentsev, Imaging-Based Metrics Drawn from Visual Perception of Haze and Clarity of Materials. I. Method, Analysis, and Distance-Dependent Transparency, Macromol Mater Eng 306 (2021) 2100045.

[143] D. Liu, X. Chen, Y. Yue, M. Chen, Q. Wu, Structure and rheology of nanocrystalline cellulose, Carbohydr Polym 84 (2011) 316–322.

[144] H. Sun, X. Liu, Y. Huang, X. Leng, Physicochemical and Sensory Properties Colored Whey Protein-Cellulose Nanocrystal Edible Films after Freeze-Thaw Treatment, Foods 11 (2022) 3782.

[145] M.-H. Chang, M. Oh-e, Kinetic arrest during the drying of cellulose nanocrystal films from aqueous suspensions analogous to the freezing of thermal motions, Sci Rep 12 (2022) 21042.

[146] R.J. Tabar, C.T. Murray, R.S. Stein, The effect of particle size on the haze of polymer films, Journal of Polymer Science: Polymer Physics Edition 21 (1983) 831–833.

[147] S. Busato, A. Perevedentsev, A simple imaging-based technique for quantifying haze and transmittance of materials, Polym Eng Sci 58 (2018) 345–352.

[148] T. Lu, H. Pan, J. Ma, Y. Li, S.W. Bokhari, X. Jiang, S. Zhu, D. Zhang, Cellulose nanocrystals/polyacrylamide composites of high sensitivity and cycling performance to gauge humidity, ACS Appl Mater Interfaces 9 (2017) 18231–18237.

[149] D. Bridgeman, J. Corral, A. Quach, X. Xian, E. Forzani, Colorimetric humidity sensor based on liquid composite materials for the monitoring of food and pharmaceuticals, Langmuir 30 (2014) 10785–10791.

[150] V.O. Neterebskaia, A.O. Goncharenko, S.M. Morozova, D.S. Kolchanov, A. V Vinogradov, Inkjet printing humidity sensing pattern based on self-organizing polystyrene spheres, Nanomaterials 10 (2020) 1538.

[151] X. Rao, L. Zhao, L. Xu, Y. Wang, K. Liu, Y. Wang, G.Y. Chen, T. Liu, Y. Wang, Review of optical humidity sensors, Sensors 21 (2021) 8049.

[152] C. Verma, M. Chhajed, S. Singh, M. Sathwane, P.K. Maji, Bioinspired structural color sensors based on self-assembled cellulose nanocrystal/citric acid to distinguish organic solvents, Colloids Surf A Physicochem Eng Asp 655 (2022) 130206.

[153] S. Taokaew, W. Kriangkrai, Recent progress in processing cellulose using ionic liquids as solvents, Polysaccharides 3 (2022) 671–691.

[154] P. Sitnikov, P. Legki, M. Torlopov, Y. Druz, V. Mikhaylov, D. Tarabukin, I. Vaseneva, M. Markarova, N. Ushakov, E. Udoratina, Efficient (Bio) emulsification/Degradation of Crude Oil Using Cellulose Nanocrystals, Polysaccharides 4 (2023) 402–420.

[155] M. Xu, W. Li, C. Ma, H. Yu, Y. Wu, Y. Wang, Z. Chen, J. Li, S. Liu, Multifunctional chiral nematic cellulose nanocrystals/glycerol structural colored nanocomposites for intelligent responsive films, photonic inks and iridescent coatings, J Mater Chem C Mater 6 (2018) 5391–5400.

[156] M. Garg, V. Apostolopoulou-Kalkavoura, M. Linares, T. Kaldéus, E. Malmström, L. Bergström, I. Zozoulenko, Moisture uptake in nanocellulose: the effects of relative humidity, temperature and degree of crystallinity, Cellulose 28 (2021) 9007–9021.

[157] J. He, K. Bian, N. Li, G. Piao, Volatile acid responsiveness of chiral nematic luminescent cellulose nanocrystal/9, 10-Bis ((Z)-2-phenyl-2-(pyridin-2-yl) vinyl) anthracene composite films, ACS Sustain Chem Eng 7 (2019) 12369–12375.

[158] T.V. de Oliveira, P.A.V. de Freitas, C.C. Pola, L.R. Terra, J.O.R. da Silva, A.T. Badaró, N.S. Junior, M.M. de Oliveira, R.R.A. Silva, N. de F.F. Soares, The influence of intermolecular interactions between maleic anhydride, cellulose nanocrystal, and nisin-Z on the structural, thermal, and antimicrobial properties of starch-PVA plasticized matrix, Polysaccharides 2 (2021) 661–676.

[159] T.M. Ejara, S. Balakrishnan, J.C. Kim, Nanocomposites of PVA/cellulose nanocrystals: Comparative and stretch drawn properties, SPE Polymers 2 (2021) 288–296.

[160] N. Park, M.A. Friest, L. Liu, Enhancing the Properties of Polyvinyl Alcohol Films by Blending with Corn Stover-Derived Cellulose Nanocrystals and Beeswax, Polymers (Basel) 15 (2023) 4321.

[161] W.C. Wong, C.C. Chan, L.H. Chen, T. Li, K.X. Lee, K.C. Leong, Polyvinyl alcohol coated photonic crystal optical fiber sensor for humidity measurement, Sens Actuators B Chem 174 (2012) 563–569.

[162] J. Li, X. Liu, H. Sun, L. Wang, J. Zhang, L. Deng, T. Ma, An optical fiber sensor coated with electrospinning polyvinyl alcohol/carbon nanotubes composite film, Sensors 20 (2020) 6996.

[163] A. Gastón, F. Pérez, J. Sevilla, Optical fiber relative-humidity sensor with polyvinyl alcohol film, Appl Opt 43 (2004) 4127–4132.

[164] Y. Wang, J. Wang, Y. Shao, C. Liao, Y. Wang, Highly sensitive surface plasmon resonance humidity sensor based on a polyvinyl-alcohol-coated polymer optical fiber, Biosensors (Basel) 11 (2021) 461.

[165] Y. Dong, H.-Y. Yu, Y. Tian, X. Yao, B. Xue, D. Xu, F. Zou, Q. Mi, Highly sensitive, self-healable, and robust polyvinyl alcohol/nanocellulose composite electronic skin by single-step Marangoni self-assembly for multipoint sensing, ACS Sustain Chem Eng 11 (2023) 13149–13163.

[166] F. Zhang, W. Ge, C. Wang, X. Zheng, D. Wang, X. Zhang, X. Wang, X. Xue, G. Qing, Highly strong and solvent-resistant cellulose nanocrystal photonic films for optical coatings, ACS Appl Mater Interfaces 13 (2021) 17118–17128.

[167] B. Wang, A. Walther, Self-assembled, iridescent, crustacean-mimetic nanocomposites with tailored periodicity and layered cuticular structure, ACS Nano 9 (2015) 10637–10646.

[168] Q. Sun, V. Lutz-Bueno, J. Zhou, Y. Yuan, P. Fischer, Polymer induced liquid crystal phase behavior of cellulose nanocrystal dispersions, Nanoscale Adv 4 (2022) 4863–4870.

[169] Y.T.H. Nguyen, T.B. Ly, B.A.T. Bui, P.K. Le, Biodegradable Polyvinyl Alcohol Composite Film Reinforced by Crystalline Nanocellulose from Rice Straw, Chem Eng Trans 106 (2023) 493–498.

[170] H.A. Silvério, W.P.F. Neto, D. Pasquini, Effect of incorporating cellulose nanocrystals from corncob on the tensile, thermal and barrier properties of poly (vinyl alcohol) nanocomposites, J Nanomater 2013 (2013) 74.

[171] C. Tsioptsias, D. Fardis, X. Ntampou, I. Tsivintzelis, C. Panayiotou, Thermal Behavior of Poly (vinyl alcohol) in the Form of Physically Crosslinked Film, Polymers (Basel) 15 (2023) 1843.

[172] X. Guo, L. Liu, Y. Hu, Y. Wu, Water vapor sorption properties of TEMPO oxidized and sulfuric acid treated cellulose nanocrystal films, Carbohydr Polym 197 (2018) 524–530.

[173] Y. Meng, Z. Long, Z. He, X. Fu, C. Dong, Chiral cellulose nanocrystal humidity-responsive iridescent films with glucan for tuned iridescence and reinforced mechanics, Biomacromolecules 22 (2021) 4479–4488.

[174] T.T.T. Hop, D.T. Mai, T.D. Cong, T.T.Y. Nhi, V.D. Loi, N.T.M. Huong, N.T. Tung, A comprehensive study on preparation of nanocellulose from bleached wood pulps by TEMPO-mediated oxidation, Results Chem 4 (2022) 100540.

[175] P. Saha, V.A. Davis, Photonic properties and applications of cellulose nanocrystal films with planar anchoring, ACS Appl Nano Mater 1 (2018) 2175–2183.

[176] A.G. Dumanli, H.M. Van Der Kooij, G. Kamita, E. Reisner, J.J. Baumberg, U. Steiner, S. Vignolini, Digital color in cellulose nanocrystal films, ACS Appl Mater Interfaces 6 (2014) 12302–12306.

[177] J.H. Park, J. Noh, C. Schütz, G. Salazar-Alvarez, G. Scalia, L. Bergström, J.P.F. Lagerwall, Macroscopic control of helix orientation in films dried from cholesteric liquid-crystalline cellulose nanocrystal suspensions, ChemPhysChem 15 (2014) 1477–1484.

[178] M. Ličen, B. Majaron, J. Noh, C. Schütz, L. Bergström, J. Lagerwall, I. Drevenšek-Olenik, Correlation between structural properties and iridescent colors of cellulose nanocrystalline films, Cellulose 23 (2016) 3601–3609.

[179] M.-H. Chang, M. Oh-e, Kinetic arrest during the drying of cellulose nanocrystal films from aqueous suspensions analogous to the freezing of thermal motions, Sci Rep 12 (2022) 21042.